ProQuest LLC.
789 East Eisenhower Parkway
P.O. Box 1346
Ann Arbor, MI 48106 - 1346

ACOUSTO-OPTIC INTERACTIONS IN SEMICONDUCTOR MULTI-LAYER OPTICAL WAVEGUIDES FOR DEVICE APPLICATIONS

By

Cameron Thompson

A thesis submitted to the Department of Electronic and Electrical Engineering, University of Surrey, for the degree of Doctor of Philosophy (Ph.D.)

Abstract

This thesis reports on work undertaken over the last three years on the modelling of the physical processes relevant to acousto-optic diffraction in multi-layered, single and multiple quantum well (QW) structures, and is mainly concerned with the AlGaAs/GaAs material system.

The propagation of surface acoustic waves (SAWs) on top of a general multi-layer structure is modelled using a basis of orthonormal polynomials to represent the appropriate solutions. The guided optical mode profiles are then determined through Maxwell's equations and matching of optical fields and field gradients at layer interfaces. The acousto-optic diffraction efficiency as a function of the wavelength of the SAW is calculated from the framework of coupled mode theory and the effects of compositional variations to the structure are considered. The effect of the SAWs on the electron/hole energy eigenvalues and envelope functions in QW structures is then considered in more detail, using a simple static approximation for the SAW. The change in complex refractive index of the QW structures is then calculated using the results of a density matrix theory expressed within the context of a semi-classical approach.

Results show that multi-layer structures have distinct advantages over single layer structures for acousto-optic applications in terms of the added control available over both the SAW induced field quantities and the guided optical mode profiles. In addition, the possibilities for constructing multiple quantum well (MQW) structures within the multi-layer structure will lead to enhanced changes in refractive index due to the presence of a SAW induced electric field. It is shown that these refractive index changes are significantly larger than those possible in bulk materials for the same acoustic powers. Also, the results indicate that the non-linearity of the SAW induced fields will, for high enough acoustic frequencies, produce different SAW induced electric fields within adjacent quantum wells of the MQW structure, an effect not suggested previously when such devices have been proposed.

Acknowledgements

I would like to thank my supervisor, Professor Bernard L. Weiss for his guidance, support and advice throughout the work that contributes to this thesis.

I am grateful to colleagues in the department of Electronic and Electrical Engineering, specifically members of the CDCR for help and advice in the use of computing facilities, and Dr A. Stoddart of the Vision, Speech and Signal Processing research group for guidance in the use of Nag libraries. I thank Dr E.H. Li of the University of Hong-Kong for useful discussions.

I acknowledge the financial support of the University of Surrey Research Committee.

Publications

The following is a list of articles published or accepted for publication, that contribute to the work under taken in the thesis :-

1. C.Thompson and B.L.Weiss "Characteristics of surface acoustic wave propagation in III-V semiconductor quantum well structures", J. Appl. Phys., **78** (8), pp.5002-5007, (1995)

2. C.Thompson and B.L.Weiss "Modal Characteristics of Graded Multilayer Optical Waveguides", J. Lightwave. Technol., **14** (5), pp.894-900, (1996)

3. C.Thompson and B.L.Weiss "Acousto-optic Bragg diffraction in SiGe/Si planar waveguides", IEE Proc-Optoelectron., **143**, pp.303-306, (1996).

4. C.Thompson and B.L.Weiss "Acousto-optic Bragg diffraction in AlGaAs/GaAs planar multilayer waveguide structures", Accepted for publication in IEEE J. Quantum Electron. (1996).

5. B.L.Weiss and C.Thompson "Acousto-optic interactions in III-V semiconductor quantum well structures for optical device applications" Conference paper to be presented at *Progress in Electromagnetics Research Symposium (PIERS),* January 9th, Hong Kong, (1997)

Acronyms

AO	Acousto-optic(s)
AOTF	Acousto-optic Tunable Filter
IDT	Inter-digital Transducer
IMP	Intermodulation Product
MBE	Molecular Beam Epitaxy
MOCVD	Metal-Organic Chemical Vapour Deposition
MQW	Multiple Quantum Well
OEIC	Optoelectronic Integrated Circuit
QCSE	Quantum Confined Stark Effect
QW	Quantum Well
SAW	Surface Acoustic Wave
TM	Transverse Magnetic
TE	Transverse Electric

Table of contents

ACOUSTO-OPTIC INTERACTIONS IN SEMICONDUCTOR MULTI-LAYER OPTICAL WAVEGUIDES FOR DEVICE APPLICATIONS

Introduction

The need for the transmission and processing of information at ever faster rates, with greater signal capacity and lower cost is both a constant goal of modern society and a driving force for scientific and technological advances. The use of light in this respect as a signal carrier, together with the huge information carrying capacity of optical fibres has lead to the optical communications revolution that we experience today.

Whilst the *transmission* of information is fully exploiting the desirable properties of light, the imprinting of that information onto the light carrier and subsequent signal processing has not yet fully caught up. The eventual goal is one of optoelectronic integrated circuits (OEICs)*, where both the optical and electronic devices relevant to the generation, detection and signal processing of the light are interconnected through optical waveguides on the same substrate wafer. A wide variety of semiconductor material systems has lead to the fabrication of a diversity of optoelectronic devices and structures, including laser diodes for emission, waveguides, and photodetectors.

The use of acoustic waves to modulate and deflect light is not new and the current generation of efficient acousto-optic devices tend to be based on the interaction of guided optical waves with surface acoustic waves (SAWs). Devices have been successfully fabricated and are available in a variety of materials and progress has been made towards monolithic integration. Acousto-optics has been, and will continue to be, used for an extensive variety of device operations. Much work is being performed at present on the development of devices such as the acousto-optic tunable filter (AOTF) for which the response of the filter can be electronically tuned through the signal applied to the SAW transducer. The presence and interaction of two types of physical wave within the active part of such devices lends itself directly to the realisation of many powerful signal processing

---

* See for example, Tamir, T. *Integrated optics*, 2nd Ed. Topics appl. Phys., Vol. 7, Springer, Berlin (1979)

techniques. The consequences of this versatility mean that acousto-optics is being used today at the forefront of new technology, such as optical computing[†] and on-board satellite applications.

Advances in semiconductor growth techniques, such as molecular beam epitaxy (MBE) and metal organic chemical vapour deposition (MOCVD), have enabled the fabrication of novel multi-layer structures over recent years for use in both waveguides and devices. Multi-layer optical waveguides provide another degree of freedom to both the nature of the optical mode profile and the possibilities for optical mode coupling, as well as being compatible with other more complicated structures fabricated within the same waveguide. Structures with layer dimensions of the order of 10-150Å, known as "quantum wells[‡]"(QWs) have enhanced electric and optical properties as a result of important quantum processes. The ability to engineer the material bandgap and band-edge properties is evident for such QW structures and offers the possibility for altering the operating wavelength of devices and also the electronic and optical characteristics for high performance optoelectronic applications. These properties can lead to improved device performance in many areas including lasers, modulators and switches. The introduction of periodicity to the QW structure allows the realisation of "superlattices" with an additional band structure leading to novel optical and electronic properties.

It is evident that the advances in material technology that have been successful in many types of semiconductor devices have not been fully considered with regard to their relevance and exploitation in the area of acousto-optic devices. It is essentially this issue that the thesis attempts to address through the computer modelling of relevant acousto-optic processes in multi-layer and multiple quantum well (MQW) structures. The main objective of the work is to ascertain whether it is likely that such structures have any inherent acousto-optic advantage over the conventionally used structures.

[†] See for example, Wherret, B.S. and Tooley, F.A.P. (Eds) *Optical computing, proceedings of the 34th Scottish Universities Summer School in Physics* (1988)

[‡] See for example, Weisbuch, C. and Vinter, B. *QUANTUM SEMICONDUCTOR STRUCTURES, Fundamentals and Applications*, Academic press Inc. (1991)

Chapter 1 gives a review of primarily the basic physics that underlies the subject of acousto-optics, starting from the two separate theories of acoustic waves in solid media, and physical optics. This leads on to a brief look at the theory of acousto-optic interactions, and its relevance to modulation and deflection of light waves. Materials are then discussed, the emphasis here being on the properties of a material that make it desirable for acousto-optic applications, together with a review of the different materials currently being used. Finally, some important device areas are mentioned together with some examples that seek to give a qualitative understanding of the importance of acousto-optic interactions in bulk, guided wave, and integrated circuit device modules. The development of the subject of acousto-optics is presented in such a way as to justify the type of materials and structures looked at throughout the thesis. In addition, a small review section on quantum well structures and devices is included at the end of chapter 1.

Chapter 2 presents a modelling study of the propagation of SAWs on multi-layered structures, with specific attention paid to AlGaAs/GaAs structures although some results are also presented for InGaAs/InP and SiGe/Si. A Laguerre polynomial method is used to solve the appropriate equations and the emphasis of the work is placed on how the material parameters of multi-layer structures affect the SAW propagation characteristics.

The determination of the guided optical modes of these type of structures is discussed in chapter 3, where Maxwell's equations are applied to a generic multi-layer structure and solutions for the electric and magnetic field profiles are determined. As in the previous chapter, the emphasis is placed on how the composition of the multi-layer waveguide affects the shape and characteristics of the guided optical mode. The results of the work presented in both chapters 2 and 3 are used in the modelling of acousto-optic diffraction, which is discussed in chapter 4. Here, an expression for the isotropic acousto-optic diffraction efficiency that has been obtained from a two-mode coupled mode theory and contains an overlap function of the acoustic and optic fields is used to determine the effect of both structure and SAW parameter variations for the multi-layer waveguides.

In chapters 2, 3 and 4, quantum confinement effects were not considered. As such, chapter 5 deals with the theoretical determination of the confined electron/hole energy levels and

envelope wave functions of single and multiple quantum well AlGaAs/GaAs structures, and the effect on these quantities of the passage of a SAW over the top of the structure. Chapter 5 also deals with the subsequent effect on the absorption coefficient and refractive index of the quantum well structures, as these two properties determine the dominant characteristics of photonic and optoelectronic devices. It is through these quantities that the question of a possible acousto-optic advantage through the use of QW structures is hoped to be answered.

Conclusions are drawn in chapter 6 and future work is also discussed.

Chapter 1

Acousto-Optics Review ; Theory, Materials, Applications and Devices

1.1 INTRODUCTION

The interaction of light with ultrasound was first predicted by Brillouin[1] (1922) and was verified experimentally by Debye and Sears[2] and also by Lucas and Biquard[3] (1932). The original theory of Brillouin was analogous to X-ray diffraction in crystals. Subsequently, work continued throughout the 1930's, and was mainly concerned with investigating possible applications of the phenomenon.

The subject was not taken up again until the early 1960's, when signal processing was investigated[4], and with the appearance of the laser, a coherent and powerful light source, interest was rekindled. When ultrasound interacts with a laser beam, it modulates and deflects it, and it was through these techniques that many more refined methods of signal processing were developed[5,6]. The laser created a need for electronically manipulating coherent light beams, and since photons have no charge this is achieved by electronically altering the properties of the material that the light is travelling in, either through the electro-optic effect[7] or the acousto-optic effect[8], the latter having certain advantages through the simple dependence of the parameters of interest (e.g. diffraction efficiency, frequency shift)

on the frequency of the acoustic wave. One of the first public descriptions of a light modulator was given by Lieben[9] in 1962 and one of the first devices used for signal processing was developed by Rosenthal[10]. Later signal processing using optical heterodyning was demonstrated by King et al[11] (1967), and the mechanism of beam deflectors was analysed by Korpel et al[12] (1965). The deflection of a beam of light by changing the frequency of sound lead naturally to the concept of an acousto-optic spectrum analyser, unlike a beam deflector where the frequencies are applied sequentially, here they are applied simultaneously. The spectrum analysis concept found applications in image display[13] (1969).

These later studies were limited mainly to bulk wave acousto-optics in which both light and sound propagate as free waves in mostly solid media, and together with material developments they led to various types of bulk wave acousto-optic devices including, modulators, scanners, deflectors, tunable filters, multiplexers/demultiplexers, spectrum analysers, correlators and other signal processors.

In addition, theoretical concepts developed at a rapid rate. Some work was done on plane wave interaction theory[14] and subsequent work included optical profiles beyond those of the plane wave[15,16]. As the theory developed, the interaction process was considered further from a quantum mechanical point of view, as a photon-phonon interaction. When the phonons are of thermal origin, this phenomenon is called Brillouin scattering[17].

With work now firmly established in finding practical applications of acousto-optics, the need for more sensitive acousto-optic materials came about, and this was reflected in the parameters used to describe materials as they shifted from the context of crystallography to device operation. Smith and Korpel proposed a figure of merit for diffraction efficiency[18], now called M_2. An attempt was made at predicting elasto-optic coefficients from first principles[19], and values of constants and figures of merit can now be found in many places[20].

Since the early 1970's much work has been done on 'Guided wave acousto-optics'[21] in which both the light and sound are confined to a relatively small depth in suitable structures. This interest in guided wave acousto-optics was a natural progression from the technologies

of both guided wave optics and surface acoustic wave (SAW) devices, and led to immediate applications in optically integrated circuits [22,23].

Acousto-optics is a means of investigating the physical properties of a material[24] as well as being an advanced technique in applied optics. Methods of interaction of light with acoustic waves lead to the determination of velocities and acoustic attenuation as well as photo-elastic constants.

The theory of acousto-optics is most readily accessible through the well established theories of elasticity and optics. The mechanical response of a material to an applied stress, together with the laws of motion are the two ingredients needed to produce an acoustic wave, and in optics the physical equations of Maxwell give rise to electro-magnetic waves.

The interaction of acoustic and electro-magnetic waves lies at the heart of acousto-optics and can be schematically visualised as the passage of an acoustic wave through a medium, causing periodic variations of stress, which through the elasto-optic effect (and possibly also the electro-optic effect), cause modifications of the refractive index, which influence the propagation of light waves.

The selection of acousto-optic materials could at first seem a free and easy choice since all material states, whatever the symmetry of the crystal, experience the elasto-optic effect. Since the theory of the elasto-optic effect is a macroscopic one, then guidance for selection of materials must come from empirical and semi-qualitative rules, which will be discussed in more detail later. Suffice to say, the main materials used during the last twenty years have formed a relatively small group consisting of Lithium Niobate ($LiNbO_3$), Tellurium dioxide (TeO_2), Gallium Phosphide (GaP), with increasing interest in semiconductors such as Gallium Arsenide (GaAs) and Indium Phosphide (InP).

The use of surface and bulk acoustic waves in bulk materials is well established for the fabrication of various acousto-optic modulators and deflectors[25]. However with the advent of new low dimensional structures, such as 'quantum wells'[26] that show enhanced electro-optic behaviour, the possibilities for constructing more efficient devices have increased.

1.2 THEORY

1.2.1 Bulk and surface acoustic waves

It is important to outline the conceptual framework within which the physics is expressed. Acoustic waves travelling in crystalline solids can be most generally visualised as corresponding to the large wavelength limit of modes of lattice vibration[27], where the acoustic wavelength is much larger than the atomic separation. In this sense, a macroscopic description of the behaviour of the solid under passage of an acoustic wave is justified, where the solid is assumed to be a homogeneous continuum, and the equations of motion are expressed in terms of the displacement of "particles" (see Figure 1.1) that are assumed to be much bigger than atomic dimensions but much smaller then the wavelength of the acoustic waves of interest.

1.2.1.1 Non-piezoelectric media

Any acoustic wave is brought about by the mechanical response of the propagation medium to an applied stress, and the temporal development of the wave is subject to the laws of motion. The resulting strains in the crystal structures studied here are relatively small (i.e. we assume that the materials behaviour can be treated as elastic), the corresponding 'mechanical response' is then a generalised Hooke's law[28]

$$T_{ij} = c_{ijkl} S_{kl} \qquad \text{-(1.1)}$$

where subscripts range from 1 to 3. 'Generalised', here means tensors are used to describe the anisotropic structure, i.e. T is the stress tensor, S the strain tensor and c the stiffness tensor. A full explanation of the nature of these tensors is found in the text of Nye[29]. The relevant 'equation of motion' is Newton's second law ;

$$\frac{\partial T_{ij}}{\partial x_j} = \rho \frac{\partial^2 u_i}{\partial t^2} \qquad \text{-(1.2)}$$

Where u_i is the particle displacement. Equations (1.1) and (1.2) contain the essential physics of acoustic waves in elastic media. Combining the two equations together we obtain ;

$$\rho \ddot{u}_i = c_{ijkl} u_{k,lj} \qquad \text{-(1.3)}$$

which is a familiar second order differential equation whose solutions represent waves. Each u_i must satisfy this wave equation. Consider an infinite propagation medium, and no boundary conditions, if a solution of a general plane wave form is assumed and is substituted into the wave equation we find that for all non-zero u_k the following must be true;

$$\left|(c_{ijkl} s_j s_l - \rho v^2 \delta_{ik})\right| = 0 \qquad \text{-(1.4)}$$

Thus for any propagation direction s, Equation (1.4) will give the corresponding wave velocity, which will be independent of the frequency of the wave.

Consider now a semi-infinite medium bounded on one side by air, and now add the requirement that the amplitude of the wave decreases with depth. One such solution of the wave equation is known as a Rayleigh wave[30] and takes the general form;

$$u_i = U_i \exp(-(\alpha + j\beta))x_3 \exp j\omega\left[t - \frac{s_1 x_1 + s_2 x_2}{v_s}\right] \qquad \text{-(1.5)}$$

where α will be a complex number whose real part we require to be positive and v_s is the velocity of the Rayleigh wave. The solution of the wave equation is identical in form to the case for the volume waves, except that s_3 will now no longer represent the direction component parallel to the x_3 axis. An equation involving the determinant of a matrix (i.e. of the form of Equation (1.4)) is again obtained involving now the surface velocity. The problem is reduced to finding the surface velocity, the decay constant with respect to depth (α) and the corresponding particle displacements. The determinantal equation represents a sixth degree polynomial equation in α , which can be solved analytically for very simple

situations such as when the propagation medium is isotropic[31]. For anisotropic materials the surface velocity is usually found using iterative techniques for computers, which then allows determination of decay constants, which can be found using simple numerical techniques.

1.2.1.2 Piezoelectric media

In an analogous way to the generalised Hooke's law, the electric displacement D in a non-piezoelectric material is related to the electric field E through the physical property of permittivity, represented by the two index permittivity tensor;

$$D_i = \varepsilon_{ik} E_k \qquad \text{-(1.6)}$$

In piezoelectric media there is a coupling between electric fields and stresses and hence between strains and polarisations, as a result the stress becomes a function of both strain and electric field, as does the electric displacement. The equations of piezoelectricity are written;

$$T_{ij} = c^{E}_{ijkl} S_{lk} - e_{kij} E_k \qquad \text{-(1.7)}$$

$$D_i = e_{ikl} S_{kl} + \varepsilon^{S}_{ik} E_k \qquad \text{-(1.8)}$$

where c^E is the stiffness tensor in a zero electric field and ε^s the permittivity tensor for zero strain. The modification of the stress tensor leads to a new wave equation involving the particle displacement coupled to an electric potential, together with a second wave equation which uses Maxwell's equations since any electromagnetic phenomena must also obey these.

An absence of free charges is assumed together with the assumption that time derivatives of magnetic fields are effectively zero, this is known as the quasi-static approach and leads to a longitudinal electric field associated with a plane acoustic wave. A full discussion of the foundations of the theory is given in various papers [32,33].

1.2.2 Physical optics

Since we have been dealing with a physical description of acoustic waves in terms of tensors and differential equations, it is only sensible to treat optics in the same way, and hence we must use Maxwell's equations to describe the electromagnetic waves[34].

As far as general signal processing is concerned, a full treatment is given in many texts. The important concepts for acousto-optic applications are mentioned here briefly.

Optical waveguides are important to almost every application of modern optics, and when applying Maxwell's equations to waveguide structures, a wave equation is needed, which can be obtained by assuming no current sources and taking the curl of the relevant Maxwell equation. After applying any relevant boundary conditions with reference to the structure of the waveguide, the solutions of the wave equations give the spatial distributions of the optical waves in one or more dimensions, and are known as modes. Any optical beam used in a practical acousto-optic interaction will consist of these modes. Other properties of the solutions of the wave equation that will be of interest in acousto-optic interaction will be the polarisation and the propagation vector of the optical beam.

Once the precise parameters of the optical beam are known and the interaction is to be looked at, the relevant optical and acousto-optical properties of the propagation medium need to be assessed. 'Propagation medium' here means the medium that the *acoustic* wave is propagating in, and of interest is what effect it will have on any incident light beam.

1.2.3 Electro-optic and elasto-optic effects

1.2.3.1 The index ellipsoid

On application of an electric field to an isotropic material, the induced electric displacement D is parallel to the electric field E and related to it via the absolute permittivity, ε;

$$\underline{D} = \varepsilon \underline{E} \qquad \text{-(1.9)}$$

at optical frequencies, the refractive index is given by the square root of the relative permittivity and the velocity of propagation is then the velocity of propagation in vacuum divided by the refractive index. However, in anisotropic media, Equation (1.9) becomes direction dependent and as a result the permittivity becomes a second rank tensor ;

$$D_i = \varepsilon_0 \varepsilon^r_{ij} E_j \qquad \text{-(1.10)}$$

A so called 'representation quadric' or 'indicatrix' (which is simply a geometrical construction) can be associated with the permittivity tensor thus ;

$$(\varepsilon^r)^{-1}_{ij} x_i x_j = 1 \qquad \text{-(1.11)}$$

This is the equation of an ellipsoid and if we identify the relative permittivity with the inverse of the square of a refractive index; the optical indicatrix is then a surface given by;

$$(1/n^2)_{ij} x_i x_j = 1 \qquad \text{-(1.12)}$$

This surface is a *geometrical representation* used for describing the behaviour of electromagnetic waves in anisotropic media, and gives us access to the variation of refractive index via the shape of the representation, e.g. for cubic crystals the indicatrix is a sphere.

1.2.3.2 The elasto-optic effect

The elasto-optic effect is the change in the refractive index of a medium, as a result of a strain (with components S_{kl}) associated with an applied stress (with components T_{ij}). Since the optical indicatrix represents the spatial variation of refractive index, then any change in refractive index will obviously have some effect on the indicatrix. Consequently we re-write the ellipsoid equation as ;

$$\left(\left(\frac{1}{n^2}\right)_{ij} + \Delta\left(\frac{1}{n^2}\right)_{ij}\right) x_i x_j = 1 \qquad \text{-(1.13)}$$

Initially it was supposed that the variations in the indicatrix were related to the S_{kl} components by some tensor of rank 4 with components p_{ijkl} ;

$$\Delta\left(\frac{1}{n^2}\right)_{ij} = p_{ijkl} s_{kl} \qquad \text{-(1.14)}$$

i.e. the relationship between the observed change in refractive index and the observed strain was assumed to be linear, as we shall see, this is not strictly valid.

Because of the symmetry of the index ellipsoid components and the symmetry of the strain tensor, Equation (1.14) can be re-written in reduced index form using p_{mn}, where the p_{mn} related to the standard crystallographic axes are known as the 'photo-elastic constants'.

If a crystal is subjected to a strain, the strain will have symmetry properties which will be reflected in the corresponding tensor. The index ellipsoid will undergo modifications, but will conserve the symmetry elements common to the strain and the crystal before deformation. In short, this allows the reduction of the number of independent photo-elastic constants for each crystal system, just as in the case for the stiffness tensor.

Thus the form of the p_{mn} matrix for every crystal group can be deduced from Equation (1.14) by the application of symmetry operations.

Nelson and Lax[35] established that Equation (1.14) contradicts certain experimental evidence, and they suggested that for defining p_{ijkl}, S_{kl} is not the best independent variable to consider. They proposed using the gradient of the particle displacement $u_{k,l}$, instead ,which possesses nine components and includes the anti-symmetrical parts (e.g. rigid body rotations) which were not included in the definition of the strain tensor. The corresponding changes in the refractive index now include anti-symmetrical effects, and the inclusion of these effects for

certain materials has been verified experimentally (these effects are only present for double refracting crystals).

1.2.3.3 The electro-optic effect

The electro-optic effect is the change in refractive index in a medium due to the presence of an electric field. In the most general case this effect contains both the linear (Pockel's effect) and the non-linear (Kerr effect) components. The constitutive equations of the linear effect are given in the form ;

$$\Delta\left(\frac{1}{n^2}\right)_{ij} = r_{ijn}E_n \qquad \text{-(1.15)}$$

Interestingly, there is a similar equation to (1.15) for variations in stress due to the piezoelectric effect, and just like the piezoelectric effect, the electro-optic effect does not occur in crystals that are centrosymmetric (this is because r_{ijn} is a three index tensor and thus can never possess centrosymmetric properties). Following reduction of the number of indices to two, through symmetry considerations, we obtain r_{mn}. The r_{mn} are known as the electro-optic constants, and can be deduced for each point group by observing that the r_{mn} matrix will have the same form as a transposed reduced index piezoelectric matrix (e_{il}).

Obviously piezoelectric materials will complicate things further since an applied electric field will produce a strain which will contribute to a change in the refractive index. It is important to be clear here of just what the piezoelectric effect consists of; in piezoelectric media for certain directions there is a *coupling* of a *wave of deformation* and a *longitudinal electric field.* In this case the variation in the indicatrix can be expressed by adding contributions from the strain and electric fields and re-expressing the electric field contribution in terms of strains and piezoelectric constants, a modified photo-elastic constant is then obtained that characterises the overall effect[36] .

1.2.4 Diffraction of light by an acoustic wave

Here, a simple approach to the interaction of two plane waves, one electromagnetic the other acoustic will be considered in order to provide a generic quantitative framework within which the operation of different device types can be compared. The propagation medium is transparent with respect to photons. Consider that a periodic variation of refractive index has been set up in the medium by means of a bulk/surface acoustic wave travelling in the x direction, see Figure 1.2, and is given by

$$n(x,t) = n_0 - \delta n_0 \sin(\Omega t - Kx + \delta) \qquad \text{-(1.16)}$$

where Ω is the angular frequency of the SAW, K is the momentum vector of the SAW and n_0 is the refractive index without any perturbing effects. In practice δn_0 could be made up from many contributions such as the photo-elastic and electro-optic effects. The electric field of the optical wave must satisfy the appropriate wave equation obtained from Maxwell's equations, which is given by:

$$\nabla^2 E = \frac{[n(x,t)]^2}{c^2}\frac{\partial^2 E}{\partial t^2} \qquad \text{-(1.17)}$$

where E is the electric field, $n(x,t)$ is the refractive index distribution and c the velocity of light in vacuum. Since the incident optical mode is assumed of the plane wave form we can justifiably represent the electric field for this structure as a Fourier series of plane waves;

$$E = E_0 \sum_{q=-\infty}^{q=+\infty} a_q(z)\exp[j(\omega_q - k_l(z\cos\theta + x\sin\theta) - qk_s x)] \qquad \text{-(1.18)}$$

where k_l is the incident wave vector of the electric field and hence it is assumed to be oriented in the x, z plane at an angle θ to the wavefronts of the acoustic wave. Substituting (1.18) into (1.17) and neglecting second derivatives of the expansion coefficients a_q, the following set of coupled first order differential equations is obtained;

$$\frac{da_q}{dz} - \frac{\pi\delta n_0}{\lambda_0}(a_{q-1} - a_{q+1}) = \frac{jqQ}{2L}(q - 2\alpha)a_q \qquad \text{-(1.19)}$$

where, $Q = \frac{2\pi L}{\lambda_s^{\,2}}\frac{\lambda_0}{n_0}$ and $\alpha = \frac{-n_0\lambda_s \sin\theta}{\lambda_0}$

For q ≠0 there are diffracted modes. Energy transfer between modes depends on the coupling coefficient $\pi\delta n_0/\lambda_0$, and phase matching. For q = ±1, the right hand side of Equation (1.19) must be small, to transfer energy out of the zeroth order. There are two ways of doing this

i) By working at α=0 and Q << 1.

ii) By working at angles of incidence given by α = ±1/2 with Q >> 1

and they correspond to two different regions of acousto-optic diffraction. **i)** corresponds to the Raman-Nath[37] region for which many diffraction orders can be observed simultaneously, **ii)** corresponds to the Bragg region and under these conditions there is only a single diffracted beam.

The most common approach for detailed treatment of acousto-optic interactions is the so called coupled mode technique[38], which can be used to derive the difference between the Bragg and Raman-Nath processes.

There are different types of diffraction which can be categorised by the effect on the momentum vector of the guided mode; in isotropic diffraction the polarisation of the guided mode is unchanged, whereas in anisotropic diffraction, a change in polarisation can occur and/or the propagation medium is optically anisotropic.

1.3 MATERIALS

The suitability of a material for acousto-optic applications is assessed through the use of the "acousto-optic figures of merit", which are expressed in terms of well known material

parameters, such as the refractive index, density, velocity of sound and photo-elastic components. The figure first proposed[18] (by Smith and Korpel in 1965) and most commonly used is known as "M_2" and has the form,

$$M_2 = \frac{n^6 p^2}{\rho V^3} \qquad -(1.20)$$

where n is the refractive index, ρ is the density, V is the velocity of sound and p represents the appropriate photo-elastic component. The other figures of merit are closely related to M_2 in form (see Chang[25] 1976) and are applicable to different types of device design, for example M_1 (proposed by Gordon[39], 1966) considers bandwidth as well as diffraction efficiency. All figures of merit are maximised in materials having high refractive indices, high photo-elastic components, low densities and low sound velocities. The acoustic loss from a material is also important and is characterised by the attenuation of a propagating ultrasonic beam.

		ACOUSTIC			OPTIC		FIGURES OF MERIT*			
Material	Density (gm^{-3})	Mode & prop. direction †	V (ms^{-1})	Att., α	ref. index, n	λ_o (μm)	M_1	M_2	M_3	M_4
Fused Silica	2.2	L	5.96	7.2	1.46	0.633	1	1	1	1
$LiNbO_3$	4.64	L[100]	6.57	0.1	2.20	0.633	8.5	4.6	7.7	15.5
Diamond	3.52	L[100]	17.50	2.6	2.42	0.589	9.6	0.68	3.3	138
TeO_2	6.0	L[001]	4.20	6.3	2.26	0.633	17.6	22.9	25	13.5
GaP	4.13	L[110]	6.32	3.8	3.31	0.633	75.3	29.5	71	192
As_2Se_3	4.64	L	2.25	27.5	2.89	0.633	204	722	539	57.4
GaAs	5.34	L[110]	5.15	15.5	3.37	1.150	118	69	137	202
Ge	5.33	L[111]	5.50	16.5	4.00	10.60	1260	540	1365	2940

Table 1.1 Data taken from Chang[25] (1976)

* All figures are normalised with respect to fused Silica :- $M_1=7.83\times10^{-7}$ [cm^2sg^{-1}], $M_2=1.51\times10^{-18}$ [s^3g^{-1}], $M_3=1.3\times10^{-12}$ [$cmsg^{-1}$], $M_4=4.06\times10^5$ [$cm^4s^{-1}g^{-1}$].

† e.g. L[100] means the longitudinal mode in the [100] direction

‡ α is the acoustic attenuation per unit time at f=1GHz, and has units of dB/μsec

Guidelines for selection of acousto-optic materials, based on these figures of merit were set out by Pinnow[19] in 1970, and lead to the use of new materials. Table 1.1 (previous page) shows the important acousto-optic factors and corresponding figures of merit for a selection of commonly used materials.

1.4 APPLICATIONS AND DEVICES

A brief look at the important acousto-optic device concepts will be given here, with specific reference to the individual device areas that contribute to the development of acousto-optics.

1.4.1 General principles

All acousto-optic devices are based on light deflection or modulation occurring in a transparent medium in which ultrasound is propagating. The acoustic waves can be progressive or stationary, surface or bulk waves.

In general there are three types of acousto-optic device ; deflectors, modulators and tunable filters, each utilising some form of AO diffraction. Bragg diffraction is more efficient than Raman-Nath diffraction and tends to be used more in devices. The Bragg cell then can be considered as a fundamental building block of acousto-optic devices and device modules. There are essentially three useful characteristics of Bragg cells,

1. The frequency of light is shifted either up or down by the frequency of the SAW, depending on the components of the momentum vector of the optical wave. This can be used to perform frequency shifting and frequency modulation of guided optical waves.

2. The angle of deflection of the diffracted light increases linearly with the acoustic frequency so by tuning the RF frequency applied to the SAW transducer the cell can be used to perform high speed light beam deflection/scanning and multi-port light beam switching.

3. The intensity of the diffracted light is proportional to the power of the RF signal, provided the cell is not driven into saturation. This provides obvious applications to implementations of intensity modulators.

Deflectors are used principally in optical scanning and information processing applications. The direction of the diffracted beam can be varied by changing the driving frequency of the acoustic wave. A careful balance is required between bandwidth, diffraction efficiency and time aperture. The first two speak for themselves, time aperture is the time taken for the optical wave to cross the acoustic wave, and is a fundamental measure of the frequency resolution and speed of the device.

A device is considered to be a modulator if it's primary function is to impress information on a light wave by temporally varying one of it's properties, such as phase or intensity. A deflector or switch on the other hand changes the spatial position of the light or turns it on or off.

The concept of deflection raises the question, can a deflector be used as the dispersive element in an optical spectrometer? The acousto-optic tunable filter (AOTF) permits fast, electronically controlled tuning over a wide wavelength range and is useful therefore for spectral analysis and optical computing. This type of device was first proposed in 1969[40], and much work is being done at present on improving the performance of these devices[41] and on new applications such as femtosecond optical pulse shaping[42].

1.4.2 Bulk devices

Bulk acousto-optic device technology (where the acoustic wave propagates freely throughout the bulk of the propagation medium as opposed to the surface) is well established, amongst the most well-developed applications of these devices is the spectrum-analyser. The acousto-optic part of the device is a simple Bragg cell, and each incident light beam is deflected at an angle proportional to it's frequency, so the beams may be separated easily. The principles of bulk devices tend to carry over into the region of guided wave

devices and integrated devices and for this reason will not be covered here to avoid duplication.

1.4.3 Surface acoustic wave (SAW) technology

Bulk elastic waves propagating inside solids have played important roles in electronics for many years, initially for use in oscillators and filters[43], and later for incorporation in devices employing delay lines[44]. More recently though attention has turned to surface acoustic waves and the possibilities available in constructing signal processing devices which use these types of waves.

Surface acoustic wave devices are becoming increasingly more popular for signal processing applications and operate most readily with bandwidths in the range 10 to over 1000 MHz. The devices are small in size, easily fabricated (exploiting the already established technique of photolithography) and the energy of the relevant physical processes is readily accessible at the surface for tapping, guiding, reflecting, focusing, absorbing etc., leading to a large design flexibility and multitude of applications.

1.4.3.1 Generation and detection

To make SAWs useful for signal processing, the ability to generate and detect them is essential. This is achieved by the use of an interdigital transducer (IDT). An IDT is simply an array of metal strips placed on the piezoelectric substrate on which the SAW is to be generated (see Figure 1.3). When an RF voltage is applied across the IDT, the inverse piezoelectric effect causes surface waves of that frequency to be generated. There is an optimum separation of the transducer fingers that leads to constructive interference of the SAWs generated at each finger for a particular wavelength. The greater the number of finger pairs, the greater is the efficiency as more pairs are adding constructively, however there is a bandwidth reduction as one uses more and more pairs. Within a first order approximation, the frequency response of the SAW transducer is the Fourier transform of the finger overlap pattern[45]. Thus by taking the inverse transform, any required frequency

response can be realised by an appropriate IDT. SAW devices in this form are used widely in making bandpass filters[46,47], resonators, and oscillators.

1.4.3.2 Devices

Many SAW devices implement the concept of a delay line for their operation. A filter employing a delay line would produce signals along it's length which would be tapped off to provide the output. Recursive filters insert the delay line in a feedback loop, the response to an impulse input would be a sampled exponential decay with time constant $-\alpha$ and time between samples T. Non-recursive filters have no feedback loop, the output is formed by summing samples of the input, each with a different weight, taken at various points along the delay line. Such a filter is known as a transversal filter, it's effectiveness was limited because of the large velocities involved, giving rise to relatively small delays over practical distances. This difficulty is overcome by the use of acoustic delay lines. Surface acoustic waves have a velocity of the order of 3×10^3 ms^{-1} in the materials commonly used which produces significant delays of signals within convenient, accessible distances, the electrical signal is converted to an acoustic wave, usually by using an IDT which is fabricated on the surface of a piezoelectric solid. These electrodes are used to tap and produce the energy along the surface and the summation is automatically provided by the structure.

If the processing of signals of different frequencies is required, it is immediately apparent that, since the delay lines are designed in the time domain and outputs are desired in the frequency domain, then the Fourier transform would provide a useful tool in assessing the design of these types of devices.

Spectrum analysis, as mentioned in the previous section, is an area that takes full advantage of the SAW signal processing capabilities. If the spacing between the IDT fingers is designed to vary linearly along the propagation axis, it is possible to obtain delays which vary linearly with frequency, this is the principle of the linear frequency modulator (LFM), commonly referred to as a "chirp" filter. Slanted chirp transducers (SCT)[48] focus SAWs to a point, and the point to which the SAWs are focused moves with frequency, leading to determination of the relative amplitude of the frequency components of a signal.

RF demultiplexers can be also realised using the Bragg cell spectrum analyser. Each frequency within the incoming bandwidth is deflected into an appropriate detector.

Digital as well as spread spectrum transmission systems need matched receivers to "decide" between useful signals and interference and to make other such judgements of comparison on transmitted signals. The processes of convolution, correlation and decoding, which are used for these purposes can be efficiently realised using SAW devices. One such implementation of convolution exploits the interaction of a SAW with the free carriers on the surface of a semiconductor, a so called "space-charge coupled" SAW device[49,50], which utilise the piezoelectrically induced electric fields on appropriate semiconductors, allowing the transport of charge across the structure.

1.4.4 Guided wave devices

The use of waveguides in optoelectronic devices provides a means for interconnection of devices and is therefore important to the construction of optoelectronic integrated circuits. Since indirectly, many acousto-optic devices involve an electro-optic effect, the fundamental operation of electro-optic devices provides a foundation for more complicated acousto-optic devices and it is therefore of interest to briefly mention purely electro-optic devices.

1.4.4.1 Electro-optic devices

As far as single waveguide structures are concerned there are several different types of modulators and deflectors that can be fabricated in planar or channel waveguides, and many of these devices can function either as a modulator or a deflector.

A basic single waveguide structure is a Shottky barrier diode with a substrate forming an optical waveguide. Considering its operation as a phase modulator, when a reverse bias is applied to the Schottky barrier diode the waveguide becomes part of the depletion region, and the electric field then present in the waveguide causes a change in the phase of light waves travelling along the guide and hence provides the mechanism for phase modulation[51]. This type of structure can also be used in such a way as to cause rotation of the optical

polarisation vector as a result of propagation through the waveguide. This polarisation change is then detected and provides the mechanism for modulation.

The Schottky barrier/Waveguide structure is most often used for intensity modulation, where the difference in refractive index between the substrate and the waveguide is carefully engineered to tailor the waveguide to be at the threshold for guiding the lowest order propagation mode with no electric field present. On application of an electric field the change in refractive index causes the waveguide to become transmissive. A modulator of this construction was first implemented by Hall *et al.*[52] in GaAs and similar devices have been constructed in $LiNbO_3$.

The electro-absorption modulator, is based on the Franz-Keldysh effect[53], which is the shifting of a semiconductor absorption edge to longer wavelength on application of a large electric field (~ 10^5 Vcm^{-1}). Intuitively very effective electro-absorption modulators can be constructed for light of slightly less than bandgap wavelength since application of an electric field of the correct order of magnitude will cause relatively large changes in the absorption around the band-edge.

Dual channel electro-optic modulators are also used in guided wave technology. In this case the common mechanism of operation is to apply modulating signal voltages to the electrodes of each channel, resulting in slight differences in the refractive indices of each guide, and hence in the propagation constants of the respective modes. The transfer of power through the dual-channel guide will then be a function of this difference in propagation constants. Another class of dual channel modulator is based on a waveguide version of the Mach-Zehnder interferometer in which coherent light waves that have travelled different path lengths are made to interfere[54]. These types of single and double channel waveguide modulators were among the first types to be developed into integrated optical devices.

Electro-optic modulators based on diffraction are generally based on the Bragg effect rather than the Raman-Nath effect, and were first proposed by Hammer[55] and later, other authors including Lee and Wang[56] presented theoretical and experimental studies . Very efficient

Bragg diffraction electro-optic modulators can be made if grating geometry and tolerances are carefully controlled.

When discussing waveguide modulators as opposed to bulk electro-optic modulators it is important to compare the different power requirements, and since the modulating power required is proportional to the active volume' it is obvious that significantly less power is required by a waveguide device.

1.4.4.2 Acousto-optic devices

As would be expected in acousto-optic modulation, two fundamentally different types of modulation are possible ; Raman-Nath and Bragg type. In Raman-Nath modulators the optical beam is incident transversely to the acoustic beam and the width of the acoustic beam is relatively short. For Raman-Nath type diffraction to take place, the interaction length must be short enough to prevent multiple diffraction occurring. Light passing through the device undergoes a phase shift $\Delta\varphi$, given by

$$\Delta\varphi = (\Delta n 2\pi l/\lambda_0)sin(2\pi y/\Lambda) \qquad -(1.21)$$

where Δn is the acoustically induced index change, l is the interaction length (i.e. the distance over which interaction occurs), and Λ is the acoustic wavelength. The change in refractive index can be expressed in terms of one of the acousto-optic figures of merit, and the intensity of the diffracted orders are found to be Bessel functions of the phase changes.

These types of modulators generally have a smaller modulation index than that of comparable Bragg modulators, and they cannot easily be used as optical switches because the diffracted light is spatially distributed over many orders. Bragg modulators on the other hand are widely used as intensity modulators, beam deflectors and optical switches.

In Bragg type modulators the acousto-optic interaction length is relatively long, giving rise to multiple diffraction. It is important to note that the transition between the Bragg and Raman-Nath regions is not discrete and indeed there is in fact a range of interaction lengths

for which a composite type of diffraction occurs. When designing devices it is important then to tailor the interaction length so as to produce a device that is clearly Bragg or Raman-Nath.

In guided wave devices, such as those used for optically integrated circuit applications, the power requirements are much less than their bulk counterparts since the optical and acoustic waves can be confined to the same small volume. The first waveguide acousto-optic modulators were hybrid devices[57], with the guided light in a different material to that which the acoustic wave is launched in, later monolithic devices were also constructed[58,59] in materials such as GaAs and $LiNbO_3$, producing very high modulation indices in many cases.

Although the Bragg and Raman -Nath type diffraction processes are by far the most common techniques employed in constructing acousto-optic modulators, there are other methods available. These methods generally make use of acoustic waves to induce coupling between various modes in the waveguide[60,61,62].

Bragg modulators are equally capable of functioning as deflectors and optical switches. If the frequency of the acoustic beam is held constant, the optical beam can be switched through the angle $2\theta_B$ by supplying sufficient acoustic power to provide 100% diffraction from the zeroth order beam to the first order beam. If the acoustic frequency is varied the optical beam can be switched through different angles. However as the frequency (wavelength) of the acoustic beam is varied the diffraction condition is no longer exactly satisfied and other orders appear, together with a corresponding reduction in intensity of the first order peak. This reduction in intensity will obviously limit the bandwidth of any operating device.

The geometry of the interdigital transducer used to excite the acoustic waves is an important factor when considering the efficiency of any proposed acousto-optic device. If a large bandwidth is required, then decreasing the interaction length will achieve this, however this will be at the expense of diffraction efficiency since the phase shift (Equation (1.21)) and hence the modulation index contain the interaction length as a factor. More sophisticated structures are required for both wide bandwidth and high diffraction efficiency, e.g. the *chirp*

transducer in which the interdigital spacing is gradually changed along it's length[63], thus allowing for the optimal generation of different acoustic frequencies along the length of the transducer, and increasing overall bandwidth. Using a multiple array of transducers, each tilted with respect to the other, and each having a different interdigital spacing, will also increase bandwidth and diffraction efficiency and this type of set-up is very effective since it permits the Bragg condition to be satisfied over a large acoustic aperture and a large frequency range.

The frequency shift effect is usually ignored when considering the modulation and deflection processes, although it can be useful in certain applications. Consider two acoustic waves of the same frequency, launched on a waveguide substrate in opposite directions. After interaction the optical beam will have components of frequency that have been shifted by small equal amounts, above and below the original frequency of the incident wave. The two components of the optical beam beat together to produce a beam with a modulated sub-carrier frequency equal to twice the equal shifts in frequency. This is the basis of the standing wave surface acoustic wave optical modulator (SWSAWOM)[64], which has applications in frequency division multiplexing of optical beams.[65]

1.4.5 Integrated acousto-optic devices

Continuing progress in the design, fabrication and performance of components such as optical waveguides, waveguide lenses, laser sources and photo-detector arrays and their integration have advanced the possibilities for a variety of integrated acousto-optic device modules and circuits. $LiNbO_3$ and GaAs remain the two most promising substrate materials. Channel planar composite waveguides[66] have become increasingly important, allowing a large number of light sources to be used and hence utilising the channel capacities inherent in arrays of diode lasers, optical fibres and photodetectors. These can be fabricated in $LiNbO_3$ using a Titanium indiffusion (TI) process[67] and in GaAs using epitaxial methods and etching techniques to form the channel waveguide array. Planar waveguide lenses are among the key components in integrated optic circuits, and various fabrication techniques and lens types have been developed. There are two relatively new fabrication techniques that are capable of

producing microlens arrays and large aperture lenses. One is Titanium-Indiffusion Proton-Exchange (TIPE)[68,69] which is applicable to $LiNbO_3$, the TI process is first used to form the waveguide, chemical etching is used to define the lens area and then a proton exchange technique[70] is used to form the lens. Recently the ion-milling technique has been successful in producing lenses in GaAs[71].

The work done so far indicates that acousto-optic integrated device modules will have small substrate dimensions along the optical path and will be inherently of high modularity and versatility. Two such devices are mentioned here.

The integrated acousto-optic device that tends to receive most attention is the integrated optic RF spectrum analyser, which is used for real time processing of wide band RF signals. Just as in the bulk case, the spectral analysis process is based on the fact that the deflection angle and the intensity of the Bragg diffracted light are proportional to the frequency, and the power of the RF signal being applied to the surface acoustic wave transducer respectively. A hybrid approach to the fabrication is the most common at the moment, consisting of usually a $LiNbO_3$ substrate for the Bragg cell. The beams emerging from the acousto-optic part of the device are focused by a lens onto a photo-detector array, and the relative intensity of each beam is then accessible and is proportional to the strength of the corresponding RF frequency component. Figure 1.4 shows a schematic diagram of an integrated acousto-optic spectrum analyser[72].

To facilitate a total or monolithic integration, GaAs would be the ideal substrate because then both the laser and the photodetector array, together with the associated electronic devices could be fabricated in the resulting waveguide[73,74], as the technology of light sources and detectors is already well established on this substrate [75,76]. Significant progress has been made in the realisation of wide band acousto-optic Bragg cells on this substrate material[77]. Other materials that are capable of integrating the Bragg cell and the photo-detector array on the same substrate are thermally oxidised silicon (SiO_2/Si)[78], and arsenic trisulphide on thermally oxidised silicon (As_2S_3/SiO_2/Si)[79] where a ZnO film was deposited on a portion of the substrate of this module, to provide a piezoelectric film for efficient surface acoustic

wave generation. The As_2S_3 was used to provide efficient acousto-optic Bragg diffraction, due to it's high acousto-optic figure of merit.

The ability to perform real time correlation of two signals is one of the key requirements in radar and communication systems. Correlators can be basically classified into two types ; time integrating[80] and spatial integrating[81]. Spatial integrating correlators perform correlation by integrating the light diffracted by all parts of the signal(s) which are simultaneously present in the light beam aperture of the Bragg cell. The input signal is correlated with a time delayed reference signal and the two are spatially integrated to produce the correlated output. Time integrating correlators perform correlation by using a closely spaced photodetector array to integrate in time for each point within the Bragg cell.

Hybrid and monolithic structures for integrated optic implementations of time integrating correlators have been suggested. Multi-channel RF correlator modules using acousto-optic and electro-optic Bragg diffraction have been fabricated and tested.

In summary, successful monolithic integration of AO devices really hinges on the development of *efficient wide-band AO Bragg cells in GaAs*. High diffraction efficiencies and large bandwidths have been achieved[82]. Clearly as far as monolithic integration of optic device modules based on GaAs substrates is concerned, a key component is an efficient, wideband acousto-optic Bragg cell. Theoretical studies have shown that[77] bandwidths as large as 1.6 and 1.4 GHz are possible for specific cuts of the GaAs-AlGaAs waveguide.

1.5 QUANTUM WELLS; PROPERTIES AND DEVICES

1.5.1 Introduction

When the dimensions of a semiconductor device structure are reduced to the point at which they are approaching the electron wavelength, the relevant physics changes to that of

quantum mechanics and unique structures known as 'quantum wells' exploit this fact. Improved lasers, photodiodes, modulators and switches have all been constructed using quantum wells. Here a brief introduction to the subject will be given together with it's possible relevance to acousto-optic devices. A full account of the electronic and optical properties of quantum well structures and their use in devices, can be found in several texts[83,84] and review articles[85,86].

A quantum well (QW) structure consists of one or more very thin layers (typically $\leq$ 100 Å) of narrow band gap material, sandwiched between barriers of wider bandgap material, providing electronic carrier confinement (e.g. Figure 1.5). The layers can be grown by either MBE[87] or MOCVD[88] techniques, and the technology has been particularly successful in the III-V structures such as GaAs/AlGaAs and InGaAsP/InP. It is the confinement of the charge carriers that leads to the observable quantum effects; the potential well provided by the difference in band gaps of the two constituent materials extends over a sufficiently small enough length to produce observable discreteness in the allowed energies of the charge carriers as given by the energy eigenvalues of the Schrödinger equation.

As a consequence of this quantization, the energy dependence of the density of states $\rho(E)$ for electrons and/or holes takes on a staircase form[89]. It is the modification of this density of states structure, brought about through variations in layer thicknesses and composition within the quantum well structure that can lead to methods of tailoring the optical properties.

1.5.2 Electronic and optical properties

1.5.2.1 The single quantum well

The determination of the electron and hole energy eigenvalues and wave functions is of fundamental importance to any analysis of the operation of a quantum well device. These quantities can be determined through use of the envelope function approximation[90] where the wave functions are separated into a slowly varying part and a part that varies on the lattice potential scale.

Figure 1.6 shows schematically the electron and hole energy levels in a single quantum well structure at $k=0$. This quantization is easily seen in an optical absorption spectrum where a series of steps is observed rather than the relatively smooth spectrum which is characteristic of bulk semiconductors. The transitions seen in the absorption spectrum correspond to those that are allowed by selection rules[91] that can be derived from investigations of the electric-dipole matrix elements. In addition there are strong absorption features at the edges of the steps in the spectrum, due to excitons, which are fundamental to the interaction of light with matter and are excited pairs of Coulomb attracted electrons and holes. In bulk materials excitons are relatively fragile and are barely resolvable at room temperature. In the quantum well there is an excitonic feature at the onset of each new sub-band structure, which in pure samples is twin peaked, revealing excitons that consist of two types of holes: known as heavy holes and light holes.

One of the most important applications of quantum wells comes from the modifications to their optical properties that follow the application of an electric field. For the case of a perpendicular electric field, first studied in 1982 by Mendez et al[92], the low lying electron and hole states are moved closer together in energy. The effect of the electric field on the one electron properties has been calculated from perturbation theory to second order[93], and leads to a quadratic reduction in the interband absorption energy with electric field. The applied electric field also has an effect on the excitonic properties and, unlike bulk semiconductors where the excitons are easily dissociated, here the electrons and holes are confined to the quantum well until very large electric fields are applied (typically 50 times that required for the same effect in bulk), i.e. the confinement provided by the QW is far more effective at keeping the electrons and holes in close proximity than the Coulomb interaction.

1.5.2.2 Multiple quantum wells and superlattices

If a structure consisting of many quantum wells layered on top of each other has barrier layers large enough such that the individual wells can be treated as independent (barriers typically >~100Å), the structure is known as a multiple quantum well (MQW). Typically there are ~50 quantum wells in a real MQW structure. The optical response should be ideally a simple multiple of the response of one of the quantum wells but unavoidable

variations in layer thickness in practice and other factors mean that the quantum wells within the structure are not in fact identical and the result is a broadening of the luminescence from such a structure. A similar effect can also be detrimental to the operation of devices which rely on electric fields across the MQW structure, where the electric field is perhaps not uniform over the structure.

If the structure has barriers that are not large enough to dispel any interaction between adjacent quantum wells then the structure is strictly known as a 'superlattice'. The simplest superlattice structure then is obviously a pair of quantum wells, and the energy levels and wave functions of such a structure can be found by considering the coupling between the two quantum wells within a perturbation theory approach[82]. This leads to a splitting of the energy levels, and if more quantum wells are added, the additional splitting leads eventually to a sequence of energy bands rather then discrete levels, in much the same way that the atoms of a crystal lattice affect the energy levels of their neighbours and produce a band structure, hence the term 'superlattice'. Superlattices have interesting optical and electronic properties, including possibilities for terahertz oscillations between coupled wells.[94]

1.5.2.3 Strain in quantum wells

If the bulk lattice constant of an epitaxial layer differs from that of the substrate on which it is grown, then the grown layer will be strained. Far from being a problem, this type of strained structure and the physics associated with it can be exploited in many electronic and optical devices. Extensive strain investigations have been performed on the $In_xGa_{1-x}As/GaAs$[95] and $Si_{1-x}Ge_x/Si$[96] material systems.

The introduction of strain into QW structures in this manner has implications for the band structure[97] of III-V materials since the strain breaks the cubic symmetry of the crystal structure and leads to lifting of the degeneracy of the heavy and light hole states at $k=0$, and anisotropy of the valence band structure. The variations of valence band structure that can be achieved through the incorporation of strain is large and can lead to improved performance in many electrical and optical devices. For example the ability to lower the effective mass of valence band sub-band states can lead to improved laser performance.

1.5.2.4 Acousto-optics of quantum wells and superlattices

Very little work has been published on the acousto-optics of quantum well and superlattice structures. The propagation of SAWs on GaAs/AlGaAs heterostructures has been studied experimentally and the interaction of the SAWs with the quasi-two dimensional inversion electron system considered[98]. It has been shown how the superlattice structure can be exploited to form a Fabry-Perot type resonator and subsequently produce retrodiffraction by ultrasonic waves to increase the acousto-optic interaction in such structures[99].

It is acknowledged that the direct use of the SAW induced acousto-optic effect has not been fully investigated or demonstrated for these type of structures. However a number of devices have been proposed that would utilise these effects[100,101,102].

1.5.3 Device technology

There are many device types which exploit the ideas of quantum confinement to improve device performance. The increased performance is a direct consequence of the physics associated with the structures.

The area of transistors has seen much progress through the use of multi-layer semiconductor structures. Transport of electrons in the active region of the device determines much of the device performance[103]. High-electron-mobility transistors (HEMT) exploit the mobility of the two-dimensional electron gas (2DEG) associated with confinement in a heterojunction[104] and heterojunctions in bipolar transistors (HBTs) lead to high speed devices[105].

In addition, the generation and detection of microwaves is an area where heterojunction and multi-layer semiconductor structures have been used extensively[106].

Heterostructures introduced into lasers[107] increase electron and hole density in the active region and provided better optical confinement leading to reduction in threshold current densities. In QW lasers the total number of carriers needed to obtain a given level of population inversion is reduced, as a result the free carrier absorption is reduced and the

threshold current density drops by around a factor of ten as compared to conventional heterostructure laser diodes. Only a single quantum well is required to realise the benefits of confinement in laser structures, and from a simple assumption of infinite barrier height, plots of density of states and gain as a function of photon energy can be obtained [108]. The advantages and operation of QW lasers are described in the text by Weisbuch and Vinter[82].

At sufficiently high injection current levels the gain of a single QW laser can be improved by adding more layers to produce an MQW laser. A further steep drop in threshold current density in QW lasers can be achieved by the incorporation of strain into the structure[109].

Practical applications of the electric field dependent optical properties of quantum wells are devices such as modulators and switches. The "Quantum confined Stark effect (QCSE)"[110] is very useful in such devices because moderate fields (~10^4 Vcm^{-1}) can cause significant changes in absorption[111]. The electro-absorption is approximately 50 times stronger in MQW structures than in bulk semiconductors where the Stark shift is masked by a broadening of the excitonic peak. Early QCSE modulators were made in GaAs/AlGaAs MQW structures [112,113], with the light introduced normal to the QW layers. The on-off ratio [114] of these devices was limited due to the small interaction length, and an effective way of getting round this problem was to use a waveguide modulator structure, with the light confined to propagate in the plane of the layers [115].

The strong electro-absorption effect in QW devices implies an electro-optic effect through the Kamers-Kronig relationship[116]. The relative strengths of the electro-absorption and electro-optic effects in MQW devices is very important, although it seems in general that the electro-optic effect is not large enough to significantly interfere with the operation of electro-absorption devices. Typical figures indicate that the electro-optic effect in MQW structures can be around 2 orders of magnitude[117] greater than bulk counterparts suggesting shorter interaction lengths in typical devices, such as phase modulators. The greatest advantage of the multiple-quantum-well modulator is probably the possibilities for monolithic integration with laser diodes. Such a device structure has been made in AlGaAs/GaAs by Tarucha and Okamoto.[118]

MQW structures can also be used advantageously in the fabrication of optical switches, by modifications to the dual channel directional coupler[119]. Strain can be introduced using deposited materials, such as gold strips which result in the refractive index profiles needed. Devices of this type suggest the possibility of all optical logic circuitry, capable of functioning without any electrical inputs or control signals.

The self-electro-optic device (SEED)[120] is a device with a principle of operation that depends on the optical properties of quantum wells. The QW structure is embedded in a *p-n* junction and acts as both a modulator and photodetector, resulting in an optically switchable bistable device, i.e. the diode is switched between a high absorption low voltage state and a low absorption high voltage state. The SEED is currently receiving much attention and many applications have been demonstrated[121,122].

1.6 SUMMARY

Chapter one has shown how acousto-optic techniques provide a versatile basis for device realisation together with how the subject has progressed through advances in SAW technology, optical waveguides and optoelectronic integrated circuits. It is clear that improvements in Bragg cell performance will extend that progression further in many device areas.

The fabrication techniques now available allow new structures such as quantum wells and multi-layered structures to be grown. There is clear justification then for looking at the applicability of such structures to acousto-optic applications, since devices have been proposed but not fabricated and theoretical work has not been exhaustive.

The rest of this thesis will show the modelling work that has been carried out in this area, starting from the propagation of SAWs on multi-layered structures, guided optical waves in multi-layered structures, and onto acousto-optic interactions and finally quantum mechanical effects.

References

[1] Brillouin, L. "Diffraction of light and X-rays by a transparent Homogeneous Body," Ann. Phys. (Paris), **17**, pp.88-122, (1922)

[2] Debye, P. and Sears, F.W. "On the scattering of light by supersonic waves," Proc. Nat. Acad. Sci. (US), **18**, pp.409-414, (1932)

[3] Lucas, R. and Biquard, P. "New optical properties produced in liquids by HF sound waves", J. Phys. Rad., **3**, pp.464-477, (1932)

[4] Slobodin, L. "Optical correlation technique for radar pulse compression," Proc. IEEE, **52**, p.842, (1964)

[5] Korpel, A., Adler, R. Desmares, P. and Watson, W. "A television display using acoustic deflection and modulation of coherent light," Proc. IEEE, **54**, pp.1429-1437, (1966)

[6] Whitman, R., Korpel, A. and Lotsoff, S. "Application of acoustic Bragg diffraction to optical processing techniques," Proc. Symp. Modern Optics, pp.243-255, (1967)

[7] Hunsperger, R.G. *Integrated Optics: Theory and Technology* Third Edition, Section 8.2, Springer-Verlag, (1991)

[8] Korpel, A. "Acousto-Optics - A Review of Fundamentals," Proc. IEEE, **69**, pp.48-53, (1981)

[9] Lieben, W. "Some applications of an ultrasonic light modulator," J. Ac. Soc. Am. **34**, pp.860-861, (1962)

[10] Rosenthal, A.H. "Application of ultrasonic light modulation to signal recording, display, analysis and communication," IRE Trans. Ultrason. Eng., **UE-8**, pp.1-5, (1961)

[11] King, M., Bennett, W.R., Lambert, L.B. and Arm, M. "Real time electro-optical signal processors with coherent detection," Appl. Opt., **6**, pp.1367-1375, (1967)

[12] Korpel, A. "An ultrasonic light deflection system," IEEE J. Quantum. Electron., **QE-1**, pp.60-61, (1965)

[13] Korpel, A., Lotsoff, S.N. and Whitman, R.L. "The Interchange of Time and Frequency in Television Displays," Proc. IEEE, **57**, (2), pp.160-170, (1969)

[14] Klein, W. and Cook, B. "Unified approach to ultrasonic light diffraction," IEEE Trans. Son. Ultrason., **SU-14**, pp.123-134, (1967)

[15] Chu, R.S. and Tamir, T. "Bragg diffraction of Gaussian beams by periodically modulated media," J. Opt. Soc. Am., **66**, pp.220-226, (1976)

[16] Chu, R.S. and Koy, J.A. "Diffraction of optical beams with arbitrary profile by a periodically modulated layer," J. Opt. Soc. Am, **70** (1), pp.1-6, (1980)

[17] Fleyry, P.A. "Light scattering as a probe of phonons and other excitations," in *Physical Acoustics, principles and methods*, Ed. Mason, W.P. and Thurston, R.N., Academic Press, London, (1970)

[18] Smith, T.M. and Korpel, A. "Measurement of light-sound interaction efficiencies in solids," IEEE J. Quantum. Electron., **QE-1**, pp.283-284, (1965)

[19] Pinnow, D. "Guide lines for selection of acoustooptic materials," IEEE J. Quantum. Electron., **QE-6**, pp.223-238, (1970)

[20] Uchida, N. and Niizeki, N. "Acoustooptic Deflection Materials and Techniques," Proc. IEEE, **61**, (8), pp.1073-1092, (1973)

[21] Tsai, C.S. *Guided wave acousto-optics, Interactions, devices and applications*, Springer series in Electronics and Photonics Vol.23, Springer, Berlin, New York (1990)

[22] Hunsperger, R.G. *Integrated Optics: Theory and Technology* Third edition, Springer-Verlag (1991)

[23] Tsai, C.S. "Integrated acoustooptic circuits and applications", IEEE Trans. Ultrason. Feroroelectrics and Freq. Control, **39**, (5), (1992)

[24] Sliwinski, A., "On acousto-optical examination of material properties," Proc. SPIE Int. Soc. Opt. Eng., **1844**, pp.141-154, (1992)

[25] Chang, I.C. "Acousto-optic devices and applications ," IEEE Trans. Son. Ultrason., **SU-23**, pp.2-22, (1976)

[26] Miller, D.A.B, "Quantum well optoelectronic switching devices," Int. J. High Speed. Electron. **1**, pp.19-46, (1990)

[27] Hook, J.R. and Hall, H.E. *Solid State Physics* 2nd edition, Chapter 2, John Wiley and Sons. (1991)

[28] Sapriel, J. *Acousto-Optics* page 14, John Wiley & Sons (1979)

[29] Nye, J.F. *Physical properties of crystals* Clarenden, Oxford (1960)

[30] Lord Rayleigh "On waves propagated along the plane surface of an elastic solid," London Math. Proc., **17**,(4), pp.4-11, (1885)

[31] Sapriel, J. *Acousto-Optics* Page 21, John Wiley & Sons, (1979)

[32] Bright, V.M., Kim, Y. and Hunt, W.D. "Study of surface acoustic waves on the {110} plane of gallium arsenide," J. Appl. Phys., **71**, pp.597-605, (1992)

[33] Bright, V.M. and Hunt, W.D. "Bleustein-Gulyaev waves in gallium arsenide and other piezoelectric cubic crystals," J. Appl. Phys., **66**, pp.1556-1564, (1989)

[34] Hecht, E. *Optics* Chapter 3, 2nd Edition, Addison-Wesley, (1987)

[35] Nelson, D.F. and Lax, M., "New symmetry for acousto-optic scattering," Phys. Rev. Lett., **24**, pp.379-380, (1970)

[36] See, for example, Sapriel, J. *Acousto-Optics* Page 49, John Wiley & Sons, (1979)

[37] Raman, C.V. and Nagendra Nath, N.S., "The diffraction of light by high frequency sound waves", Proc. Ind. Acad. Sci., **2**, pp.406-420, (1935); **3**, pp.75-84, (1936); **3**, pp.119-125, (1936); **3**, pp.459-465, (1936)

[38] Yariv, A "Coupled-Mode Theory for Guided-Wave Optics," IEEE J. Quantum Electron., **QE-9**, pp.919-933, (1973)

[39] Gordon, E.I. "Figure of merit for acousto-optical deflection and modulation devices," IEEE J. Quantum. Electron., **QE-2**, pp.104-105, (1966)

[40] Harris, S.E. and Wallace, R.W., "Acousto-optic tunable filter," J. Opt. Soc. Am., **59**, pp.744-747, (1969)

[41] Aronson, L.B., Rankin, G. Trutner, W.R. and Dolfi, D.W. "Reduced sidelobe integrated acousto-optic filter with birefringence apodization," Opt. Lett. **18**, pp.1721-1723, (1993)

[42] Fermann, M.E., da Silva, V., Smith, D.A., Silberberg, Y. and Weiner, A.M. "Shaping of ultrashort optical pulses by using an integrated acousto-optic tunable filter," Opt. Lett., **18**, pp.1505-1507, (1993)

[43] Hartman, C.S., "Variable bandwidth-variable center frequency surface wave bandpass filter," Proc. Ultrasonic Symp., pp.21-215, (1972)

[44] Brackelsby, C.J., Palfreeman, J.S. and Gibson, R.W. *Ultrasonic delay lines*, ILIFFE books Ltd., London, (1963)

[45] Milstein, L.B. and Das, P.K., "Surface acoustic wave devices," IEEE Commun. Mag. pp.25-33, September, (1979)

[46] Tancrell, R.H. "Analytic design of surface wave bandpass filters," IEEE Trans. Sonics and Ultrason., **SU-21**, (1), pp.12-22, (1974)

[47] Jack, M.A., Grant, P.M., and Collins, J.M. "The theory design and applications of surface acoustic wave fourier transform processors," Proc. IEEE, **68**, (4), pp.450-468, (1980)

[48] Barnard, M.E., Bloch, P.D., and Paige, E.G.S. "A novel SAW spectrum analyser," IEEE Intern. Workshop. WIORT-84, Florence, Italy (1984)

[49] Kino, G.S. "Acousto-electric interactions in acoustic surface wave devices," Proc. IEEE, **60**, pp.724-748 (1978)

[50] Wang, W.C. and Das, P. "Surface wave convolver via space charge non-linearity", Proc. IEEE Ultrasonic. Symp., pp.310 (1972)

[51] Kaminow, I.P., Ramaswamy, V., Schmidt, R.V., and Turner, F.H., "Lithium Niobate ridge waveguide modulator" Appl. Phys. Lett. **24**, pp.622-624, (1974)

[52] Hall, D., Yariv, E. and Garmie, E. "Observation of propagation cutoff and it's control in thin optical waveguides," Appl. Phys. Lett., **17**, pp.127-129, (1970)

[53] See, for example, Pankove, J.I. *Optical Processes in Semiconductors*, Prentice-Hall, Englewood Cliffs, Page 29 (1971)

[54] Campbell, J.C., Blum, F.A., Shaw, D.W. and Lawley, K.L. "GaAs electro-optic directional coupler switch," Appl. Phys. Lett., **27**, pp202-205, (1975)

[55] Hammer, J.M. and Channin., D.J. "Simple acoustic grating modulator," Appl. Opt., **11**, (10), pp.2203-2209 (1972)

[56] Lee, Y.K., and Wang, S. "Electrooptic Bragg-deflection modulators: theoretical and experimental studies," Appl. Opt., **15**, (6), pp.1565-1572, (1976)

[57] Kuhn, L., Dakss, M.L., Heidrich, P.F. and Scott, B.A., "Deflection of an optical guided wave by a surface acoustic wave," Appl. Phys. Lett., **17**, pp.265-267, (1970)

[58] Schmidt, R.V., Kaminow, I.P. and Carruthers, J.R., "Acousto-optic diffraction of guided optical waves in $LiNbO_3$," Appl. Phys. Lett. **23**, pp.417-419, (1973)

[59] Loh, K.W., Chang, W.S.C. Smith, W.R. and Grudowski, T. "Bragg coupling efficiency for guided acoustooptic interaction in GaAs," Appl. Opt. **15**, pp.156-166, (1976)

[60] Chu, R.S. and Tamir, T., "Guided wave theory of light diffraction by acoustic microwaves," IEEE Trans., **MTT-18**, pp.486-504, (1970)

[61] Kuhn, L, Hiedrich, P. and Lean, E., "Optical guided wave mode conversion by an acoustic surface wave," Appl. Phys. Lett., **19**, pp.428-430, (1971)

[62] Brandt, G.B., Gottlieb. M., and Conroy, J.S., "Bulk acoustic wave interaction with guided optical wave," Appl. Phys. Lett., **23**, pp53-54, (1973)

[63] Tsai, C.S., Alhaider, M.A., Nguyen, Le T. and Kim, B. "Wide-band Guided-wave Acoustooptic Bragg Diffraction and Devices Using Multiple Tilted Surface Acoustic Wave," Proc. IEEE, **64**, pp.318-328 (1976)

[64] Kissa, K., Wang, X., Ih, C.S. and Hunsperger, R.G. "Novel Integrated-Optic Modulator for Optical communications," Technical digest of the OSA Opticon '88 Symposium, Santa Clara, CA p.MK3, (30oct- 4 nov 1988)

[65] Ih, C.S., Hunsperger, R.G., Kramer, J.J., Tian, R., Wang, X., Kissa, K.and Butler, J.,"A novel modulation system for optical communications," Proc. SPIE, **876,** pp.30-38, (1988)

[66] Tsai, C.S., Zang, D.Y., and Le, P. "Acousto-optic Bragg diffraction in a $LiNbO_3$ channel-planar composite waveguide with application to optical computing," Appl. Phys. Lett., **47**, pp.549-551, (1985)

[67] Scmidth, R.V. and Kaminow, I.P. "Metal-diffused optical waveguide in $LiNbO_3$", Appl. Phys. Lett., **25**, pp.458-460, (1974)

[68] Zang, D.Y., and Tsai, C.S. "Single-mode waveguide microlens and microlens arrays fabricated in $LiNbO_3$ using titanium indiffused proton exchanged technique," Appl. Phys. Lett., **46,** pp.703-705, (1985)

[69] Zang, D.Y., and Tsai, C.S. "Titanium indiffused proton exchanged waveguide lenses in $LiNbO_3$ for optical information processing," App. Opt., **25**, Special issue on optical computing, pp.2264-2271, (1986)

[70] Jackel, J.L., Rice, C.E. and Veslka, J.J. "Proton-exchange for high index waveguiding in $LiNbO_3$," Appl. Phys. Lett. **41**, pp.607-608, (1982)

[71] Vu, T.Q., Norris, J.A., and Tsai, C.S. "Planar waveguide lenses in GaAs using ion milling," Appl. Phys. Lett., **54**, pp.1098-1100, (1989)

[72] Lewis, M.F., West, C.L., Deacon, J.M. and Humphreys, R.F. "Recent developments in SAW devices," IEE Proc., **131**, pp.186-215, (1984)

[73] Yariv, A. "The Beginning of Integrated Optoelectronic Circuits," IEEE Trans. Electron. Dev., **ED-31**, (11) pp.1656-1661, (1984)

[74] Wada, O., Sakurai, T. and Nakagami, T. "Recent progress in Optoelectronic Integrated Circuits (OEIC's)," IEEE J. Quantum. Electron., **QE-22**, (6), pp.805-8219, (1986)

[75] Suematsu, Y., Yamada, M. and Hayashi, K. "Integrated Twin-Guide AlGaAs laser with Multiheterostructure," IEEE J. Quantum. Electron., **QE-11**, (7), pp.457-460, (1975)

[76] Suematsu, Y. "Advances in Semiconductor lasers," Physics today, **38**, (5), pp.32-39, (1985)

[77] Lii, C.J., Tsai, C.S., Lee, C.C. and Abdelrazek, Y.A. "Wideband acoustooptic Bragg cells in GaAs waveguide," Proc. Ultrason. Symp. pp.429-433, (1986)

[78] Valette, S., Lizet, J., Mottier, P. et al. "Integrated optical spectrum analyser using planar technology on oxidised silicon substrate," Electron. Lett., **19**, (21), pp.883-885, (1983)

[79] Suhara,T. Shiono,T., Nishihara, H. and Koyama, J. "An integrated-optic Fourier processor using an acoustooptic deflector and Fresnel lenses in an As_2S_3 waveguide," IEEE J. Lightwave. Technol., **LT-1**, (4), pp.625-629, (1983)

[80] Alippi, A., Palma, A., Palmieri, L., Socino, G. and Verona, E. "Time integrating acousto-optical correlator based on light polarization processing," Opt. Commun., **40**, pp.19-22, (1981)

[81] Reeve, C.D. and Wombwell, J.F. "Novel space-integrating acoustooptic correlator - amplitude and phase information from intensity only measurements," IEE Proc. Radar and signal processing, **136**, pp.185-190, (1989)

[82] Abdelrazek, Y. and Tsai, C.S. "High-performance acoustooptic Bragg cells in ZnO-GaAs waveguide at GHz frequencies," OPTOELECTRONICS-Devices and technologies, **4**, pp33-37, (1989)

[83] Weisbuch, C. and Vinter, B. *Quantum semiconductor structures* Academic press New York, (1991)

[84] Kelly, M.J. *Low-dimensional semiconductor structures, materials, physics, technology, devices,* Clarendon Press, Oxford, (1995)

[85] Esaki, L., "The evolution of semiconductor superlattices and quantum wells," Int. J. Mod. Phys., **B3,** pp.487-507, (1989)

[86] Schmitt-Rink, S., Chemla, D.S., and Miller, D.A.B., "Linear and nonlinear optical properties of semiconductor quantum wells," Advances in Physics, **38**, pp.89-188, (1989)

[87] Chang, L.L. and Ploog, K.(ed). *Molecular beam epitaxy and heterostructures.* Martinus Nijhof, Dordrecht, (1985)

[88] Razeghi, M. *The MOCVD challenge.* Adam Hilger, Bristol, (1989)

[89] Okamoto, H. "Semiconductor Quantum-Well Structures for Optoelectronics :- Recent advances and Future Prospects," Jap. J. Appl. Phys., **26**, (3), pp.315-330, (1987)

[90] See, for example Chow, W.W., Koch, S.W. and Sargent III, M. *Semiconductor-Laser Physics* Page 192, Springer-Verlag, (1994)

[91] See, for example Weisbuch, C. and Vinter, B. *Quantum semiconductor structures* Page 65, Academic press New York, (1991)

[92] Mendez, E.E., Bastard, G., Chang, L.L., Esaki, L., Morkoç, H. and Fischer, R.,"Electric field-induced quenching of luminescence in quantum wells" Physica, **117-118,** pp.711-713, (1983)

[93] Miller, D.A.B., Chemla, D.S., Damen, T.C., Gossard, A.C., Wiegmann, W., Wood, T.H., and Burrus, C.A. "Electric field dependence of optical absorption near the bandgap of quantum well structures," App. Phys. Lett., **41**, pp.679-681, (1985)

[94] Roskos, H.G., Nuss, M.C., Shah, J., Leo, K., Miller, D.A.B., Fox, A.M., et al. "Coherent submillimetre wave emission from charge oscillation in a double well potential," Phys. Rev. Lett., **68**, pp.2216-2219, (1992)

[95] Fritz, I.J., Picraux, S.T., Dawson, L.R., Drummond, T.J., Laidig, W.D., and Anderson, N.G., "Dependence of critical layer thickness on strain for $In_xGa_{1-x}As/GaAs$ strained layer superlattices," Appl. Phys. Lett., **46**, pp.967-969, (1985)

[96] Bean, J.C., Feldman, L.C., Fiory, A.T., Nakahara, S., and Robinson, I.K. "Ge_xSi_{1-x}/Si strained layer superlattices grown by molecular beam epitaxy," J. Vac. Sci. Technol. A, **2**, pp.436-440, (1984)

[97] O'Reilly, E.P. "Valence band engineering in strained layer structures," Semiconductor Sci. Technol., **4**, pp.121-127, (1989)

[98] Wixforth, A., Scribe, J. Wassermeier, M. Kotthaus, J.P., Weimann, G. and Schlapp, W. "Surface acoustic waves on GaAs/AlGaAs heterostructures," Phys. Rev. B, **40**, pp.7874-7887, (1989)

[99] Renosi, P. and Sapriel, J.S. "Acousto-optics of semiconductor crystals and superlattices in resonance conditions," Ultrasonics, **31**, pp.327-332, (1993).

[100] Bhattacharjee, K.K. and Jain, F.C. "Multiple quantum well acousto-optic and electro-optic modulators," Proc. Ultrason. Symp. pp.621-624, (1990)

[101] Bhattacharjee, K.K. and Jain, F.C. "Multiple Quantum well Optical Modulator Structures Using Surface Acoustic Wave Induced Stark Effect," IEEE Photon. Technol. Lett. **1**, pp.307-309, (1989)

[102] Gryba, T. and Lefebvre, J.E. "Optimisation of MQW structures for acousto-optic absorption modulators," IEE Proc. Optoelctron., **141**, pp.62-64, (1994)

[103] Ladbrooke, P.H. "Comparison of transistors for monolithic microwave and millimetre wave integrated circuits," GEC Journal of Research, **4**, pp.115-125, (1986)

[104] Pearton, S.J. and Shah, N.J., "Heterostructure field effect transistors" In *High speed semiconductor devices* (ed S.M.Sze), pp.283-334. Wiley, New York. (1990)

[105] Ashbeck, P.M. "Bipolar transistors" In *High speed semiconductor devices*, (ed. S.M.Sze), pp.335-397 Wiley, New York, (1990)

[106] See, for example Chapter 17 "Devices II: microwave diodes" in Kelly, M.J. *Low-Dimensional semiconductors, materials, physics, technology, devices*, Clarendon press, Oxford, (1995)

[107] Casey, H.C. and Panish, M.B. *Heterostructure lasers*. Academic Press, New York, (1978)

[108] Yariv, A. *Quantum Electronics*, 3rd Edition Wiley New York (1988)

[109] Adams, A.R., "Band-structure engineering for low-threshold high efficiency semiconductor lasers." Electron. Lett., **22**, pp.249-250 (1986)

[110] Miller, D.A.B., Chemla, D.S., Damen, T.C, Gossard, A.C., Wiegmann, W., Wood, T.H. and Burrus, L.A. "Bandedge Electroabsorption in Quantum Well structures : the Quantum Confined Stark Effect," Phys. Rev. Lett., **53**, pp.2173-2176, (1984)

[111] Chemla, D.S., Damen, T.C., Miller, D.A.B., Gossard, A.C. and Wiegmann, W. "Electroabsorption by Stark effect on room temperature excitons in GaAs/GaAlAs multiple quantum well structures," Appl. Phys. Lett., **42**, pp.864-866, (1983)

[112] Wood, T.H., Burrus, C.A., Miller, D.A.B., Chemla, D.S., Damen, T.C., Gossard, A.C. and Wiegmann, W. "131ps optical modulator in semiconductor multiple quantm wells (MQWs)," IEEE J. Quantum. Electron., **QE-21**, pp.117-118, (1985)

[113] Miller, D.A.B., Chemla, D.S., Damen, T.C., Gossard, A.C., Wiegmann, W., Wood, T.H. and Burrus, L.A. "Electric field dependence of optical absorption near the band gap of quantum well structures,", Phys. Rev. B, **32**, pp.1043-1060, (1985)

[114] Wood, T.H. "Multiple Quantum well (MQW) waveguide modulators," IEEE J. Lightwave. Technol., **LT-6**, (6), pp.743-757, (1988)

[115] Wood, T.H., Burrus, C.A., Tucker, R.S., Weiner, J.S., Miller, D.A.B., Chemla, D.S., Damen, T.C., Gossard, A.C. and Wiegmann, W. "100 ps Waveguide multiple quantum well (MQW) optical modulator with 10:1 on/off ratio," Electron. Lett., **21**, (16), pp.693-694, (1985)

[116] Klingshirn, C.F. *Semiconductor Optics*, Chapter 8. Springer-Verlag Berlin Heidelberg (1995)

[117] Wood, T.H., Tkach, R.W. and Charaplyvy, A.R. "Observation of large quadratic electro-optic effect in GaAs/AlGaAs multiple quantum wells," Appl. Phys. Lett., **50**, (13), pp.798-800, (1987)

[118] Tarucha, S. and Okamoto, H. "Monolithic integration of a laser diode and an optical waveguide modulator having a GaAs/AlGaAs quantum well double heterostructure," Appl. Phys. Lett., **48**, pp.1-3, (1986)

[119] Wa, P.Li Kam, Sitch, J.E., Mason, N.J., Roberts, J.S., and Robson, P.N. "All optical multiple-quantum-well waveguide switch," Electron. Lett., **21**, pp.26-28, (1985)

[120] Miller, D.A.B., Chemla, D.S., Damen, T.C., Gossard, A.C., Weigmann, W., Wood, T.H., and Burrus, C.A., "Novel hybrid optically bistable switch: the quantum well self-electr-optic-effect device," Appl. Phys. Lett., **45**, pp.13-15, (1984)

[121] Giles, C.R., Wood, T.H. and Burrus, C.A. "Quantum well SEED optical oscillators," IEEE J. Quantum Electron., **QE-26**, pp512-517, (1990)

[122] Keyworth, B.P., Cada, M., Glinski, J.M., Springthorpe, A.J., Rolland, C., and Hil, K.O. "Multiple quantum well directional coupler as a self-electro-optic-effect device," Electron. Lett., **26**, pp.2011-2013, (1990)

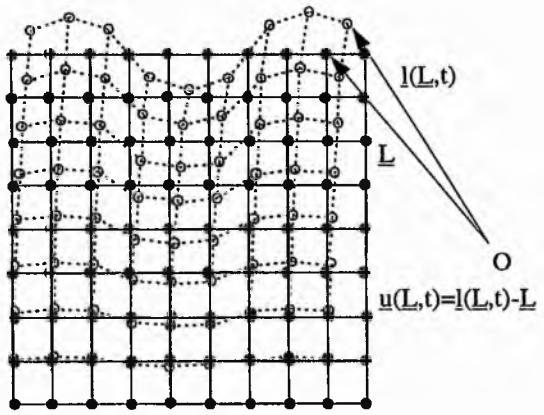

Figure 1.1 *Schematic diagram of particle displacement vector* $\underline{u}(\underline{L},t)$*, due to the deformation casued by the passage of a SAW*

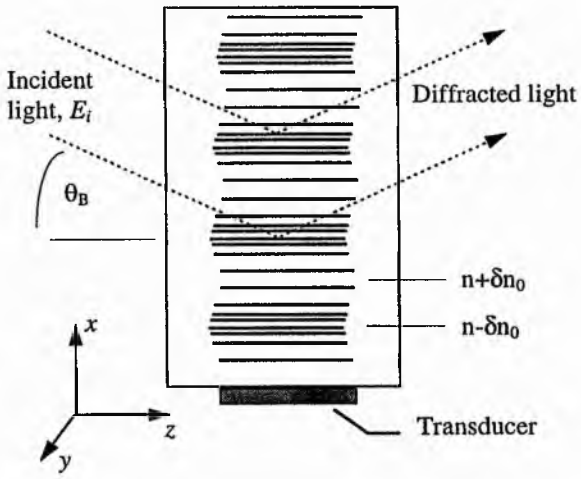

Figure 1.2 *Schematic diagram of the diffraction of light by ultrasound.* θ_B *is the Bragg angle*

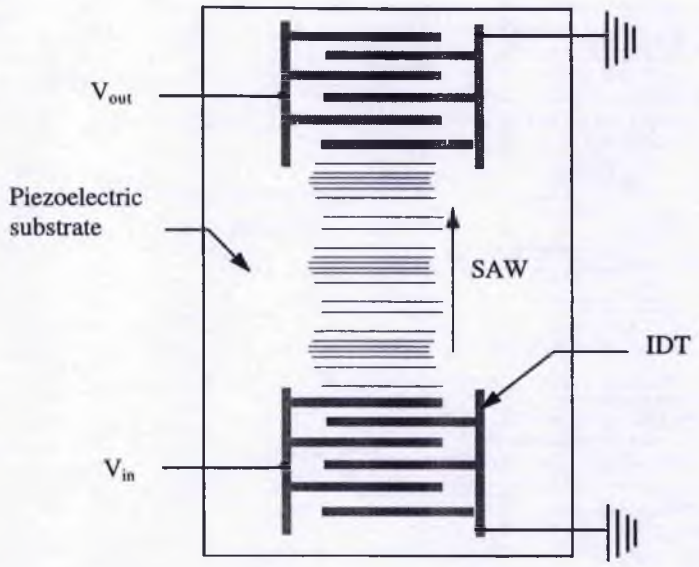

Figure 1.3 *Schematic diagram of the generation and detection of SAWs on a piezoelectric substrate, using interdigital transducers (IDTs)*

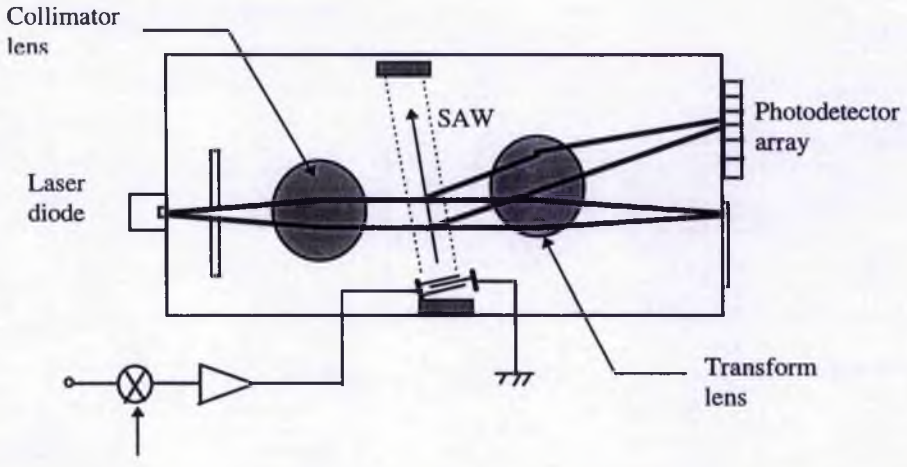

Figure 1.4. *Schematic diagram of the operation of an integrated acousto-optic spectrum analyser*

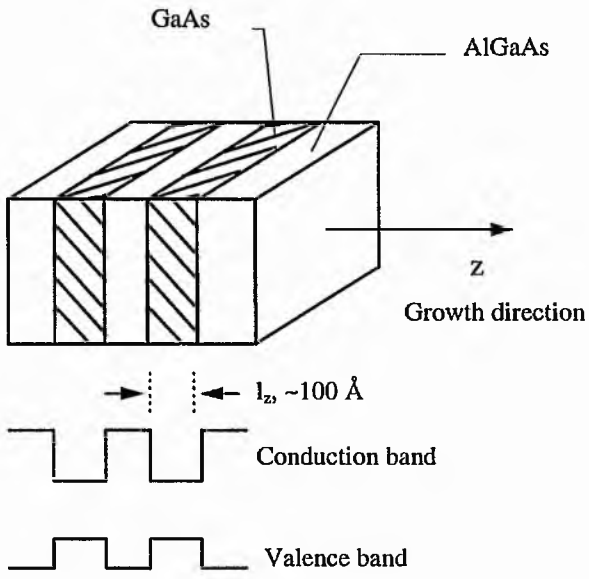

Figure 1.5 *AlGaAs/GaAs quantum well structure and schematic view of the confinement potential provided by the band gap discontinuities.*

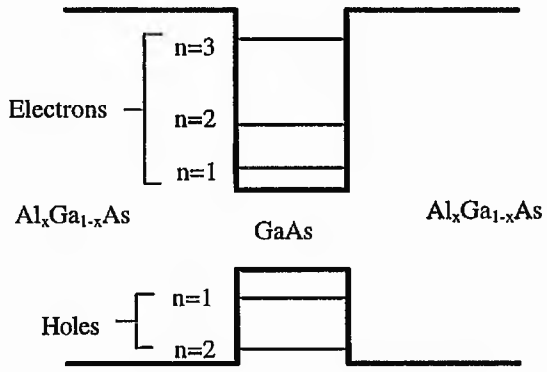

Figure 1.6 *Example of the electron/hole energy levels at k=0 in a single AlGaAs/GaAs quantum well.*

Chapter 2.

Surface Acoustic Wave Propagation on Layered Semiconductor Structures

2.1 INTRODUCTION

The passage of an acoustic wave through a layered semiconductor structure will alter the optical characteristics of that structure through the electro-optic and elasto-optic effects. Consequently any investigation of the interaction of guided optical beams with surface acoustic waves (SAWs) in appropriate device structures must first be concerned with the nature of the SAW induced field quantities (i.e. the fields that alter the refractive index), and the effect on these field quantities of altering the dimensions and composition of the material structure for a given SAW propagation. With the advent of new material structures such as quantum wells (QWs)[1], as mentioned in chapter 1, the possibility of increasing the efficiency of present acousto-optic devices has become apparent through the relatively large optical absorption (and correspondingly large electro-optic effect) provided by these structures at characteristic frequencies and several authors have proposed devices that utilise these effects [2,3]. Any investigation that proposes to model the induced field quantities in appropriate structures must therefore be applicable to layered structures and possible QW structures.

There are various ways to approach the problem of modelling SAWs on top of multi-layered structures including vector methods[4], matching the fields at layer interfaces and solving the resulting linear algebra problem[5] and closely related methods involving matrices[6]. The propagation of SAWs on GaAs and other III-V bulk materials has been studied theoretically for various crystallographic geometries and wave types in both the bulk material[7,8,9,10] and layered structures[11,12].

The Laguerre polynomial method which was first applied to SAWs guided in wedges[13] and has subsequently been applied to layered structures[14], including layers of different composition[15] will be used here to study structures of arbitrary layer thickness and composition.[16] The method is non-iterative and simple to program.

2.2 SURFACE ACOUSTIC WAVES ON APPROPRIATE DEVICE STRUCTURES

2.2.1 Theory

The theory is expressed within the conceptual framework outlined in chapter 1.

2.2.1.1 Propagation of piezoelectric surface waves

In the case of piezoelectric media such as we are considering here, we expect any stresses to be accompanied by an electric field and hence we have an additional constraint on the field quantities, namely that the electric field must obey the relevant Maxwell's equation, (in the absence of free charges);

$$\nabla . \boldsymbol{D} = 0 \qquad \text{-(2.1)}$$

The 'quasi-static' approach is taken here in which the appropriate acoustic velocities are

assumed to be much less than the velocity of electromagnetic waves, producing an effective assumption of a constant electromagnetic field. Equation (2.1) together with the equation of motion;

$$\frac{\partial T_{ij}}{\partial x_j} = \rho \frac{\partial^2 u_i}{\partial t^2} \qquad \text{-(2.2)}$$

govern the wave propagation in piezoelectric media. $\boldsymbol{D}$ is the electric displacement vector, ρ is the mass density and u the particle displacement (the conceptual nature of which was explained in section 1.2) for an assumed homogeneous medium.

The equations of piezoelectricity are written

$$T_{ij} = c^{E}_{ijkl} \frac{\partial u_k}{\partial x_l} + e_{lij} \frac{\partial \phi}{\partial x_l} \qquad \text{-(2.3)}$$

$$D_j = e_{jkl} \frac{\partial u_k}{\partial x_l} - \varepsilon^{s}_{jl} \frac{\partial \phi}{\partial x_l} \qquad \text{-(2.4)}$$

where ϕ is the electric potential. The relevant physical properties are c, the stiffness tensor, e the piezoelectric tensor, and ε the permittivity tensor. Note that here, in the case of piezoelectric materials, the stress is dependent on the electric field and the electric displacement is dependent on the strain. The superscript E labels stiffness in zero electric field and S labels permittivity with zero strain.

The modification of the stress tensor (Equation. (2.3)) together with the expression for the electric displacement (Equation (2.4)) lead through substitution in Equations (2.1) and (2.2), to two coupled wave equations that must be simultaneously obeyed; the boundary conditions can then be applied and the corresponding wave equations solved for the particle displacement and electric potential.

If a general Rayleigh wave form solution is assumed, and substituted into the coupled wave equations, a determinantal equation is obtained, for which it is important to note that for any

particular propagation direction, there are three corresponding particle displacements, u_i (i = 1, 2, 3), which are mutually orthogonal, and each will have a corresponding angular frequency. When one of the orthogonal particle displacements is parallel to the wavevector of the SAW, the acoustic wave is said to be longitudinal, and obviously in this case the other two particle displacements are normal and the waves associated with them are said to be transverse.

Surface waves are generally present to a depth of one wavelength below the surface of the propagation medium. The velocity of propagation of a surface wave is always less than that of volume waves in a given material. This is sensible since if we assume the material to be bounded by air, the particles found at the surface only exert forces of elastic cohesion on one side, providing the illusion that the surface wave experiences a medium of lower stiffness.

Closer inspection of the determinantal problem will reveal which modes involve coupling of the particle displacement and electric potential and hence can be excited piezoelectrically. For example, in the case of SAWs on the {100} planes of Gallium Arsenide, for propagation in the [100] direction the following determinantal type equation is obtained;

$$\begin{pmatrix} M_{11} & 0 & 0 & M_{14} \\ 0 & M_{22} & M_{23} & 0 \\ 0 & M_{32} & M_{33} & 0 \\ M_{41} & 0 & 0 & M_{44} \end{pmatrix} \begin{pmatrix} u_1 \\ u_2 \\ u_3 \\ \phi \end{pmatrix} = 0 \qquad \text{-(2.5)}$$

where the [M] matrix contains large expressions involving material constants and decay factors. However, in the case of propagation in the [110] direction the following is obtained;

$$\begin{pmatrix} M_{11} & 0 & 0 & 0 \\ 0 & M_{22} & M_{23} & M_{24} \\ 0 & M_{32} & M_{33} & M_{34} \\ 0 & M_{42} & M_{43} & M_{44} \end{pmatrix} \begin{pmatrix} u_1 \\ u_2 \\ u_3 \\ \phi \end{pmatrix} = 0 \qquad \text{-(2.6)}$$

Comparing Equations (2.5) and (2.6) it can be seen that for the first case of propagation in the [100] direction only the u_1 particle displacement is coupled to the electric potential ϕ, the

other two particle displacements being coupled together as pure Rayleigh waves, hence in this case only the transverse mode has the possibility of being excited piezoelectrically and is known as a 'Bleustein-Gulyaev' wave[17], but for this particular propagation direction it can be shown that this mode does not exist[18]. For the second case (Equation (2.6)) it can be seen that one of the modes cannot be excited piezoelectrically as it is decoupled from the electric potential, however three modes appear to exist that couple u_2, u_3 and ϕ and hence should be able to be excited piezoelectrically. Using the fact that the determinant of the [M] matrix should be put to zero, a polynomial equation can then be solved for example by using a Newton-Raphson method or some other root finding method and the decay constants can be obtained. This is the standard approach to the numerical modelling of SAWs in piezoelectric media and is not used in it's full form here, since the problem is further complicated by the presence of multiple layers of differing compositions.

2.2.1.2 Multi-layer structures

In the case of multi-layered structures the situation is much more complex, and boundary conditions must be matched at interfaces, leading to great complexity when the number of layers becomes large.

The justification behind using a Laguerre polynomial technique is quite apparent. The Laguerre polynomials form an orthonormal basis set for the half space $x \geq 0$, and in this case we would use the depth below the surface as representing x. Laguerre polynomials are commonly used for example in the representation of the radial part of Hydrogen like wave functions[19]. The first five functions used in the expansion of the field quantities are shown in Figure 2.1, $f(x)$ in this case represents a particular Laguerre polynomial multiplied by exp(-$x/2$). The orthonormality of the polynomials is expressed through the overlap function ;

$$\int_{-\infty}^{+\infty} L_i(x) L_j(x) = \delta_{ij} \qquad \text{-(2.7)}$$

which can be thought of as representing a scalar product on an appropriate vector space. δ_{ij} represents the Kronecker delta function.

The material structure is represented in Figure 2.2, each layer being characterised by the physical properties of stiffness, permittivity, piezoelectric constant and the mass density, ρ .

2.2.1.3 Co-ordinate systems

The co-ordinate system adopted is one in which the surface wave propagates in the x_1 direction and the x_2 direction represents the depth below the surface. The SAW is assumed to propagate in the [110] direction on the {100} plane, since this configuration provides a high electromechanical coupling constant for structures such as GaAs and AlGaAs[12]. Since the material tensors are defined with respect to the crystallographic axes, their components must be transformed so that they may be expressed in the co-ordinate system adopted. The material tensors were transformed according to Auld[20], which is based on the fact that all tensors transform as products of vectors[21], and given the transformation matrix of the crystallographic axes, conditions on the elements of the transformation matrices for all tensors can be derived. For example, the stress tensor, T, is a two index tensor and hence would transform according to

$$T'_{kl} = a_{ki} a_{lj} T_{ij} \qquad \text{-(2.8)}$$

where the a's are the sets of numbers that transform each component of each index of the tensor. Equation (2.8) can be re-written in reduced index form as

$$T'_m = M_{mn} T_n \qquad \text{-(2.9)}$$

(i.e. two indices running form 1 to 3 can be reduced to 1 index running from 1 to 6) with the two stress tensors being related through a single 6×6 matrix, [M] whose elements are derived from the elements of the matrix representing the product of the two a matrices in Equation (2.8). The transformation of the stiffness tensor can then be carried out in reduced index form and can be written in terms of the matrix [M] as

$$[c]' = [M][c][M]^T \qquad \text{-(2.10)}$$

where [c] is the matrix representing the stiffness tensor in reduced index form. Considering just the stiffness tensor, before transformation is performed, the matrix [c] has the following form;

$$\begin{pmatrix} c_{11} & c_{12} & c_{12} & 0 & 0 & 0 \\ c_{12} & c_{11} & c_{12} & 0 & 0 & 0 \\ c_{12} & c_{12} & c_{11} & 0 & 0 & 0 \\ 0 & 0 & 0 & c_{44} & 0 & 0 \\ 0 & 0 & 0 & 0 & c_{44} & 0 \\ 0 & 0 & 0 & 0 & 0 & c_{44} \end{pmatrix} \qquad \text{-(2.11)}$$

which is the standard reduced index form (i.e. the four indices of the tensor have been reduced, through symmetry to two indices each running from 1 to 6) of a material with a zinc blende crystal structure. Note that the matrix has only three independent elements.

The transformation that was performed on the tensors was one in which the crystallographic axes were first rotated through 90° about the x axis, transforming the z axis into the y axis and the y axis into the -z axis, and then rotated by 45° about the new y axis (see Figure 2.3). The SAW would then be assumed to be propagating in the x'' direction (i.e. the [110] direction). After applying the first transformation (rotation through 90° about the x axis) of the stiffness tensor it will be unchanged since any physical property must possess the crystallographic point group symmetries and after application of the second transformation it has the following form;

$$\begin{pmatrix} c' & c_{12} & c'' & 0 & 0 & 0 \\ c_{12} & c_{11} & c_{12} & 0 & 0 & 0 \\ c'' & c_{12} & c' & 0 & 0 & 0 \\ 0 & 0 & 0 & c_{44} & 0 & 0 \\ 0 & 0 & 0 & 0 & c''' & 0 \\ 0 & 0 & 0 & 0 & 0 & c_{44} \end{pmatrix} \qquad \text{-(2.12)}$$

where $c' = 1/2(c_{11}+c_{12})+c_{44}$, $c'' = 1/2(c_{11}+c_{12})-c_{44}$ and $c''' = (c_{11}-c_{12})/2$. Note how certain rows and columns of the stiffness matrix are unchanged under this transformation, reflecting

the fact that some of the axes of the co-ordinate system still lie along one of the three equivalent crystallographic directions in this cubic structure. Similar matrices were also derived for the piezoelectric tensor and the permittivity tensor, through the use of similar techniques to derive transformation equations, that are outlined in the text by Auld[20].

2.2.1.4 Boundary conditions and the eigen-problem

The boundary conditions for the propagation of SAWs on top of piezoelectric structures are that the normal component of the stress should vanish at the surface together with the continuity of the electric potential and normal component of electric displacement at each interface. Boundary conditions are incorporated by using the step function $\theta(x)$, which is also used to represent the effective material tensors of the layered structure :

$$c_{ijkl}^{M} = c_{ijkl}^{1} + \sum_{L=1}^{N} (c_{ijkl}^{L} - c_{ijkl}^{L-1})\theta(q_2 - kh_L) \qquad \text{-(2.13)}$$

$$e_{lij}^{M} = e_{lij}^{1} + \sum_{L=1}^{N} (e_{lij}^{L} - e_{lij}^{L-1})\theta(q_2 - kh_L) \qquad \text{-(2.14)}$$

$$\varepsilon_{jl}^{M} = \varepsilon_{jl}^{1} + \sum_{L=1}^{N} (\varepsilon_{jl}^{L} - \varepsilon_{jl}^{L-1})\theta(q_2 - kh_L) \qquad \text{-(2.15)}$$

$$\rho^{M} = \varepsilon^{1} + \sum_{L=1}^{N} (\rho^{L} - \rho^{L-1})\theta(q_2 - kh_L) \qquad \text{-(2.16)}$$

where N represents the number of layers and L labels each layer. The superscript M stands for 'multi-layer' and indicates that these material quantities are 'effective', and q represents a change of variable from x_i to kx_i where k is the magnitude of the wave vector in the propagation direction.

If we assume generic solutions for the particle displacements and the electric potentials, having the form of a plane propagating wave in the x_1 direction, with an $e^{i\omega t}$ time dependence and an amplitude that is a function of depth, then after inserting the modified material tensors into the equations of piezoelectricity, the two coupled wave equations can be re-written ;

$$\frac{\omega^2}{k^2}\left(\rho^1 + \sum_{L=1}^{N}(\rho^L - \rho^{L-1})\theta(q_2 - kh_L)\right)u_i =$$

$$\frac{\partial}{\partial q_j}\left[-\left(c_{ijkl}^1 + \sum_{L=1}^{N}(c_{ijkl}^L - c_{ijkl}^{L-1})\theta(q_2 - kh_l)\right)\frac{\partial u_k}{\partial q_l}\right.$$

$$\left.-\left(e_{lij}^1 + \sum_{L=1}^{N}(e_{lij}^L - e_{lij}^{L-1})\theta(q_2 - kh_l)\right)\frac{\partial \phi}{\partial q_l}\right] \qquad \text{-(2.17)}$$

$$\frac{\partial}{\partial q_j}\left[\left(e_{jkl}^1 + \sum_{L=1}^{N}(e_{jkl}^L - e_{jkl}^{L-1})\theta(q_2 - kh_L)\right)\frac{\partial u_k}{\partial q_l} -\right.$$

$$\left.\left(\varepsilon_{jl}^1 + \sum_{L=1}^{N}(\varepsilon_{jl}^L - \varepsilon_{jl}^{L-1})\theta(q_2 - kh_L)\right)\frac{\partial \phi}{\partial q_l}\right] = 0 \qquad \text{-(2.18)}$$

The particle displacement and potential are expressed as expansions in the Laguerre polynomials as follows :

$$u_j = \sum_{m=0}^{\infty} p_m^j \left|m(q_2)\right\rangle \exp(iq_1) \qquad \text{-(2.19)}$$

$$\phi = \sum_{m=0}^{\infty} r_m \left|m(q_2)\right\rangle \exp(iq_1) \qquad \text{-(2.20)}$$

where,
$$\left|m(q_2)\right\rangle = \exp[-(q_2/2)]L_m(q_2)/m!$$

and L_m is the mth Laguerre polynomial. The definition of the Laguerre polynomials is taken from Aizenshtadt[22], the Laguerre polynomials used here are a specific form of the generic $L_n^s(x)$ where in this case s=0 and we write $L_n(x)$. Although these summations involve an infinity of terms, in practice after a finite number the contribution from each new term becomes negligible and a finite sum can be used.

After substitution of Equations (2.19) and (2.20) into the relevant wave equations, the orthonormality of the polynomials is exploited by multiplying by $|n\rangle^*$ and integrating over q_2 from 0 to ∞, with subsequent manipulation of the terms an eigenvalue equation is obtained of the form:

$$\frac{\omega^2}{k^2} p_r^i = \left(\rho^0 I + \sum_{L=1}^{N} \left(\rho^L - \rho^{L-1} \right) a_{rn} \right)^{-1} \times \left(P_{nm}^{ik} - Q_{nm}^i S_{nm}^{-1} R_{nm}^k \right) p_m^k \qquad \text{-(2.21)}$$

where the eigenvalue $\frac{\omega^2}{k^2}$, is the square of the SAW velocity, the indices i and k range over the spatial co-ordinates 1, 2, 3 and m, n, r range from zero to the highest number of polynomial used. The matrices [P], [Q], [R], [S] and [a] are given by;

$$P_{nm}^{ik} = - c_{ijkl}^1 M_{jl} - \sum_{L=1}^{N} (c_{ijkl}^L - c_{ijkl}^{L-1}) H_{jl} \qquad \text{-(2.22)}$$

$$Q_{nm}^i = - e_{lij}^1 M_{jl} - \sum_{L=1}^{N} (e_{lij}^L - e_{lij}^{L-1}) H_{jl} \qquad \text{-(2.23)}$$

$$R_{nm}^k = - e_{jkl}^1 M_{jl} + \sum_{L=1}^{N} (e_{jkl}^L - e_{jkl}^{L-1}) H_{jl} \qquad \text{-(2.24)}$$

$$S_{nm} = - \varepsilon_{jl}^1 M_{jl} - \sum_{L=1}^{N} (\varepsilon_{jl}^L - \varepsilon_{jl}^{L-1}) H_{jl} \qquad \text{-(2.25)}$$

$$a_{nr} = \int_0^{\infty} dq_2 |r\rangle^* \theta (q_2 - kh_L) |n\rangle \qquad \text{-(2.26)}$$

where [M] and [H] contain the overlap functions of differentiated Laguerre polynomials, [H] is effectively the multi-layer equivalent of [M], and they have the following form;

$$M_{jl} = \int_0^{\infty} dq_2 |n\rangle^* \frac{\partial}{\partial q_j} \theta (q_2) \frac{\partial}{\partial q_l} |m\rangle \qquad \text{-(2.27)}$$

$$H_{jl} = \int_0^{\infty} dq_2 |n\rangle^* \frac{\partial}{\partial q_j} \theta (q_2 - kh_L) \frac{\partial}{\partial q_l} |m\rangle \qquad \text{-(2.28)}$$

It was found that 5 terms was sufficient to obtain good convergence of the eigenvalues and

vectors, so in that case the eigen-matrix appearing in Equation (2.21) can be expressed as an 18×18 matrix, and the correct eigenvalues and vectors obtained by observing their convergence as the size of the matrix increases. Once the eigenvectors p_m^j are determined they can be substituted into Equation (2.16) to give the variation with depth of the relative magnitude and phase of the particle displacement components. The coefficients r_m are then found by their relationship to the eigenvectors and can then be substituted into Equation (2.20) to give the solution for the electric potential.

Since closed expressions for the potential and particle displacements are obtained it is a straight forward matter to deduce other interesting observable quantities such as the electric field and strain.

The absolute values for the particle displacement will depend on the resistance to movement provided by the material under investigation. Since resistance will vary with the frequency of the acoustic wave, as for instance stiffness becomes more important than the inertial impedance etc., then ideally we require a method to compare absolute values that is independent of the applied frequency. The usual method employed is to calculate the energy flow per unit area in the direction of propagation of the acoustic wave, by considering the electromagnetic and mechanical contributions to the power density of the acoustic field together with the quasi-static assumption. The energy flow is then given according to Auld as

$$W = \frac{1}{2}\mathrm{Re}\left(\int_0^{\infty} dx \; i\omega\left(u_i^* T_{i1} + \phi D_1^*\right)\right) \qquad \text{-(2.29)}$$

where the u, T, ϕ, and D obtained from the model are inserted into this expression using a sub-routine to calculate the power flow. Note that the energy flow expression of Equation (2.29) is calculated along the acoustic beam width, for normalisation of field quantities it is common to assume a power flow of 1mW/λ for all propagating SAWs.

2.2.2 *Introduction to the program and the method used*

The program is written in Fortran 77 and the main object of the program is to solve the eigenvalue problem that is eventually obtained. The procedure is to firstly, set up the specific transformed material tensor matrices in full index form, calculate the various matrices used in the theory relating to the Laguerre polynomials and the material tensors for each layer, and then invert and combine all appropriate matrices.

Two Nag (Numerical Algorithms Group)[23] library subroutines are used in the program, one inverts 8×8 complex matrices, and the other finds the eigenvalues and eigenvectors of, in this case, 18×18 complex matrices.

After solving the eigenvalue problem and producing the eigenvectors required for the expansion of the appropriate particle displacements and electric potential, the corresponding expansion terms for the relevant strains and electric fields are calculated. Finally, the power flow in the direction of propagation of the acoustic wave is calculated for use in normalisation of the field quantities.

A schematic flow chart for the operation of the program is shown in Figure 2.4, it is presented as a rough summary of the major operations of the program.

Figure 2.5 shows the general structure used for the analysis, in the case of $GaAs/Al_xGa_{1-x}As$ multi-layered structures and quantum wells, the substrate would be GaAs. For InGaAs/InP structures the layers are assumed to be lattice matched with a corresponding Indium fraction of 0.53, which corresponds to a structure of negligible mismatch strain[24].

Considering quantum well (QW) structures, they have typical well layer dimensions of around 10Å-150Å, and typical barrier layer dimensions of 100Å-1000Å, device operating SAW frequencies are of the order of 0.5-1.5 GHz. Assuming a surface velocity of $\approx 3\times10^3 ms^{-1}$ for $GaAs/Al_xGa_{1-x}As$ structures, then layer dimensions would lie in the range 0.002 to 0.1 acoustic wavelengths (λ_{ac}), with an operating wavelength lying in the range 2-6μm. In order to gain some qualitative understanding of how the presence of a particular

layer will affect the variation of particle displacement and electric potential with depth, a systematic approach to the analysis of different layer structures was adopted. A bulk GaAs structure was first studied, and the parameters obtained from the program were, the surface wave velocity V_s, and the variation with depth of the particle displacements u_1 and u_2, electric potential ϕ, the strain components S_{11}, S_{22}, S_{12}, S_{21} and the E_1 and E_2 electric field components. A bulk $Al_xGa_{1-x}As$ structure was then studied and the variation of field quantities with aluminium fraction was calculated.

The effect of placing a single layer of $Al_{0.25}Ga_{0.75}As$ on top of the GaAs substrate was then studied. It was thought that layers of about one λ_{ac} below the surface would not have a significant effect on the field profiles, and so layer thicknesses of the order of 0.5 λ_{ac} were initially studied. The layer thickness was then reduced until typical QW dimensions were obtained.

After studying the heterojunction structures, the number of layers was increased, and a full investigation of the variation of field profiles with layer thicknesses was undertaken. As the layer thicknesses decreased, QW dimensions were reached and structures which contained a single quantum well, five, ten and twenty quantum wells were studied.

Parameters	GaAs	AlAs	InAs	InP	Si	Ge
Density (kgm^{-3}) ρ	5360	3760	5667	4810	2330	5323
Stiffness (Nm^{-2})$\times 10^{10}$						
c_{11}	11.88	12.02	8.33	10.22	16.56	12.85
c_{12}	5.38	5.70	4.53	5.76	6.39	4.923
c_{44}	5.94	5.89	3.96	4.60	7.95	6.68
Electric permittivity						
$\varepsilon^s_{11}/\varepsilon_0$	13.18	10.06	15.15	12.61	11.9	17.64
Piezoelectric constant (Cm^{-2})						
e_{14}	-0.154	-0.225	-0.045	-0.035	-	-

Table 2.1 Physical constants used for the modelling. ε_o=8.85410$\times^{-11}$ Fm^{-1}

Physical constants for the materials were taken from Adachi[25], Landolt-Börnstein[26] and INSPEC[24,27] publications and are shown in Table 2.1. In the case of the ternary alloy materials such as $Al_xGa_{1-x}As$ and $In_xGa_{1-x}As$, linear interpolation between the two constituent materials was used to obtain the physical properties. In addition to the AlGaAs/GaAs structures, some results for InGaAs/InP and SiGe/Si structures are also presented.

2.2.3 Results and discussions

For the given propagation direction on III-V structures, the u_1 and u_2 particle displacements were obtained (the u_3 particle displacement was always zero) together with the electric potential, and the associated electric field and strain components were calculated from the gradients of these quantities with respect to the x_1 and x_2 axes. The generalised form of the particle displacements and electric potential can then be written as (ignoring the time dependence);

$$u_i = \sum_{m=0}^{5} p_m^j \exp[-(q_2/2)] L_m(q_2) \exp(iq_1) \qquad \text{-(2.30)}$$

$$\phi = \sum_{m=0}^{5} r_m \exp[-(q_2/2)] L_m(q_2) \exp(iq_1) \qquad \text{-(2.31)}$$

where the expansion coefficients p and r were found through the operation of the program. Since the electric field and strains are constructed from the gradients of these quantities with respect to the Cartesian axes, and are given by

$$S_{ij} = \frac{1}{2}\left(\frac{\partial u_i}{\partial x_j} + \frac{\partial u_j}{\partial x_i}\right) \qquad \text{-(2.32)}$$

$$E_i = -\frac{\partial \phi}{\partial x_i} \qquad \text{-(2.33)}$$

it can be seen immediately that the E_1 component will behave just as the potential variation with depth, and the S_{11} and S_{22} strain components will behave just as the u_1 and u_2 particle displacements respectively.

2.2.3.1 AlGaAs/GaAs structures

The SAW induced field quantities for [110] propagation on bulk GaAs are shown in Figures 2.6-2.9 It can be seen in all graphs that the majority of the SAW induced fields are contained within 1 acoustic wavelength (λ_{ac}) of the surface as is characteristic of surface acoustic waves. It was found that particle displacement profiles of III-V materials have a general form and the profiles for GaAs are shown in Figure 2.6. Only particle displacements with components in the x_1 and x_2 directions can couple to the electric field for this particular propagation direction, i.e. only movement in the plane containing the momentum vector of the acoustic wave and normal to the surface (i.e. in the "sagittal" plane) can be excited piezoelectrically. The two components of the particle displacement are found to have a phase difference of $\pi/2$ radians.

The particle displacements have strains associated with them with respect to the x_1 and x_2 directions, the variation of the amplitudes of these strains with depth are shown in Figure 2.7. The two tensile strain components, s_{11} and s_{22}, are out of phase by $\pi/2$ radians, which results in the general form of the shear strains (s_{12} and s_{21}) being a complex quantity, with the modulus of these quantities being plotted in Figure 2.7.

The variation of the induced electric potential is shown in Figure 2.8. In it's full form the potential is a travelling wave with an oscillatory nature in the x_1 direction and the decaying amplitude of Figure 2.8 in the x_2 direction, therefore the electric field produced as a result of this potential will have two components, one in the direction of propagation and the other normal to the surface. The amplitudes of these components are plotted in Figure 2.9. The E_2 component has an amplitude that follows the shape of the potential curve since differentiating the potential solution with respect to the x_2 direction will leave it's amplitude unchanged. In the same way the E_1 component has an amplitude that is given by the gradient of the curve in Figure 2.8.

The surface velocities obtained for the bulk structures of GaAs and AlGaAs agree well with published values[25]. The variation of surface velocity with Aluminium fraction is shown in

Figure 2.10. The surface velocity of all $Al_xGa_{1-x}As$/GaAs structures ranged between the two extremes of AlAs and GaAs. The general nature of this graph is to be expected since the density of the AlGaAs alloy decreases with increasing Aluminium content, with a less significant increase in stiffness for two of the independent stiffness components (see Table 2.1).

The particle displacement profiles for bulk $Al_xGa_{1-x}As$ show no significant dependence with x, which reflects the relative similarity of the stiffness constants of GaAs, $Al_xGa_{1-x}As$ and AlAs as shown by the values given in Table 2.1. Some authors have reported on the variation in particle displacement with Al fraction[28] and have shown a slight increase in penetration depth with increasing Al fraction. Considering the size of this reported variation, it is not thought to be significant to device operation. Variation of the Aluminium fraction for bulk $Al_xGa_{1-x}As$ significantly affects the potential profiles as shown in Figure 2.11, the piezoelectric constants here range from -0.154 for GaAs to -0.225 for AlAs. All curves have the same general shape and show that the highest potential occurs at the sample surface, while a maximum also occurs at a depth of ~0.35 λ_{ac}. It can be seen that there are also variations in the induced electric field, as given by the shape of the potential graphs for the E_1 components and shown in Figure 2.12 for the E_2 components where the graph has been plotted to a depth of 0.1 acoustic wavelengths.

The effect of the $Al_xGa_{1-x}As$ epitaxial layer thickness and Al content (x) in an AlGaAs/GaAs heterostructure on a (100) GaAs substrate on the induced potentials are shown in Figures 2.13-2.14. The depth profile of the induced potential has the same shape as that of the bulk material and is seen to vary between the profiles of the two constituent materials, the epitaxial layer and the substrate. Near the surface the profile resembles that of the $Al_xGa_{1-x}As$ layer while below the surface it becomes the same as that of the GaAs substrate. However, the point at which the behaviour changes from that of the surface to that of the substrate is dependent on the thickness and composition of the top layer. Two important parameters can be used to assess the effect of layer thickness; the value of the induced potential at the surface and the subsequent development of the potential profile below the surface.

The results given in Figure 2.13 show that layers of > 0.5 λ_{ac} are thick enough to induce a potential at the surface equivalent to a bulk material of the same composition as the surface layer, whereas layers of < 0.05 λ_{ac} have little effect on the induced potential at the surface. The development of the profile below the surface demonstrates that the thickness and composition of the surface layer dominates it's properties at the surface while at greater depths it is the properties of the substrate. The point at which the behaviour changes is obviously dependent on the thickness of the top layer as can be seen in Figure 2.13.

The effect of the composition of an 0.25λ_{ac} thick epitaxial layer on the induced potential is shown in Figure 2.14. Where the general effect of the composition of the layer, with a layer of 0.25 wavelength thickness is indicated. The corresponding electric fields show a similar behaviour indicating how the electric field in the substrate layer can be effected by the composition of the layer above or more specifically by the relative piezoelectric constant of the surface layer.

The thickness of quantum well layers are of the order of 50 to 200 Å. Consequently as this value is << λ_{ac} its effect on the induced potential and resultant field are negligible and can be evaluated by replacing the multiple quantum well structure on the GaAs substrate by an AlGaAs layer of "equivalent composition" on a GaAs substrate. This can be illustrated by the structures whose SAW induced potential profiles are plotted in Figure 2.15. Here a structure consisting of twenty two layers alternating between $Al_{0.5}Ga_{0.5}As$ and GaAs, each of 0.05 λ_{ac} thickness, on a GaAs substrate is shown to be equivalent to a bulk structure of $Al_{0.35}Ga_{0.65}As$. The SAW induced potentials for bulk GaAs and $Al_{0.5}Ga_{0.5}As$ are also plotted here to illustrate the two extremes of the multi-layer structure.

Quantum well structures follow a behaviour as expected from the results already given. For single quantum wells of appropriate device dimensions, the presence of the layer has no significant effect on the induced potential and electric field and there is justification in treating the structure as a heterostructure as far as SAW propagation is concerned, with the two barriers forming the top layer of the heterostructure. As the number of quantum wells is increased the effects of the barriers and wells within the active region of the structure, have an increasing part to play on the induced potentials and fields.

For the design of devices using MQW structures it becomes important to consider if the QW region of the device is extending into the regions of much lower potential (0.1λ and below). It is then apparent that variations in the thickness and the aluminium fraction of the barriers that surround the QW region could aid in optimising the electric field within the QW region.

Given an assumed power flow of 1 mW/λ_{ac} the absolute values of electric potentials were calculated to lie in the range 0.6V to 1.5V measured at the surface of the structures, with these two figures indicating the values obtained for bulk GaAs and AlAs respectively. Assuming a SAW wavelength in the range 1-5μm, this corresponds to electric fields in the range $\approx 10^4$-10^5 Vcm^{-1}. The important point with regard to this figure is that devices that utilise applied electric field induced changes in absorption and refractive index in MQW structures typically operate within this range of electric fields[29,30]. Using the same power flow the particle displacements were calculated to be of the order of a few Angstroms and this corresponded to strains of the order of ~0.01%.

2.2.3.2 InGaAs/InP structures

The particle displacements, induced potential and resultant electric field in InGaAs and InP all have the same form as discussed above for GaAs, there is a slight difference between the particle displacements obtained for bulk $In_{0.53}Ga_{0.47}As$ and bulk InP but it is not significant enough to cause a discernible difference in induced strain.

The potential profile results follow the same behaviour as the previous results as is shown in Figure 2.16, however the larger difference in the piezoelectric constants of the two constituent materials is reflected in the graphs, and also in the electric fields obtained from those profiles. Both InAs and InP have much smaller piezoelectric coefficients (by around a factor of 4) than either GaAs or AlGaAs, as shown in Table 2.1. This is reflected in the absolute value of the induced potential.

2.2.3.3 SiGe/Si structures

Both Si and Ge possess a centrosymmetric crystal structure and hence are not piezoelectric. For SAW propagation on the bulk materials only particle displacements and strains are induced by the SAW. The Particle displacements for SAW propagation in the [110] direction and (100) plane of the bulk materials are shown in Figure 2.17. They show a similar shape to that of the III-V structures, with the relative sizes of the SAW induced particle displacements for Si and Ge being similar to within a maximum of ~8% (estimated from graph).

SiGe is a complex binary alloy, and it's properties are not as well documented as familiar III-V alloys. The growth of the alloy on Si substrates can result in both highly strained layers and layers with a large amount of dislocations[31]. As far as the author is aware, it is not known whether disruptions of the crystal structure in this sense could lead to piezoelectric behaviour in SiGe materials. For this reason the SiGe alloy has been treated as non-piezoelectric for this analysis.

2.3 SUMMARY

The variation with depth of particle displacements, potentials, strains and electric fields has been obtained using a Laguerre polynomial technique, for the layered structures of $Al_xGa_{1-x}As$/GaAs, unstrained $In_yGa_{1-y}As$/InP and SiGe/Si. The method is an effective and efficient way of determining the appropriate parameters for SAW propagation on layered structures, since the program is effectively non-iterative, once the initial code writing has been done, it only takes a relatively short amount of time to obtain eigenvectors for given material structures.

The $Al_xGa_{1-x}As$/GaAs system shows distinct differences for the potential profiles, which can be modified using variations of the layer thickness and composition and the number of layers in the structure, thereby enabling the characteristics, such as the induced electric field in the

structure to be optimised. The results presented above also show that the SAW propagation characteristics are determined by the complete structure and not by any single layer.

The $In_{0.53}Ga_{0.47}As/InP$ system shows larger differences in the potential and electric field profiles, and again modification of the electric field with a view to it's optimisation within the MQW region of applicable devices is evident.

Specific device structure and applicability is very important when considering modifications of the electric field through variations of parameters such as the Aluminium content and layer thickness', since the relationship between SAW frequency and device dimensions will be a principal factor in setting the nature of the decay of the induced potential for given material constituents.

It should be noted that the method used here to determine the characteristics of the SAW induced fields leads to a single phase velocity $\omega/\mathbf{k}$, i.e. the method is implicitly dispersionless. Dispersion is expected to arise through coupling of the movement between individual layers in a multi-layer structure and hence any accurate model should ideally include the determination of group velocities, given as $\partial\omega/\partial\mathbf{k}$.

References

[1] Weisbuch, C. and Vinter, B. *Quantum well semiconductor structures*, Academic Press, New York (1991)

[2] Jain, F.C., Bhattacharjee, K.K. and Grudkowski, T.W. "Recent developments in multiple quantum well acousto-optic and electro-optic modulator structures," Proc. IEEE Ultrason. Symp., pp.529-536, (1991)

[3] Gryba, T., Lefebvre, J.E. "Optimisation of MQW structures for acousto-optic absorption modulators," Proc. IEEE Optoelectronics, **141**, (1), pp.62-64, (1994)

[4] Fahmy, A.H. and Adler, E.L. "Propagation of acoustic surface waves in multilayers: a matrix description," Appl. Phys. Lett., **22**, pp.495-497, (1973)

[5] Armenise, M.N., Passaro, V.M.N., and Impagnatiello, F. "Acoustic mode analysis of a homogeneous multilayer guiding structure," J. Opt. Soc. Am. B **8**, pp.443-446 (1991)

[6] Adler, E.L. "Matrix methods applied to acoustic waves in multilayers," IEEE Trans. Ultrasonics, Ferroelectrics and Frequency Control, **37**, pp.485-490, (1991)

[7] Bright, V.M and Hunt, W.D. "Surface acoustic wave properties of aluminium gallium arsenide," J. Appl. Phys., **66**, pp.90-96, (1989)

[8] Bright, V.M., Kim, Y. and Hunt, W.D., "Study of surface acoustic waves on the {110} plane of Gallium Arsenide," J. Appl. Phys. **71**, pp.597-605, (1992)

[9] Bright, V.M. and Hunt, W.D., "Bleustein-Gulyaev waves in gallium arsenide and other piezoelectric cubic crystals," J. Appl. Phys., **66**, pp.1556-1564, (1989)

[10] Webster, R.T. and Carr, P.H., "Rayleigh waves on Gallium Arsenide" Proc. Int. Symp. *Rayleigh wave theory and applications*, 15-17 July, London, England pp.122-130, (1985)

[11] Bright, V.M., Kim, Y. and Hunt, W.D. "An analysis of surface acoustic waves in a piezoelectric film over a GaAs/AlGaAs heterostructure," J. Appl. Phys., **71**, pp.2136-2142, (1992)

[12] Kikkarin, S.M., Petrov, D.V. and Takovkin, I.B., "Surface acoustic waves in GaAlAs/Ga structures," Sov. Phys. Acoust., **33**, pp76-78, (1987)

[13] Sharon, T.M. "Edge modes for piezoelectric wedges of arbitrary interior angles," Proc. IEEE Ultrason. Symp., pp.126-130 (1973)

[14] Datta, S. and Hunsinger, B.J. "Analysis of surface waves using orthogonal functions," J Appl. Phys., **49**, pp.475-479, (1978)

[15] Kim,Y. and Hunt,W.D. "Acoustic fields and velocities for surface-acoustic-wave propagation in multilayered structures: an extension of the Laguerre polynomial approach," J. App. Phys. **68**, pp.4993-4997, (1990)

[16] Thompson, C. and Weiss, B.L. "Characteristics of surface acoustic wave propagation in III-V semiconductor quantum well structures," J. Appl. Phys., **78**, (8), pp.1-6, (1995)

[17] Bleustein, J.L. "A new surface wave in piezoelectric materials," Appl. Phys. Lett., **13**, pp.412-413, (1968)

[18] Velasco, V.R. "Surface and interface Bleustein-Gulyaev waves along symmetry directions of cubic crystals," Surf. Sci., **139**, pp.63-74, (1984)

[19] Schiff, L.I. *QUANTUM MECHANICS*, page 92, Third edition, McGraw-Hill, (1968)

[20] Auld, B.A. *Acoustic fields and waves in solids* Vol 1. Wiley, New York (1973)

[21] Butkov, E., *Mathematical physics*, Chapter 16, Addison-Wesley, (1968)

[22] Aizenshtadt, V.S. and Krylov, V.I. *Tables of Laguerre polynomials and functions* Pergamon, New York (1966)

[23] *The NAG Fortran library manual*, Mark 16, NAG Ltd, (1993).

[24] *Properties of lattice matched and strained Indium Gallium Arsenide*, Ed. P.Bhattacharya, INSPEC Datareview series

[25] Adachi, S. "GaAs, AlAs, and AlGaAs: Material parameters for use in research and device applications," J. Appl. Phys., **58**, pp.R1-R29, (1985)

[26] Landolt-Börnstein, *Numerical Data and Functional Relationships in Science and Technology*, Group III, Volume 17a, *Semiconductors: Physics of Group IV elements and III-V compounds*, Ed. O.Madelung, Springer-Verlag, Berlin, (1982)

[27] *Properties of strained and relaxed Silicon Germanium*, Ed. E.Kasper, EMIS Datareview series No.12, IEE, INSPEC (1995)

[28] Armenise, M.N., Matteo, A.M. and Passaro, V.M.N. "Analysis of acoustic planar wavegudies," Proc. SPIE Vol. 1583, *Integrated Optical circuits*, pp.256-267 (1991)

[29] Wood, T.H. "Multiple Quantum Well (MQW) Waveguide Modulators," J. Lightwave Technol., **6**, pp.743-757, (1988)

[30] Kan, Y., Nagai, H., Masamichi, Y. and Suemune, I. "Field Effects on the Refractive Index and Absorption Coefficient in AlGaAs Quantum Well Structures and Their Feasibility for Electrooptic Device Applications," IEEE J. Quantum Electron., **QE-23**, pp.2167-2179, (1987)

[31] Arienzo, M. Iyer, S.S. Meyerson, B.S. Patton, G.L. and Stork, J.M.C. "Si-Ge alloys: Growth, properties and applications," Appl. Surface Sci., **48/49**, pp.377-386, (1991)

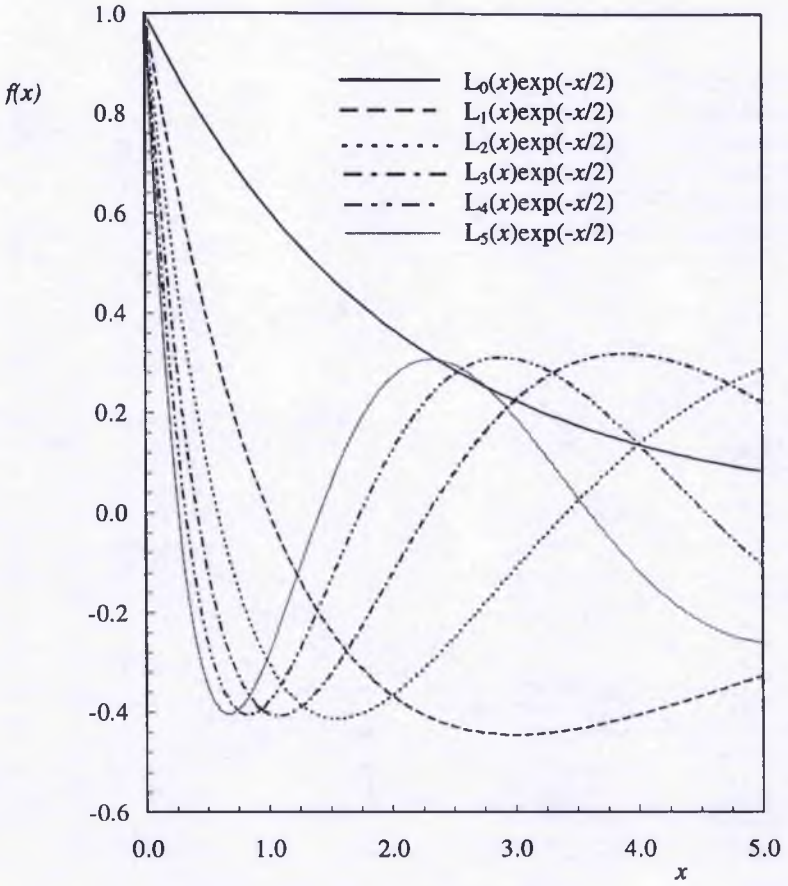

Figure 2.1. *First five Laguerre polynomial functions ($L_i(x)$) multiplied by exp(-x/2).*

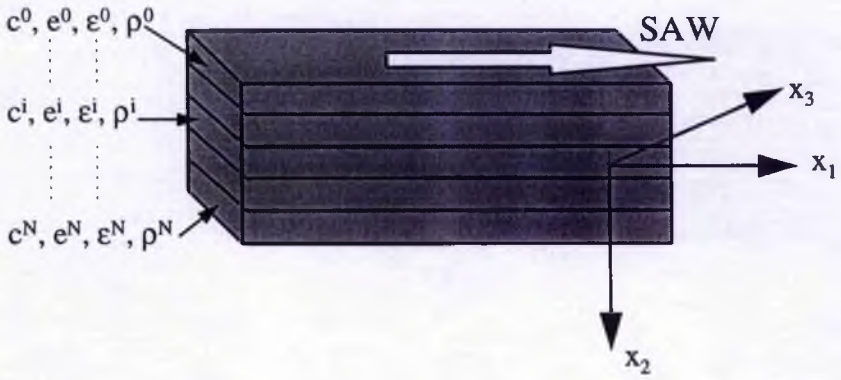

Figure 2.2 *Schematic diagram of the generic material structure and the coordinate system adopted. Each layer is characterised by it's stiffness and piezoelectric constants and by it's density and permittivity. E.g. c^0 is the stiffness in the first layer, c^N is the stiffness in the final layer*

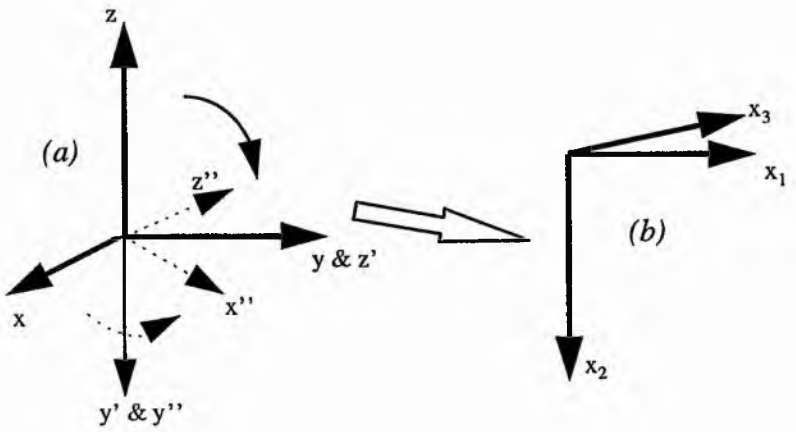

Figure 2.3 *Illustration of the transformation of the crystallographic coordinate system (a) into the coordinate system adopted for the SAW analysis (b). The SAW propagates in the [110] direction on the (100) plane.*

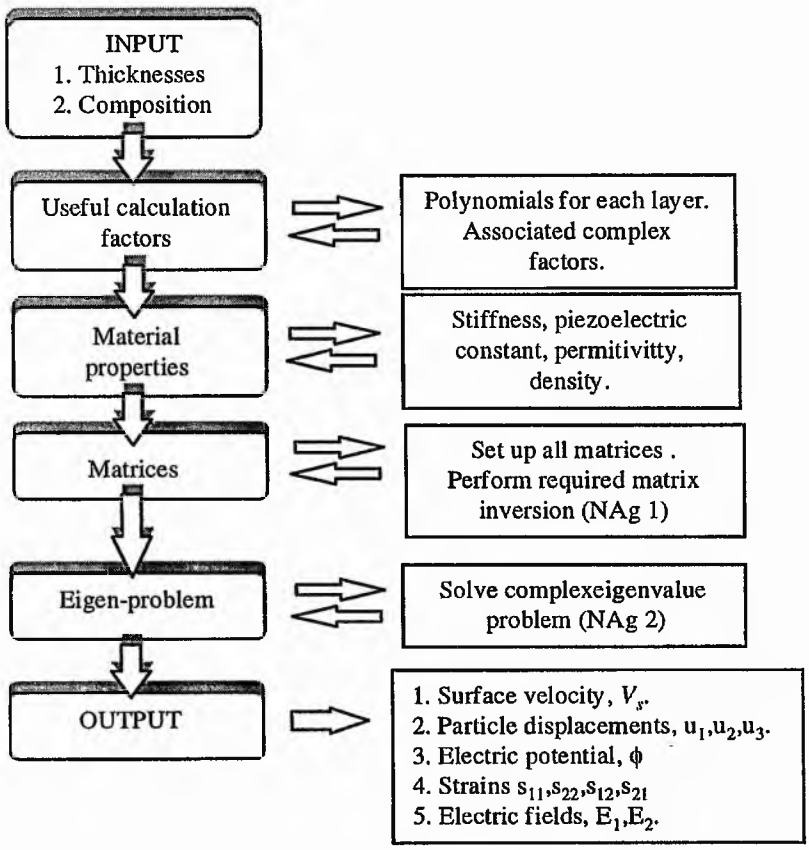

Figure 2.4 *Flow chart representation of the major operations of the program, including two major sub-routines, NAg1 and NAg2.*

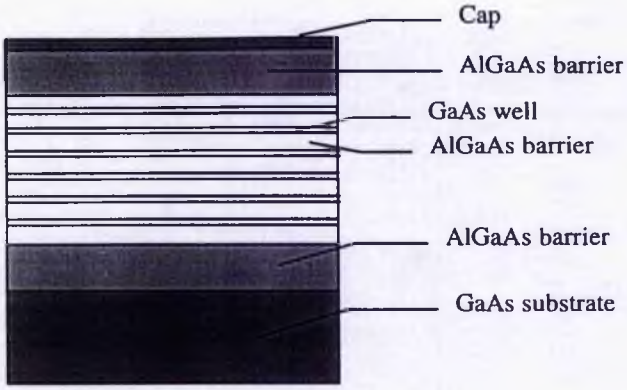

***Figure 2.5** Schematic diagram showing the general structure assumed for the analysis, here for example for an AlGaAs/GaAs structure*

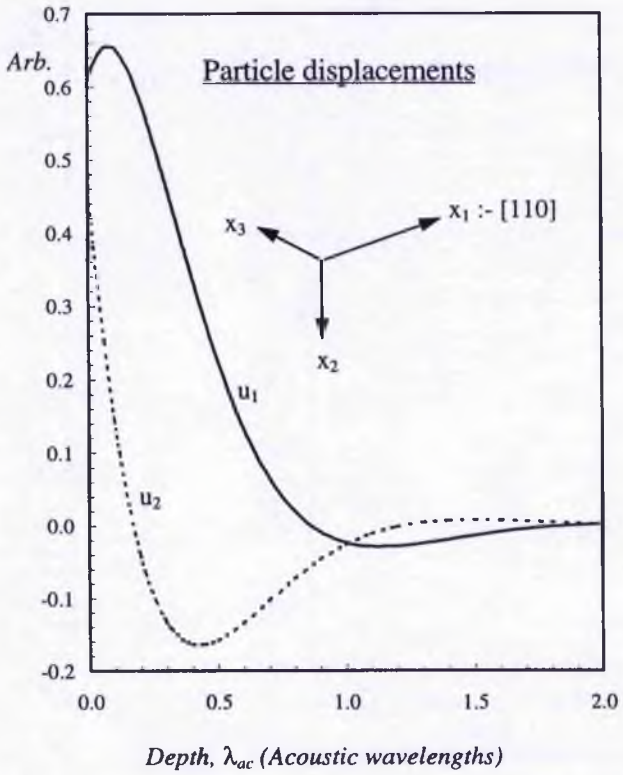

***Figure 2.6** Variation of particle displacements u_1 and u_2 with depth for [110] SAW propagation on {100} bulk GaAs*

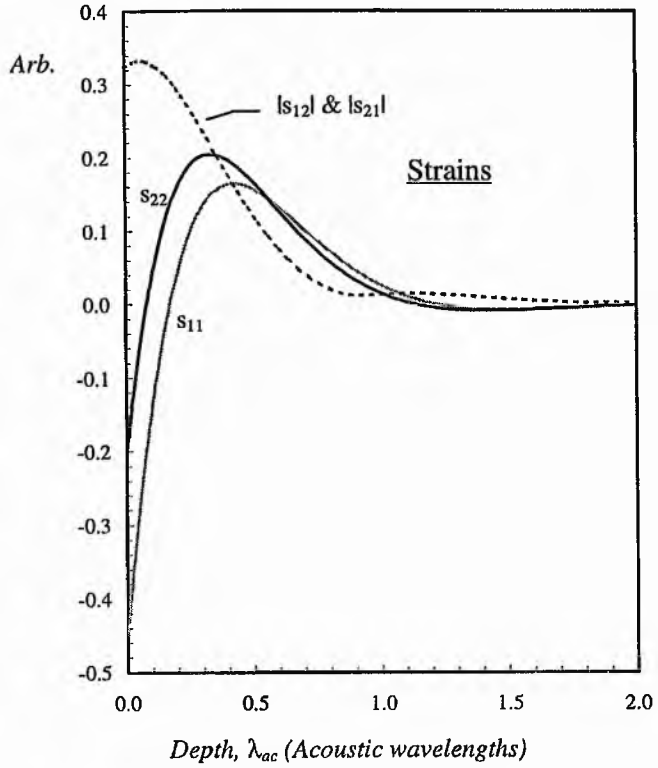

Figure 2.7 *Variation of SAW induced strain components with depth for [110] SAW propagation on bulk GaAs. The shear strains s_{12} and s_{21} are complex numbers whose moduli are equal and is plotted here.*

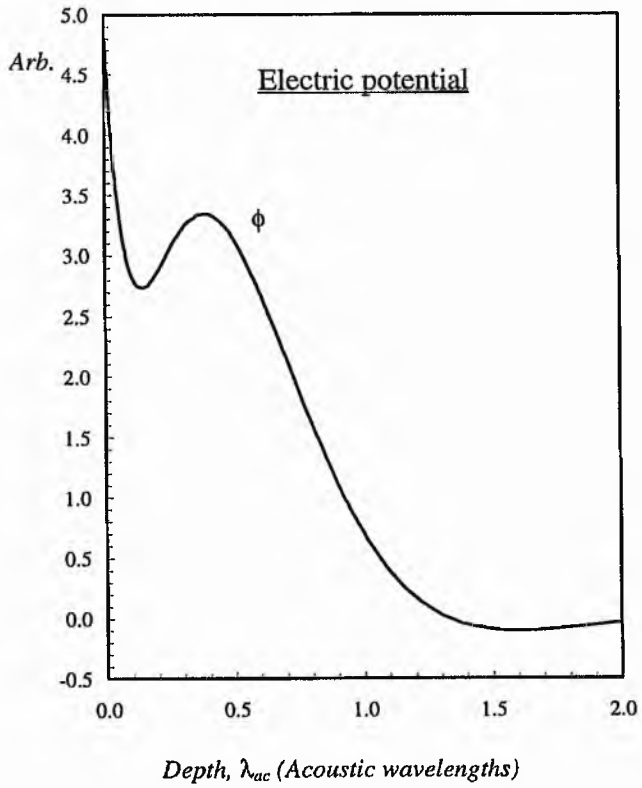

Figure 2.8 *Variation of SAW induced electric potential with depth for [110] SAW propagation on {100} bulk GaAs*

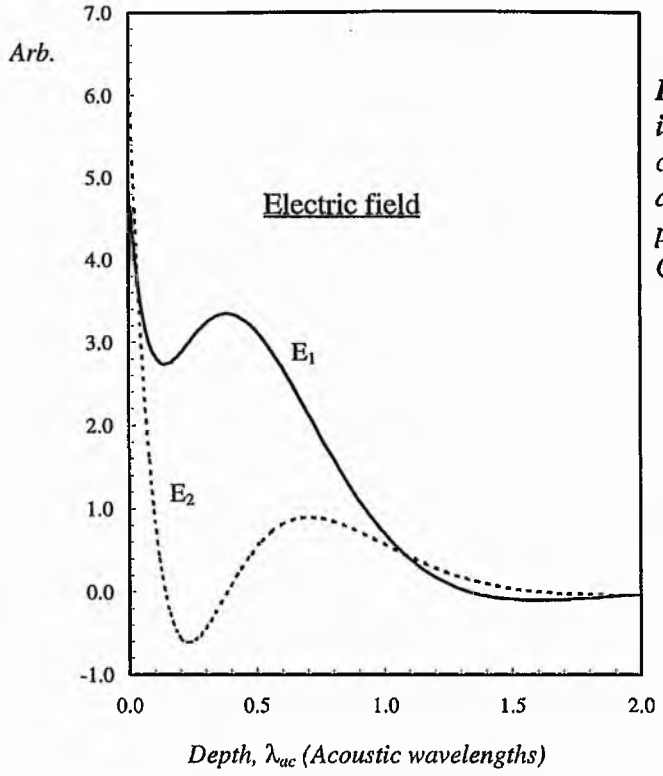

Figure 2.9 *Variation of SAW induced electric field components E_1 and E_2 with depth for [110] SAW propagation on {100} bulk GaAs*

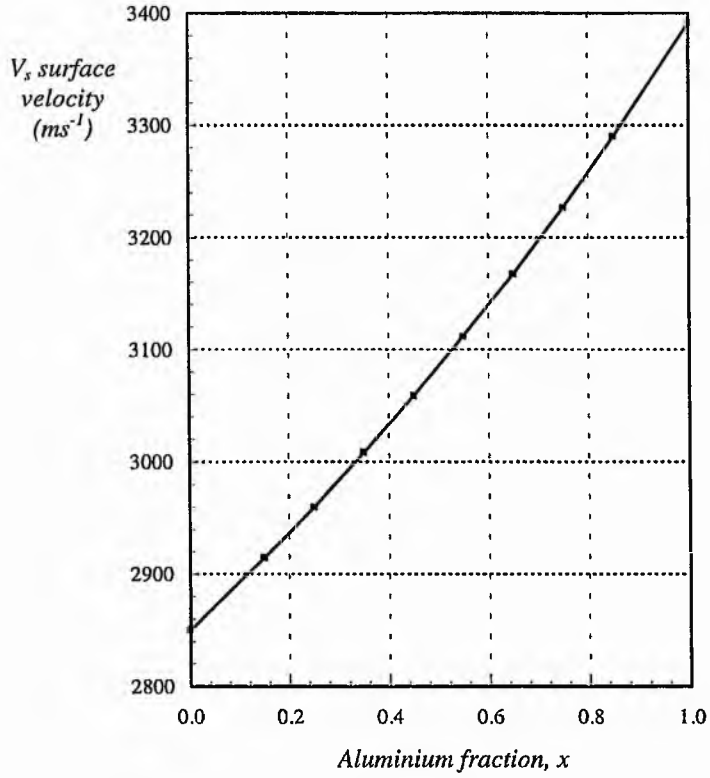

Figure 2.10 *Variation of surface velocity with Aluminium fraction for [110] propagation on {100} bulk $Al_xGa_{1-x}As$*

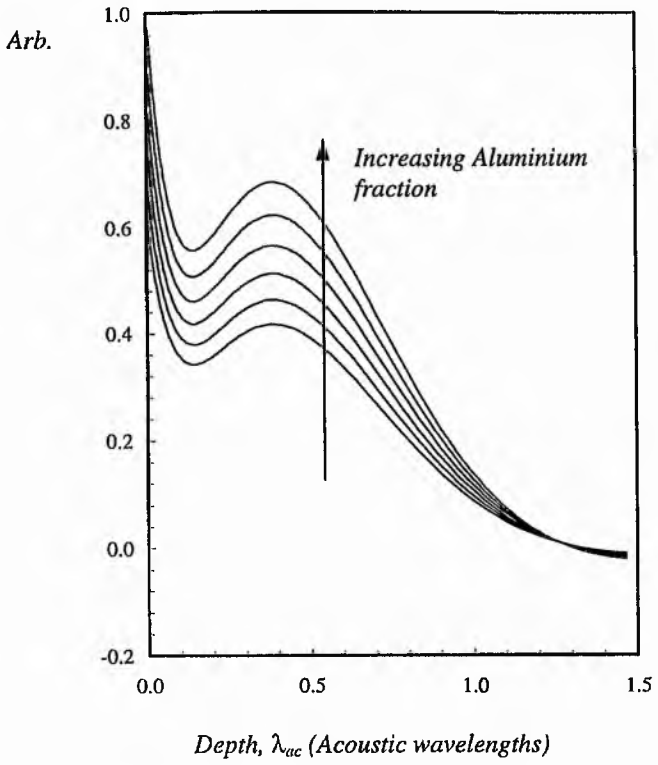

Figure 2.11 *Variation of SAW induced electric potential with depth for [110] SAW propagation on {100} bulk $Al_xGa_{1-x}As$ for a range of Aluminium fractions x=0.0, 0.2, 0.4, 0.6, 0.8, 1.0*

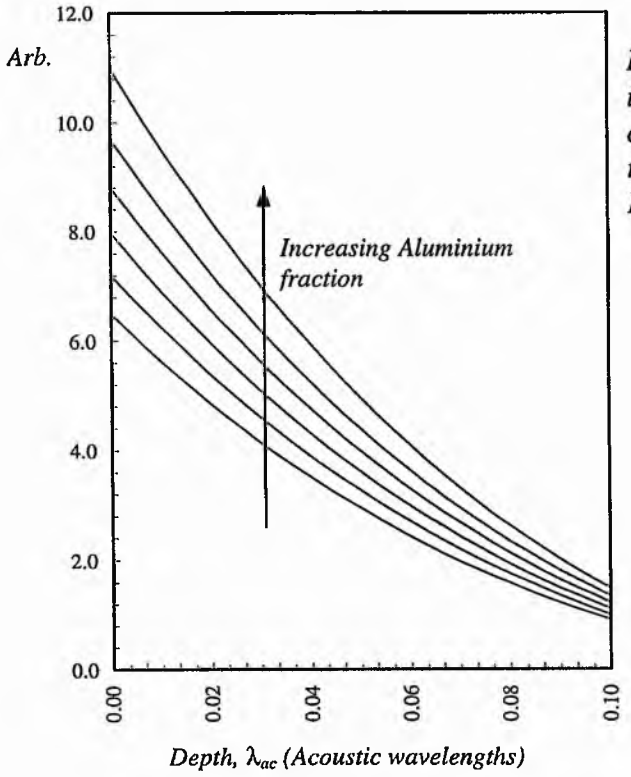

Figure 2.12 *Variation of SAW induced electric field component E_2 corresponding to the electric potentials of Figure 2.11*

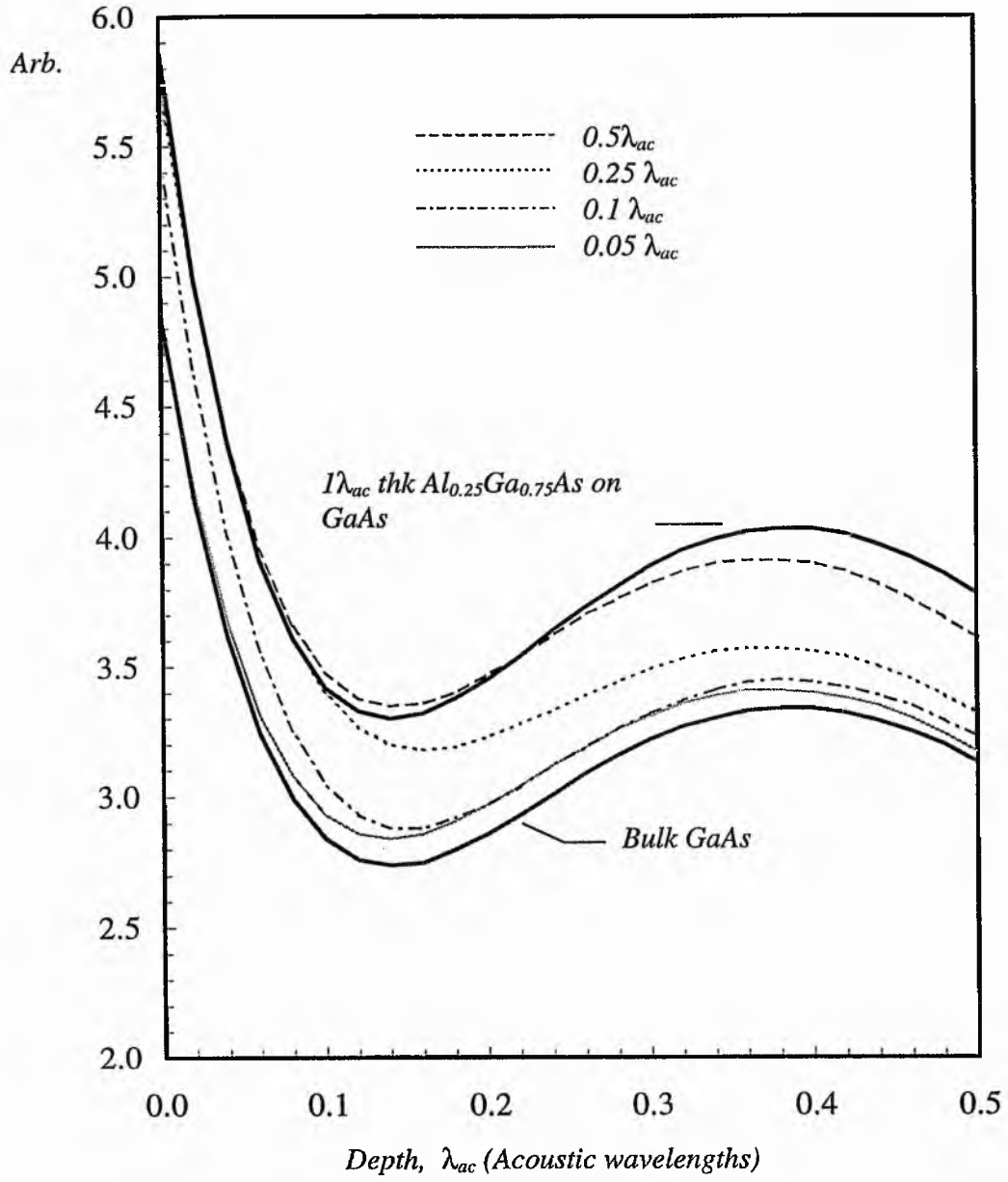

Figure 2.13 *Variation with depth of SAW induced potentials, for heterostructure of $Al_{0.25}Ga_{0.75}As$ layer on GaAs substrate for layer thicknesses in the range 0.05 to $1\lambda_{ac}$*

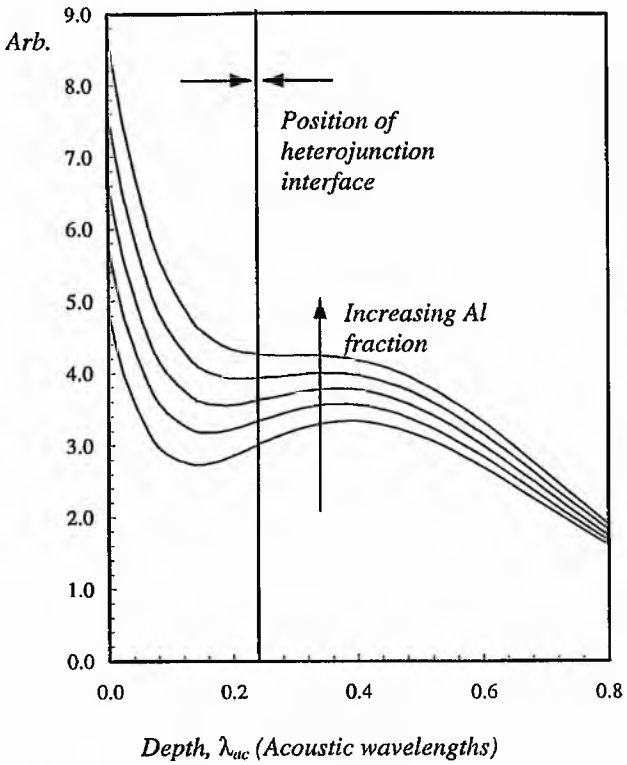

Figure 2.14 *Variation with depth of SAW induced potentials for heterostructure of 1/4 λ_{ac} thickness AlGaAs layer on GaAs substrate for aluminium fractions of x=0.0 , 0.25, 0.5, 0.75,1.0*

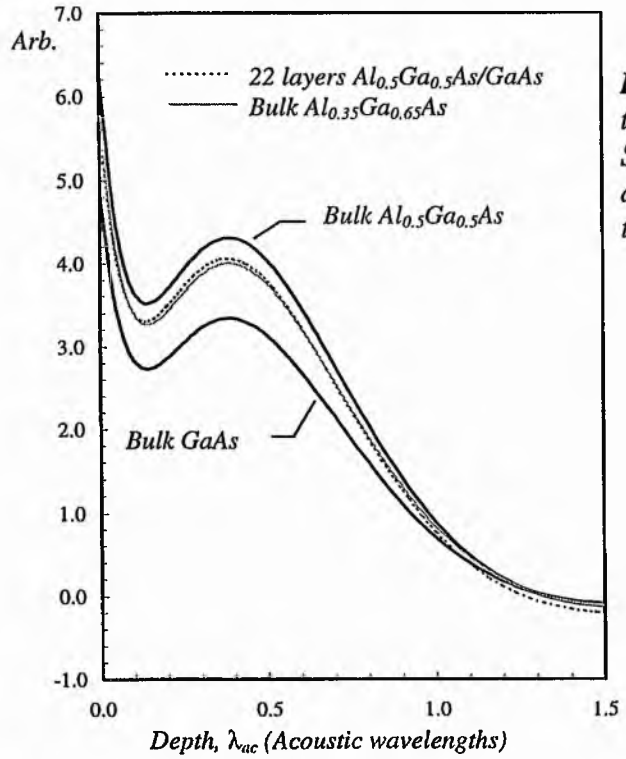

Figure 2.15 *Example of the equivalence of the SAW induced potential for a multi-layer structure to that of a bulk material*

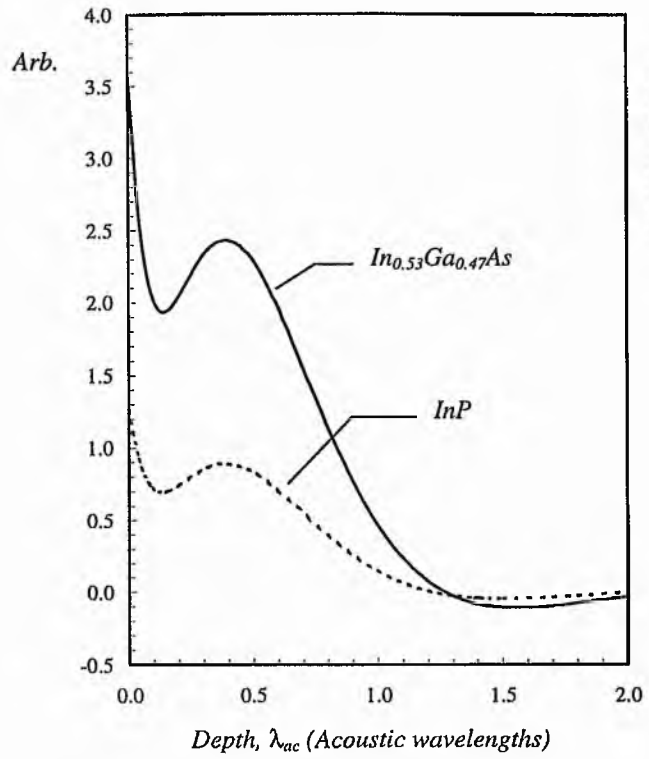

Figure 2.16 *SAW induced potential profiles for [110] propagation on bulk {100} InP and* $In_{0.53}Ga_{0.47}As$

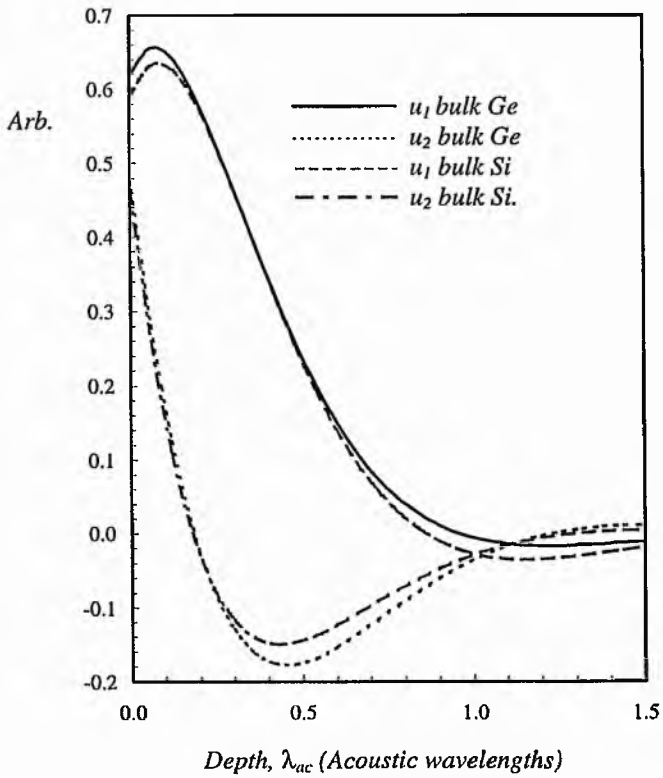

Figure 2.17 *SAW induced particle displacements,* u_1 *and* u_2 *for [110] propagation on bulk {100} Ge and Si.*

Chapter 3

The Modal Properties of Multi-Layer and Multiple Quantum Well III-V Planar Waveguides

3.1 INTRODUCTION

The refractive index of the ternary alloy $Al_xGa_{1-x}As$ depends on the value of the Aluminium fraction[1] x, so that different MQW structures will have different transverse refractive index profiles. It is therefore sensible to expect that variations in the structure of an AlGaAs/GaAs multi-layer waveguide will also affect the optical modes supported by that structure. This chapter is concerned with the determination of the guided optical modes of a generic multi-layer planar waveguide and the effect on those modes of variations in material structure. In chapter 2 it was shown that an arbitrary multi-layer AlGaAs/GaAs structure can affect the fields induced by the propagation of a surface acoustic wave, through variations in layer composition from layer to layer.

The acousto-optic diffraction efficiency of SAWs and guided optical modes is critically dependent on the overlap between the optical mode profiles and the SAW induced fields[2]. Therefore it is of interest to see whether compositionally induced variations in the guided optical mode profiles appropriate to improving acousto-optic overlaps can be brought about. In other words, does a multi-layer structure have any inherent advantage over a single layer structure (irrespective of any quantum effects), for acousto-optic applications ?

Multi-layer optical waveguide structures, including multiple quantum well (MQW) waveguides, are interesting as they form the basis of a number of optical and optoelectronic devices, including semiconductor laser cavities[3] and modulators[4]. The characteristics of these multi-layer waveguides influence the properties of the devices and are determined by the optical properties, i.e. absorption coefficient and refractive index profile of the structure, which are determined by the composition and thickness of each layer. Therefore by tailoring both the properties of these layers and the envelope of the transverse refractive index profile of a multi-layer optical waveguide, the characteristics of the waveguide may be tailored to specific requirements. Accurate control of layer composition and thickness can be achieved using molecular beam epitaxy (MBE) and metal organic chemical vapor deposition (MOCVD) for the growth of multi-layer structures, so that multi-layer waveguides with the required characteristics may be realised.

The propagation characteristics of multi-layer and MQW waveguides have been studied using both matrix methods[5] and finite element methods[6]. Each of these techniques produce the propagation constant and transverse field profiles of each propagating mode. Finite element techniques provide a framework for accurate determination of guided modes in both linear and non-linear optical waveguide structures and materials, while other methods have a simpler mathematical formulation and can be much less computationally intensive. Formulae for representing the refractive index profile of a MQW waveguide by a single "equivalent" index for both TE and TM modes have been developed[7,8], and justified using perturbation theory[9].

To date, the QW waveguide structures studied have been limited to those with identical well and barrier layer thicknesses and compositions [10,11,12]. However, it has been shown previously that varying the layer parameters of the MQW core can produce interesting waveguide characteristics such as single mode and single polarization waveguides[11]. In addition, the refractive index of the substrate, which is normally the lower waveguide cladding layer, has a significant effect on the waveguide characteristics. However, variation of the thickness and composition of each layer in the structure has not been fully investigated and provides another variable which may be used to tune the waveguide characteristics to those required for specific applications.

The results of a study of the modal characteristics of graded-step index multi-layer and QW waveguides are presented here. Results of the mode field profile and propagation constant are presented here for linearly graded waveguides and several characteristics are identified which may be useful for the development of waveguide devices. The results presented below indicate what effects are possible although for "real" QW structures quantum mechanical effects have to be taken into consideration[13] and are beyond the scope of the work presented here.

3.2 THEORY

The characteristics of multi-layer waveguides are determined by the solution of the wave equations derived from Maxwell's equations, using the matching of the fields and their gradients at the layer interfaces as the boundary conditions. The approach is a simple extension of the standard technique for three layer planar waveguides that is outlined in many texts[14].

The basic multi-layer waveguide structure is shown schematically in Figure 3.1, together with the different types of refractive index profiles that were studied and the coordinate system adopted. The core region consists of a sequence of pairs of low (AlGaAs) and high (GaAs) refractive index material sandwiched between upper and lower cladding regions, the upper cladding layer is always air or compositionally equivalent to the lower cladding layer. The former case is a symmetrical structure and the latter is an asymmetrical structure. In the case of QW structures the high and low index layers comprising the core are well and barrier layers respectively. The model allows for any combination of layer thicknesses and refractive indices, and the distribution of the refractive indices is limited only by the constraints imposed by the range of materials available in the particular material system and the assumed form of the field profiles as described in section 3.3. For individual layer thicknesses less than ~200Å the refractive index of the layer is determined by both it's composition and layer thickness since quantum mechanical effects modify the allowed energy levels in the structure which result in different absorption spectra and therefore different refractive indices.

3.2.1 TE modes

By taking the vector curl of the appropriate Maxwell equations, wave equations for both the magnetic and electric field vectors can be obtained[15]. For TE plane waves traveling in the z direction, the appropriate wave equation is :

$$\nabla^2 E_y = \frac{n_i^2}{c^2}\frac{\partial^2 E_y}{\partial t^2} \qquad -(3.1)$$

with the subscript i referring to the i'th layer, n_i is the refractive index of the i'th layer, c is the velocity of light in free space and E_y is the transverse electric field in the y direction .

Solutions of this equation in each layer are assumed to be of the plane wave form :

$$E_y(x, z, t) = \varepsilon_y(x)\exp(i\omega t - i\beta z) \qquad -(3.2)$$

where β is the propagation constant, ω is the optical angular frequency and $\varepsilon_y(x)$ is the amplitude of the wave solution which has no y or z dependence because the planar structure is assumed to be infinite in these directions, thereby removing the possibility of reflections and resultant standing waves. If the general form of the solution is substituted into the wave equation, a corresponding second order differential equation involving the amplitude $\varepsilon_y(x)$ is obtained, whose solution is of the form

$$\varepsilon_y(x) = A\exp(\alpha x) + B\exp(-\alpha x) \qquad -(3.3)$$

where,
$$\alpha = \sqrt{\beta^2 - \frac{n_i^2}{c^2}\omega^2}$$

and is either real or imaginary, A and B are complex constants and α is a decay constant for each layer. For guided modes, solutions are sought by forcing $\varepsilon_y(x)$ to be a decaying exponential into both cladding layers. Consequently α is assumed to be real in both cladding layers, imaginary in the high refractive index core layers and is allowed to be either real or imaginary in the low refractive index barrier layers. Referring to the definition of α given with Equation (3.3), the refractive index is the only factor that varies over the structure of the waveguide. Therefore

propagating modes of this kind only exist for values of β determined by the minimum refractive index of the high refractive index layers in the core region and the highest refractive index of the two cladding layers. Hence the following assumptions are used to determine the field profiles in each layer;

$$\varepsilon_y(x) = A_1 \exp(\alpha_1 x) \quad \text{in the substrate.}$$

$$\varepsilon_y(x) = A_j \exp(\alpha_j (x - t_{j-1})) + B_j \exp(-\alpha_j (x - t_{j-1}))$$

or $$\varepsilon_y(x) = A_j \exp(i\alpha_j (x - t_{j-1})) + B_j \exp(-i\alpha_j (x - t_{j-1})) \quad \text{in the } j^{th} \text{ barrier}$$

and

$$\varepsilon_y(x) = A_i \exp(i\alpha_i (x - t_{i-1})) + B_i \exp(-i\alpha_i (x - t_{i-1})) \quad \text{in the } i^{th} \text{ well}$$

$$\varepsilon_y(x) = A_N \exp(\alpha_N (x - t_{N-1})) \quad \text{in the top layer (air)}$$

-(3.4)

where the appropriate definition of α is used in each case, N is the total number of layers and t labels the cumulative depth of a particular layer. The boundary conditions require that $\varepsilon_y(x)$ and it's first derivative be continuous at each interface, which leads to field matching at each interface. The A and B coefficients for each layer can then be expressed recursively in terms of the values in the previous layer. Matching the fields and their gradients at the final interface gives :

$$-\alpha_N (A_{N-1} \exp(\alpha_{N-1}(t_{N-2} - t_{N-1})) + B_{N-1} \exp(-\alpha_{N-1}(t_{N-2} - t_{N-1}))) =$$
$$\alpha_{N-1} (A_{N-1} \exp(\alpha_{N-1}(t_{N-2} - t_{N-1})) - B_{N-1} \exp(-\alpha_{N-1}(t_{N-2} - t_{N-1})))$$

-(3.5)

which depends on the α and the A and B coefficients for each layer in the structure. Assuming a constant value for A_1 from which all other amplitudes can de derived, Equation (3.5) becomes

$$f(\beta) = 0 \qquad \text{-(3.6)}$$

Values of β which satisfy Equation (3.6) produce all other parameters of a guided mode. Equation (3.6) was solved, within the allowed range of β which was set by the composition of the

waveguide structure, using a pair of numerical routines[16] that bracketed the roots and then iteratively bisected the bracketed ranges, to improve the accuracy of the solutions.

3.2.2 TM modes

The development of the theory for the TM modes exactly parallels that for the TE modes, except that the non-zero field components are now H_y, E_x and E_z rather than E_y, H_x and H_z for the TE case. Assuming a plane wave form for the H_y component as in the TE case, the vector curl of the magnetic field components is used to determine the magnetic field components and is equal to the time derivative of the *electric displacement*, $\boldsymbol{D}$ (in the absence of any current sources) and not the electric field. This is from the two inhomogeneous Maxwell equations[17], in the absence of current sources and charge density,

$$\nabla \times \boldsymbol{E} = -\dot{\boldsymbol{B}} \qquad \text{-(3.7)}$$

$$\nabla \times \boldsymbol{H} = -\dot{\boldsymbol{D}} \qquad \text{-(3.8)}$$

where $\boldsymbol{E}$, $\boldsymbol{H}$ are the electric and magnetic field strengths, $\boldsymbol{D}$ is the electric displacement and $\boldsymbol{B}$ is the magnetic flux density. The consequence of this electric displacement dependence is the introduction of the refractive index (via the electric permitivitty) into the field components and hence the boundary conditions. Then, when matching field gradients at layer interfaces, the refractive indices of individual layers must also be included . This leads to further factors in the recursive relationship mentioned in context with Equation (3.5). The problem is then solved in exactly the same way as for the TE case.

3.2.3 Power flow normalisation

The constant A_1 appearing in Equation (3.4) (from which all other amplitudes are derived) together with an equivalent constant for the TM case are arbitrary and can be set by the power flow of the optical mode. It is chosen here so that the optical mode has 1 W of power flow per unit width in the y direction. The normalisation condition for the TE and TM modes is then given by

$$-\frac{1}{2}\int_{-\infty}^{+\infty} E_y H_x^{*}\,dx = \frac{\beta_m}{2\omega\mu}\int_{-\infty}^{+\infty}\left[\varepsilon_y^{(m)}(x)\right]^2 dx = 1 \qquad \text{-(3.9)}$$

$$-\frac{1}{2}\int_{-\infty}^{+\infty} H_y E_x^{*}\,dx = \frac{\beta_m}{2\omega}\int_{-\infty}^{+\infty}\left[\mathscr{H}_y^{(m)}(x)/n(x)\right]^2 dx = 1 \qquad \text{-(3.10)}$$

where Equation (3.9) corresponds to the TE case and (3.10) to the TM case and both expressions have been derived from the standard form of the Poynting vector. m corresponds to the m'th confined mode, $n(x)$ is the refractive index profile across the waveguide and in this case is a piecewise continous function. $\mathscr{H}_y(x)$ is the amplitude of the transverse magnetic field component. Considering the TE modes, the assumed form of the fields in each layer (Equations (3.4)) can be substituted into a modified version of Equation (3.9) involving a summation of integrals over individual layers, to give a more specific form to the normalisation condition from which the constant A_l can be determined and the form of the optical modes can then be plotted. An equivalent process for the TM modes can then also be performed.

3.3 WAVEGUIDE STRUCTURE

A schematic view of the waveguide structures modelled here is shown in Figure 3.1 together with the various waveguide transverse refractive index profiles studied here. The waveguide core consists of a sequence of pairs of layers and each pair consists of a low index and a high index layer, which will be referred to below as the barrier and well layer respectively. The core is bounded below by an $Al_xGa_{1-x}As$ cladding layer and above by either air or an $Al_xGa_{1-x}As$ cladding layer which produce either asymmetric or symmetric waveguide structures respectively. In the core region of these waveguide structures, all of the well layers are GaAs and all of the barrier layers are $Al_xGa_{1-x}As$, unless otherwise stated the upper cladding layer is assumed to be air.

In the structures studied here the refractive index of the barrier layers is varied between the two cladding layers, unlike all previous publications concerned with such multi-layer waveguide

structures, where all of the high and low index layers in the core are kept constant. The generic multi-layer waveguide structure, which has identical high and low refractive index layers in the core, has been extensively studied [10-12] and it's refractive index profile is shown in Figure 3.1(b). n_b is the refractive index in the barrier layers and n_w is the refractive index in the well layers.

The linearly graded-step refractive index profile contains identical GaAs well layers while the composition, and therefore the refractive index of the AlGaAs barrier layers is varied with depth, as shown in Figure 3.1(c). The lowest barrier has the lowest refractive index in the core. n_s is the refractive index of the substrate (or lowest cladding region), n_w is the refractive index of the well layers and n_i is the refractive index if the i'th barrier in the core. This refractive index gradient across the waveguide core is always referred to as positive, so that a negative gradient profile has the *highest* index barrier layer nearest the substrate. These structures utilize the good control of layer composition available with MBE and MOCVD growth techniques.

The V shaped graded-step index profile is shown in Figure 3.1(d). The variation again occurring in the barrier layers in the core region, and here the barriers with highest index are the outermost layers of the guiding region and the barrier with lowest index is at the center of the guiding region; note unlike the other two profiles studied above this waveguide has a symmetrical core structure since the upper and lower cladding layers have the same refractive index. n_{cl} is the refractive index of the cladding layers.

Ohke *et al.*[7,8] evaluated a squared mean weighted refractive index for the core region of a multi-layer waveguide, where the well and barrier were of constant composition and thickness, and showed that this expression was appropriate for representing structures with >50 layers and layer thicknesses <200 Å by a simple three layer structure with guiding layer index given by,

$$n_e^2 = \frac{n_b^2 + r n_w^2}{1+r} \qquad \text{-(3.11)}$$

However, for the waveguide structures studied here, as the structures contain different layer compositions a modified expression has been used which involves a sum over individual layers (see Equation (3.12)). Alman *et al.*[9] used perturbation theory to derive an optimal expression for

the *rms* guiding region index of an equivalent three layer structure, for a general MQW waveguide, which involved integration of the electric field and products of the electric field and refractive index variation over the region of interest. They also showed that by using the assumption that the electric field varies slowly over each period of the structure, the optimal expression can be shown to be equivalent to Equation (3.12). Hence it was thought to be appropriate to look at the validity of using Equation (3.12) for the type of structures studied here.

$$n_e^2 = \frac{\sum L_i n_i^2}{T_c} \qquad \text{-(3.12)}$$

In Equation (3.11) n_b is the refractive index of the barrier, n_w is the refractive index of the well and r is the ratio of well width to barrier width. In Equation (3.12) L_i is the width of the i'th layer in the core region, n_i is the refractive index in that layer, T_c is the total width of the core region and the sum extends over all layers in the core region. Note that Equation (3.11) is only applicable for a large number of layers, and (3.12) approaches (3.11) for structures of constant layer thickness and composition as the number of layers increases (see Figure 3.2.), as the effect of having an extra barrier compared to the number of wells diminishes. Equations (3.11) and (3.12) are applicable for TE modes, as studied here, but further expressions need to be used for the case of TM modes.

The refractive index values used here were those of the bulk material, although it is appreciated that the actual refractive index values of the structure are determined by the thickness and composition of each layer, which in turn determine the transition energies and therefore the absorption and refractive index of the multiple QW structure[6-8]. However, since we are concerned here with the determination of the characteristics of such multi-layer waveguide structures, provided the values used are in the correct range, the precise values use are not so important. When the model is to be used to predict the experimental performance characteristics of specific waveguide structures the absorption and refractive index determined from quantum mechanical considerations must be included.

For demonstration purposes and applicability to the thesis as a whole, we consider here multi-layer waveguides in the AlGaAs/GaAs material system, although this model is equally suited to

any such material system. In order to utilize quantum confinement effects, the well layer thickness is restricted to ~200Å while the composition of both well and barrier layers can vary from AlAs to GaAs, which defines the limits of the refractive index values of the waveguide structures for any thickness and composition. All calculations are performed using a free space optical wavelength of 1.3 μm. The material parameters used have been determined using published values[18,19] and, where such information is not available, linear interpolation between known values has been used to determine the values used in the model. The values used and the sources of the data are given in Table 3.1. For material systems where there is a greater refractive index difference between the well and barrier layers, it is thought that the layered nature of the waveguide characteristics would result in more pronounced characteristics for these graded multi-layer waveguides.

Al fraction	0.0	0.1	0.2	0.3	0.4	0.5	0.6	0.7	0.8	0.9	1.0
Refractive index	3.41	3.36	3.31	3.26	3.21	3.16	3.11	3.06	3.01	2.96	2.91

Table 3.1 Values of refractive indices used for calculations. Taken from References 18 and 19.

3.4 RESULTS AND DISCUSSION

Both polarisations were investigated and, since they both showed the same trends, the majority of the results presented below are for the TE polarisation. Some of the results for the corresponding TM modes are also presented in order to indicate that the qualitative nature of the results shown here is also applicable to these modes. In addition, using well and barrier layers of uniform composition and varying the thickness of the layers can be used to obtain similar effects although the results are not presented here. The most significant difference is that such effects would require large changes of layer thickness which is a parameter that is of fundamental importance to device and circuit design.

3.4.1 'Linearly graded' profiles

The linear graded waveguides, whose refractive index profile is shown in Figure 3.1(c), are fabricated by varying the composition of the $Al_xGa_{1-x}As$ barrier layers between GaAs and AlAs, i.e. between x=0 and x=1.0 depending on the gradient of the transverse refractive index profile.

The fundamental mode field profile for various refractive index positive gradients for constant layer thickness and number of layers are shown in Figure 3.3 for an MQW waveguide with an $Al_{0.1}Ga_{0.9}As$ upper barrier layer in all of the structures and the lowest barrier layer having the relevant composition for the required positive gradient. These results show that as the gradient of the profile is increased (i.e. in going from curve A to curve D in Figure 3.3), the peak mode field is moved toward the core/upper cladding interface of the waveguide. As the index profile gradient is reduced, the confinement of the propagating mode is also reduced and the evanescent field at the surface interface is reduced. The fields at the core cladding interfaces are of importance since the scattering loss is determined in part by the field magnitude at this interface[20]. Since these structures are asymmetric waveguides, using a multi-layer core region enables the confinement of the mode, and therefore the depth of the peak mode field, to be tailored for various applications such as low radius bends, which require well confined modes, and evanescent field sensors which require large evanescent fields at the upper waveguide core cladding interfaces. Also, this tailoring technique could be used to offset the shifting of the mode field profile seen in curved waveguides[21] which can result in a reduction in coupling between different shaped waveguides. The substrate is assumed to have the same refractive index as the lowermost barrier layer.

Increasing the well and barrier layer thickness beyond those required for quantum confinement, which results in a multi-layer waveguide core region, produces the fundamental mode field profiles for a range of index gradients shown in Figure 3.4. They show the same trends as those obtained for the MQW waveguides although oscillations due to the layered nature of the waveguide core region and the size of those layers in comparison to an optical wavelength, are superimposed on the fundamental mode field profiles of the multi-layer waveguides. They are not found in Figure 3.3 as the number of layers and therefore the period of these oscillations is too high to be resolved in these field profiles. In this structure the waveguide core is much thicker than the MQW core, so that the number of modes supported by it is much larger and the fundamental mode evanescent fields are much smaller. If a multi-layer waveguide structure has a core width the same as the MQW case, then it is found that a similar number of modes to that of the MQW case are supported by the waveguide, and as the number of layers is reduced, and hence the thickness of each layer is increased to keep the core width the same, the guided modes increase in amplitude and their confinement improves.

The variation of effective index (β/k) with the gradient of the linearly graded step index profile is shown in Figure 3.5 for the two above structures. The effective index can be seen to decrease with increasing gradient, and the effect is more pronounced in the MQW structures. Here the gradient is normalised so that a gradient of 1.0 corresponds to an Aluminium fraction of 1.0 in the layer above the substrate and 0.1 in the uppermost layer of the structure, a gradient of zero corresponds to an Aluminium fraction of 0.1 in all AlGaAs layers in the guiding region. All other gradients follow by linear interpolation. The number of guided mode solutions was found to increase with increasing gradient of the index profile when as in this case the changes in gradient are brought about through *increasing* Aluminium concentrations within the structure, with the MQW structures being either single mode or supporting 2 modes and the multi-layer waveguide structures supporting up to 10 modes.

These results suggest that it is possible to control the depth of the peak field in both MQW and multi-layer waveguides, (see Figures 3.6 and 3.7). The fundamental mode can be seen to be moved to either side of the core region using the appropriate sign of the index gradient; a positive gradient moves it towards the upper cladding/core interface and a negative gradient moves it towards the lower cladding/core interface. For MQW waveguides the size of the guiding region is critical to the effectiveness of this effect since, if the guiding region is too thin the control over the depth of the peak mode field is reduced. Guiding regions of less than ~1 optical wavelength produced this type of reduction in the movement of the peak.

3.4.2 'V' shaped profiles

Using a "V" shaped refractive index profile in a multi-layer waveguide is interesting since the fundamental transverse mode field profile has two field maxima, one above the other, see Figure 3.8. In this structure the waveguide core effectively has two guiding layers, one above the other. The waveguide structure splits the input beam between the two spatially separated guiding regions and this waveguide structure may be considered to be a vertically integrated 3dB waveguide coupler. Also, the coupling ratio of the two output beams may be varied using different positive and negative index gradients. For the case of typical multi-layer waveguides, the gradient of the V profile is also critical since the fundamental mode has only one field maximum

when the gradient of the V profile is large and additional oscillations are also superimposed on the mode profile as can be seen in Figure 3.8.

For MQW structures with a "V" shaped index profile, the thickness of the waveguide core region is critical, and can be changed by increasing either the number of layers or the layer thickness. More specifically, if the guiding region width is significantly less than the wavelength of the optical mode, the effect is not seen. "V" profiles in well composition can be used also, either separately from or in concurrence with the barrier variations to produce similar effects. Figure 3.9 shows an example of the splitting of the TE_0 mode in such MQW waveguides.

The same type of behaviour can be observed using variations in layer thickness instead of composition, although the effect does not seem to be so pronounced as that of compositional variations. In addition, it is more complicated since variations in layer thickness are inextricably linked to other factors such as the width of the guiding region and the number of layers.

Using Equation (3.12) to define a square mean weighted index it was found that in many cases an equivalent three layer structure could not re-produce the effects shown here, and in some cases the appropriate three layer structure had no guided mode solutions. More specifically, structures with a high index profile gradient may have such a high Aluminium content that the calculated equivalent three layer structure has a core index that is significantly less than the substrate, and will not support guided mode solutions.

3.4.3 TM polarisations

As has been discussed, these type of waveguide structures can also support TM modes as well as the TE modes for which results have been given. The determination of the TM mode profiles has been discussed in section 3.2.2, and the results obtained for those modes show the same trends as those given for the TE modes. For example, Figures 3.10 and 3.11 show the TM_0 mode profiles for the MQW and multi-layer waveguide structures of Figures 3.3 and 3.4 respectively. It can be seen that as in the TE case the optical mode profile is moved towards the core/upper cladding interface of the waveguide structure. Further investigations of the TM modes indicate that the effect on the TM mode profiles due to varying the

refractive index profiles in the manner already shown for TE modes, follows the same trend as that of the TE modes.

3.4.4 Quantum well effects

When considering MQW waveguides it must be remembered that the actual refractive index of the structure will be modified by the effects of quantum confinement, and to this end some variations in well refractive index were studied in order to try and estimate the significance of the quantum effects with respect to the nature of the results shown here. Refractive index variations of up to ±5% produced slight variations of the transverse mode field profile although they were not found to be significant enough to alter the qualitative nature of the results. Previous work[22] has shown that for MQW waveguides, the effects of significance on the confinement of optical modes are the guiding region thickness and the number of layers, as opposed to quantum confinement effects. In this respect the trends of the results are thought to be applicable to real quantum well structures.

3.5 SUMMARY

The results presented above show that for waveguides with graded-stepped refractive index profiles, the depth of the peak of the mode field profile may be moved across the waveguide core, with the gradient of the profile determining the actual position of the peak mode field.

The fundamental modes in waveguides with both positive and negative gradients in the transverse refractive index profile have two spatially separated field maxima such structures may be of use as vertically integrated coupled waveguide structures. The effect of layer thicknesses on the properties of the waveguides results in similar, less pronounced effects while no significant mode splitting was found for asymmetric waveguides.

References

[1] Landolt-Börnstein, *Numerical Data and Functional Relationships in Science and technology*, Group III, Volume 17a: *Semiconductors : Physics of Group IV elements and III-V compounds*, Ed. O.Madelung, Springer-Verlag, Berlin, (1982)

[2] Tsai, C.S. *Guided wave acousto-optics : Interactions, devices and applications*, Springer series in Electronics and Photonics, Vol. 23, Springer Berlin, New York. (1990)

[3] Chatenoud, F., Dzurko, K.M., Dion, M., Moss, D., Barber, R., Delâge, A. and Landheer, D. "GaAs-AlGaAs multiple quantum well lasers for monolithic integration with optical modulators", Can. J. Phys., **69**, pp.491-496, (1991)

[4] Wood, T.H. "Multiple quantum well (MQW) waveguide modulators", J. Lightwave. Technol., **6**, pp.743-757, (1988)

[5] Kraus, J. and Deimel, P.P. "Calculation of the propagation constant of the optical modes in multi-quantum-well structures", IEEE J. Quantum Electron., **QE-26**, pp.824-826, (1990)

[6] Cvetkovic, S.R. and Zhao, A.P. "Finite element formalism for linear and nonlinear guided waves in multiple-quantum-well waveguides", J. Opt. Soc. Am. B, **10**, pp.1401-1407 (1993)

[7] Ohke, S., Umeda, T. and Cho, Y. "Optical waveguides using GaAs/$Al_xGa_{1-x}As$ multiple quantum well", Opt. Commun., **56**, pp.235-239, (1985)

[8] Ohke, S., Umeda, T. and Cho, Y. "TM-mode propagation and form birefringence in a GaAs/AlGaAs multiple quantum well optical waveguide", Opt. Commun., **70**, pp.92-96, (1989)

[9] Alman, G.M., Motter, L.A., Shen, H. and Dutta, M. "Refractive index approximations from linear perturbation theory for planar waveguides", J. Quantum Electron., **QE-28**, pp.650-657, (1992)

[10] Skinner, I.M., Shail, R. and Weiss, B.L. "Modal propagation within MQW waveguides", IEEE J. Quantum Electron., **25**, pp.6-11, (1989).

[11] Kumar, M., Boyd, J.T., Jackson, H.E. and Weiss, B.L. "Birefringent properties of GaAlAs/GaAs multiple quantum well waveguides", IEEE J. Quantum Electron., **28**, pp.1678-1688, (1992).

[12] Zhao, A.P., Cvetkovic, S.R. and Punjani, M. "Analysis of stripe multilayer waveguides with effective index and finite element methods", IEEE J. Quantum. Electron., **QE-28**, pp.573-579, (1992).

[13] Kahen, K.B. and LeBurton, J.P. "Optical constants of GaAs-AlGaAs superlattices and multiple quantum wells," Phys. Rev. B., **33**, pp.5465-5472, (1986).

[14] Hunsperger, R.G. *Integrated optics: Theory and technology*. Third edition. chapter 3, New York: Springer-Verlag, (1991).

[15] Hecht, E. *OPTICS*, Addison-Wesley, page 621, Second edition, (1987)

[16] See for example, Press, W.H., Teukolsky, S.A., Vetterling, W.T. and Flannery, B.P., *NUMERICAL RECIPES in C, The Art of Scientific Computing*, Second edition, Cambridge University Press (1994)

[17] Klingshirn, C.F. *Semiconductor Optics*, Chapter 2, Springer Berlin, New York, London, (1995)

[18] "Properties of Gallium Arsenide," 2nd edition, INSPEC EMIS Datareview Series no. 2, (1990).

[19] Adachi, S. "GaAs, AlAs, and GaAs-$Al_xGa_{1-x}As$: Material parameters for use in research and device applications," J. Appl. Phys., **58**, pp.R1-29, (1985).

[20] Naden, J.M. and Weiss, B.L. "Optical properties of planar waveguides formed by He^+ implantation in $LiNbO_3$," J. Lightwave. Technol., **LT-3**, pp.855-859, (1993).

[21] Smit, M.K., Pennings, E.C.M. and Blok, H. "A normalized approach to the design of low-loss optical waveguide bends," J. Lightwave. Technol., **LT-11**, pp.1737-1742, (1993).

[22] Kraus, J. and Deimel, P.P. "Full-width-half-maximum and confinement of optical modes in multiple-quantum well laser structures," J. Lightwave.Technol., **LT-11**, pp.1802-1805, (1993).

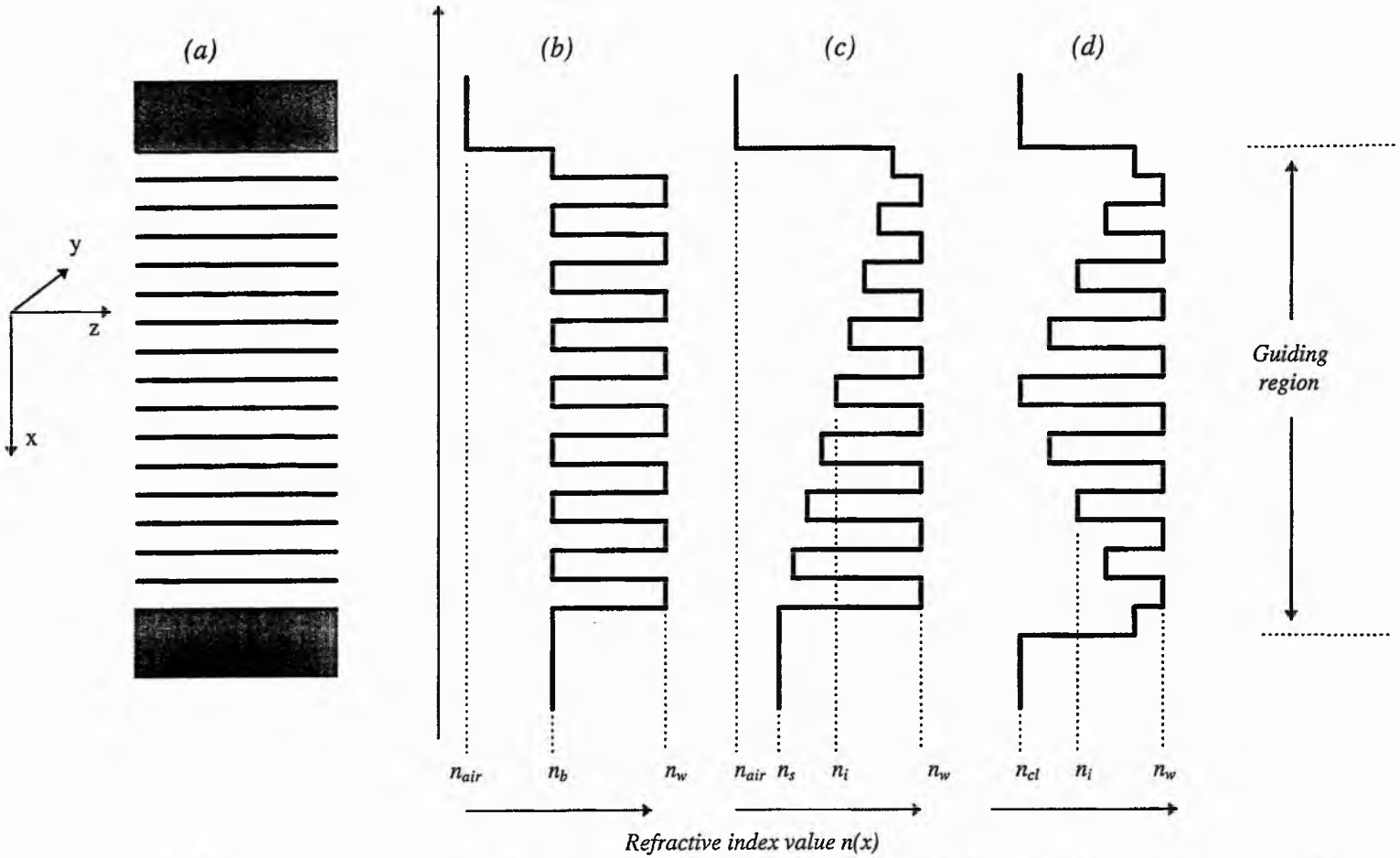

Figure 3.1 *The transverse refractive index profiles of the symmetric and asymmetric planar waveguides modelled here: (a) Generic multilayer waveguide structure and coordinate system, (b) refractive index profile of standard multilayer waveguide structure with the well and barrier composition constant throughout the structure, (c) "linearly graded-step" refractive index profile, and (d) "V" graded-step refractive index profile*

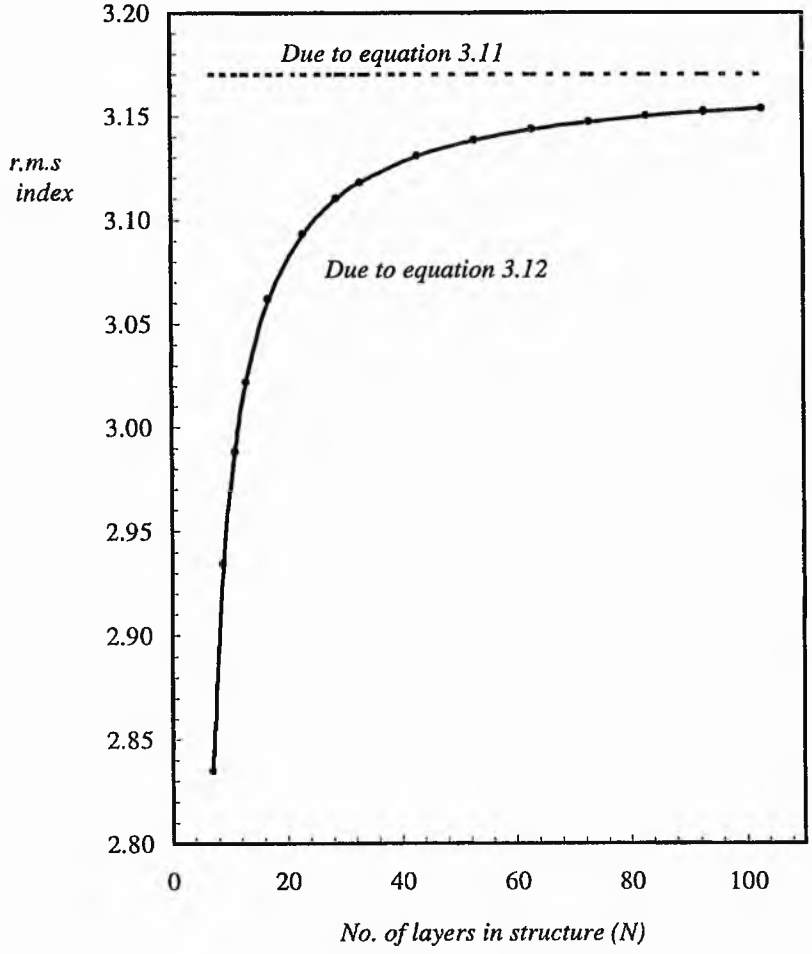

Figure 3.2 *The comparison of the calculated root mean squared refractive index values for a multilayer waveguide structure with barrier and well layer thickness and composition constant throughout the structure. All layer thicknesses are 0.1μm. Structure is:- Air/AlAs/GaAs/...../GaAs.*

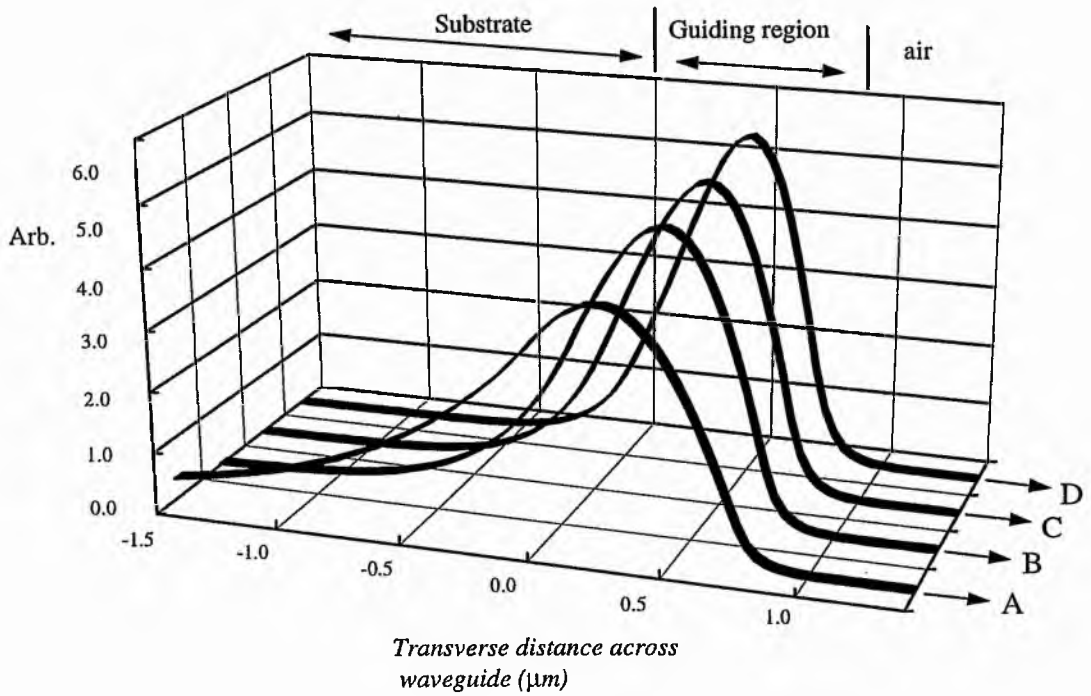

Figure 3.3 *The movement of the fundamental TE mode profile toward the surface of the guiding structure in MQW waveguides due to linearly graded step profiles with a positive gradient. Well width (L_z) = 80 Å, barrier width (L_b) = 120 Å, 81 layers. Profile gradient increasing with A→B→C→D.*

A :- x=0.2 in substrate/ x=0.2 to 0.1 in core / x=1.0 (air),
B :- x=0.4 in substrate/ x=0.4 to 0.1 in core / x= 1.0 (air),
C :- x=0.6 in substrate/ x=0.6 to 0.1 in core / x=1.0 (air),
D:- x=1.0 in substrate/ x=1.0 to 0.1 in core / x=1.0 (air)

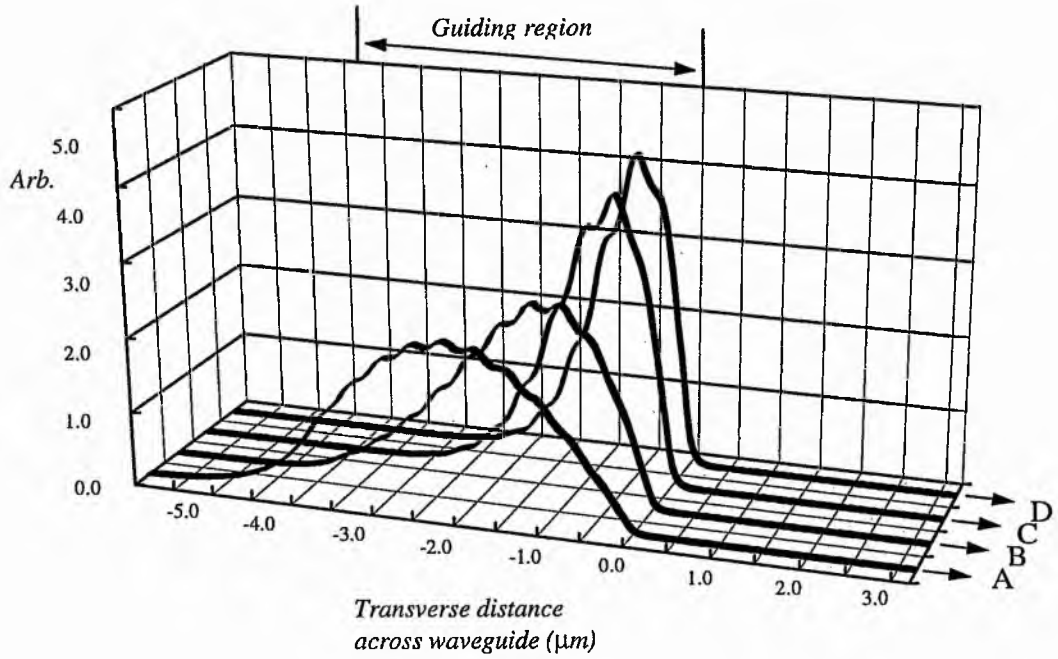

Figure 3.4 *The movement of the fundamental TE mode profile toward the surface of the guiding structure in multi-layer waveguides due to linearly graded step profiles with a positive gradient. All layer thicknesses are 0.2μm, 21 layers in the guiding region. Profile gradient increasing with A→B→C→D.*

A:- x=0.1 in all cladding layers and substrate,
B:- x=0.2 in substrate/ x=0.2 to 0.1 in core / x=1.0 (air),
C:- x=0.6 in substrate/ x=0.6 to 0.1 in core / x=1.0 (air),
D :- x=1.0 in substrate/ x=1.0 to 0.1 in core/ x=1.0 (air)

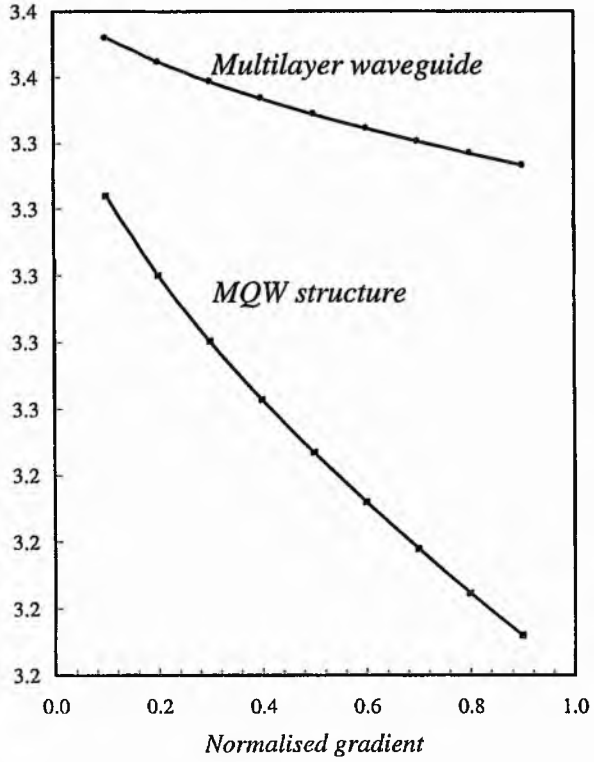

Figure 3.5 *The variation of the effective index of the fundamental TE mode due to varying gradients of the linearly graded step index profiles in MQW and multi-layer waveguides. All gradients are positive with compositional variations in the barriers.*
MQW :- L_z=80Å, L_b=120Å, 81 layers.
Multilayer :- All layers 0.2μm, 23 layers

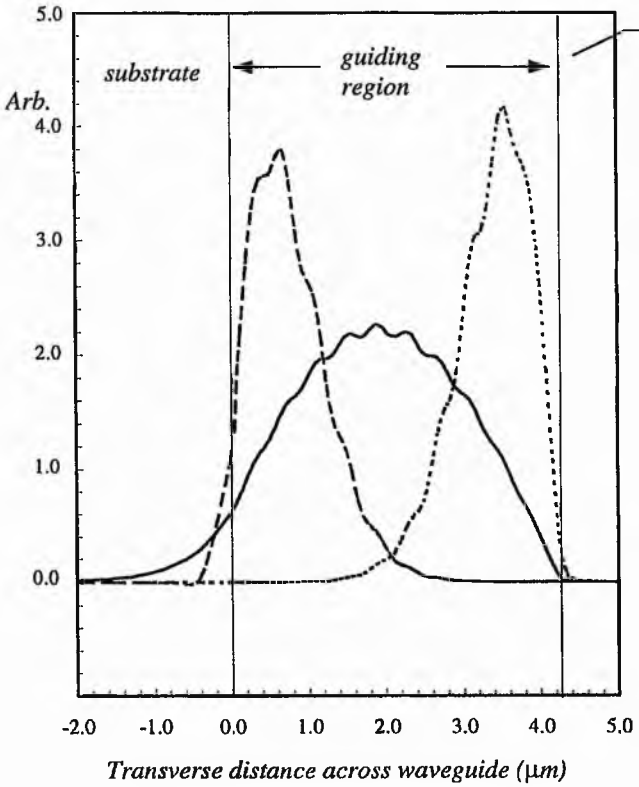

Figure 3.6 *The control. of the transverse position of the fundamental TE mode in multi-layer waveguides using positive and negative gradient step profiles. All layer thicknesses are 0.2 μm with 21 layers in the guiding region. (—)$Al_{0.1}Ga_{0.9}As$ in all cladding layers and substrate, (----)AlAs in substrate and lowest barrier and $Al_{0.1}Ga_{0.9}As$ in top barrier, (····) $Al_{0.1}Ga_{0.9}As$ in lowest barrier and AlAs in top barrier and substrate.*

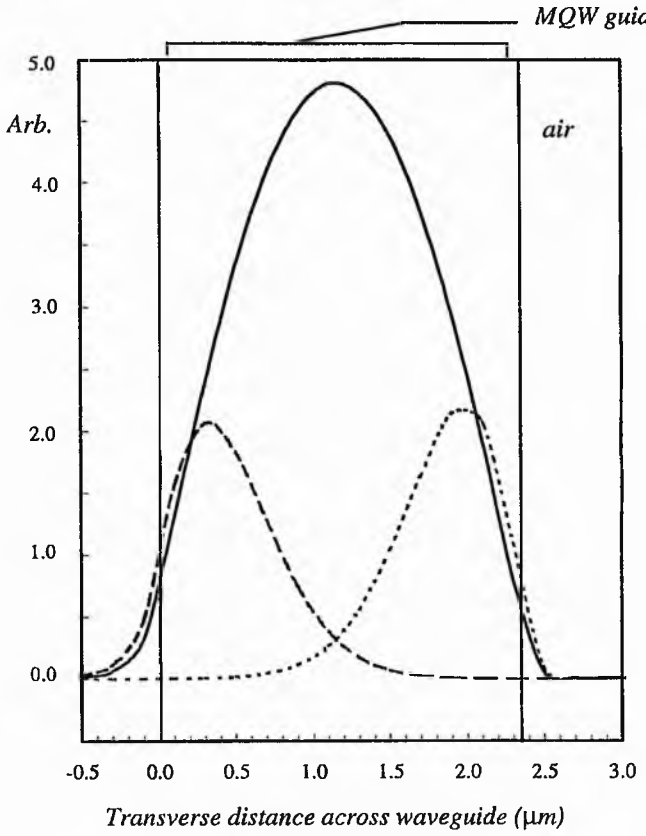

Figure 3.7 *The control. of the transverse position of the fundamental TE mode in MQW waveguides using positive and negative gradient step profiles. Lz = 80Å, Lb=500Å and 81 layers in the guiding region. (——) $Al_{0.1}Ga_{0.9}As$ in all the caldding layers and AlAs in substrate, (-----) AlAs in the substrate and in lowest barrier and $Al_{0.1}Ga_{0.9}As$ in the top barrier, (····)$Al_{0.1}Ga_{0.9}As$ in the lowest barrier and AlAs in the top barrier and substrate.*

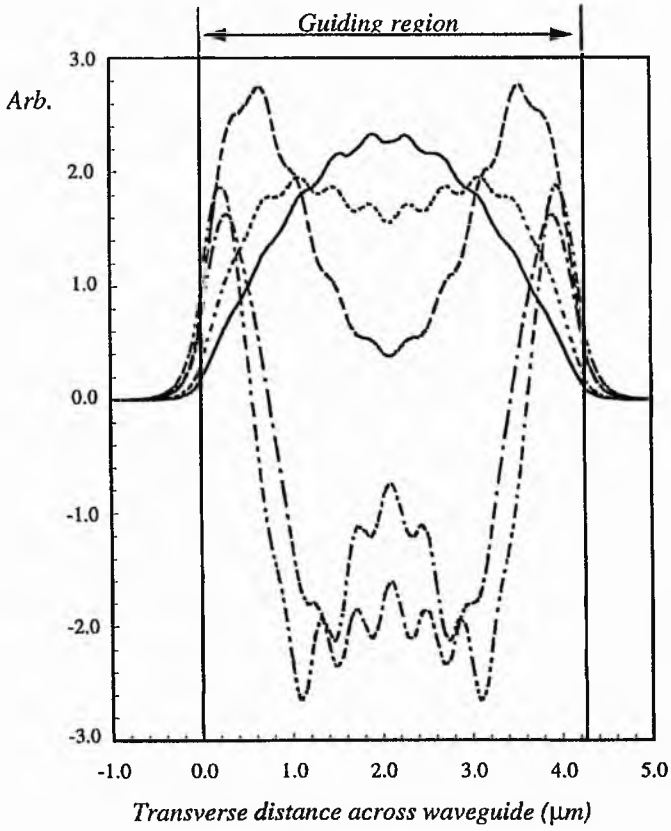

Figure 3.8 *The transverse splitting of the fundamental TE mode in symmetrical multilayer waveguides. All layer thicknesses are 0.2 μm with 21 layers in the guiding region. AlAs cladding layers. "V" shaped profiles in waveguide cores :*
Aluminium fractions in core:-

- *0.1/···1.0···/0.1*
- *0.1/···0.6···/0.1*
- *0.1/···0.5···/0.1*
- *0.1/···0.2···/0.1*
- *0.1/···0.1···/0.1*

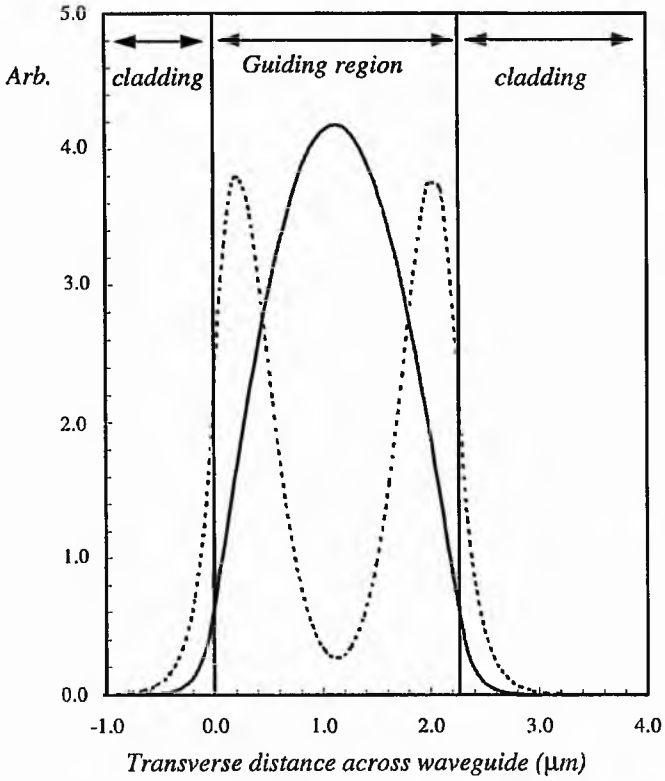

Figure 3.9 *The transverse splitting of the fundamental TE mode in symmetrical MQW waveguides. L_z =80Å, L_b=500Å with 40 layers in guiding region. AlAs cladding layers with a "V" graded step profile in barrier layer composition*

——— *x=0.1 in all barrier layers in guiding region.*

- - - - *x=0.1 at edges of guiding region and 1.0 in the middle*

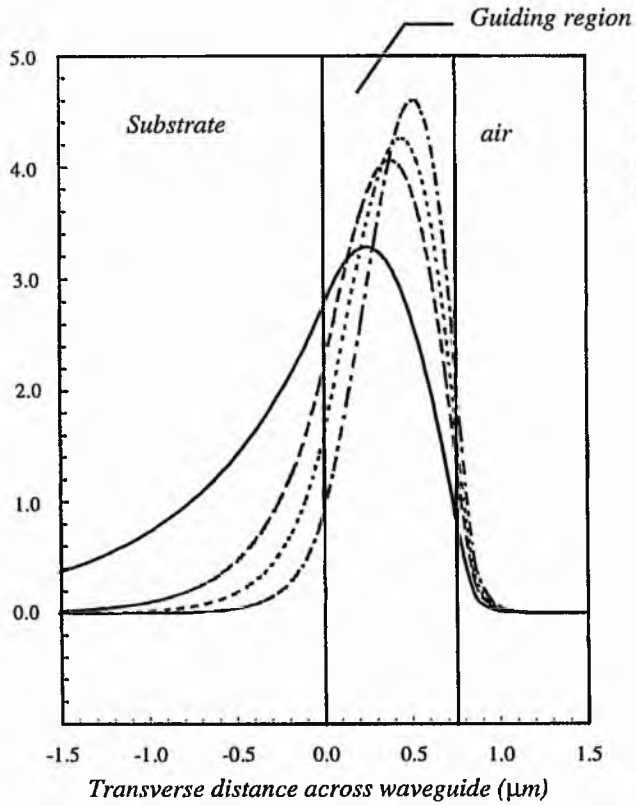

Figure 3.10 *TM_0 mode profles for the MQW waveguide structure of Figure 3.3*

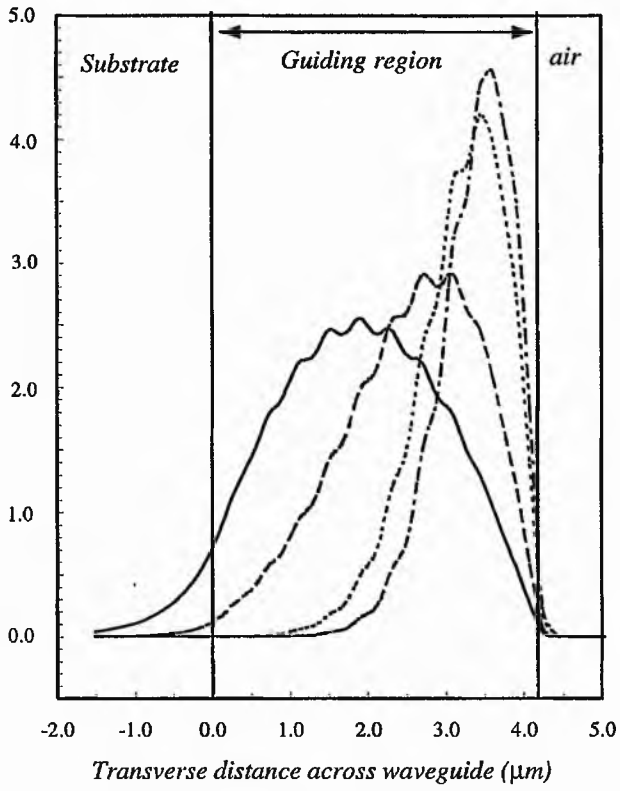

Figure 3.11 *TM_0 mode profiles for the multilayer waveguide structure of Figure 3.4*

Chapter 4

Acousto-Optic Diffraction in Multi-layer and Multiple Quantum well Waveguides

4.1 INTRODUCTION

The modelling of surface acoustic waves (SAWs) and guided optical modes in relevant structures has been achieved and discussed in chapters 2 and 3 respectively. In studying the subsequent acousto-optic diffraction in such structures, the results of chapters 2 and 3 will provide input to the solution of the problem and it will clearly be of interest to consider the compositionally induced changes in the SAW induced quantities and guided optical modes that have been discussed, and their effect on the diffraction process.

Many guided wave devices are based on acousto-optic interactions, such as modulators[1], beam deflectors[2], and spectrum analysers[3]. As the technology of opto-electronic integrated circuits develops, the need for more efficient, wide band acousto-optic interaction in materials such as GaAs becomes apparent. Quantum well structures provide the possibility of enhanced electro-optic effects and therefore more efficient devices[4,5]. Hence it is of interest to study acousto-optic interactions in multi-layer structures of quantum well dimensions.

The building block of many acousto-optic devices is the Bragg cell, which was discussed in chapter 1 and is shown schematically in Figure 4.1. The cell has a planar waveguide structure, with an interdigital transducer (IDT) fabricated on the surface to generate the SAW. The passage of the SAW forms an optical grating that moves across the path of the incident guided light, at a particular SAW frequency the Bragg condition will be satisfied and the incident optical mode will be diffracted.

The theory behind the acousto-optic interaction involved in the Bragg cell is based on a coupled mode theory approach[6,7], in which the effect of the SAW is represented as a perturbation to the modes of the planar waveguide structure, resulting in an exchange of power between them. The perturbed modes are expanded using the set of unperturbed modes as a basis, and by substituting the perturbed modes into the appropriate wave equation, an expression for the diffraction efficiency can eventually be obtained[8].

In this chapter the results of a study of the variation of the diffraction efficiency with various design parameters, such as the transducer length, acoustic power flow and specific material composition will be presented. The scope of the investigation is concentrated on the possibilities for increasing the diffraction efficiency.

4.2 THEORY

Referring to Figure 4.1 for a brief development of the theory, the SAW is assumed to propagate in the z direction with acoustic frequency Ω and momentum vector $\underline{K}$. The optical mode propagates in the x, z plane, with optical frequency ω_n and momentum vector k_n, and when the Bragg condition is satisfied the mode is incident to the momentum vector of the SAW with angle θ_B, the Bragg angle. Considering the electric field, the wave equation obeyed by the unperturbed modes is,

$$\nabla^2 \mathbf{E}(r,t) = \mu\varepsilon \frac{\partial^2 \mathbf{E}}{\partial t^2} \qquad \text{-(4.1)}$$

where **E** is the electric field vector. The optical modes have an amplitude profile that varies with depth and has previously been determined using the method outlined in chapter 3. In vacuum the electric displacement of an electromagnetic wave is proportional to the electric field, and when light travels through matter the electric displacement becomes modified by the addition of a polarisation term. The perturbation provided by the SAW is assumed to contribute a distributed polarisation source $P_{pert}(\boldsymbol{r},t)$, from which the wave equation for the perturbed case follows, and is of the form,

$$\nabla^2 E_y(\boldsymbol{r},t) = \mu\varepsilon \frac{\partial^2 E_y}{\partial t^2} + \mu \frac{\partial^2}{\partial t^2}[P_{pert}(\boldsymbol{r},t)]_y \qquad \text{-(4.2)}$$

The SAW induces strains in the structure and in the case of III-V materials, for certain SAW propagations the strains piezoelectrically induce electric fields (as mentioned in chapter 2). It is these SAW induced fields that contribute to $P_{pert}(\boldsymbol{r},t)$, and their effect is expressed through the changes that occur in the electric permittivity (or alternatively the refractive index), together with the corresponding elasto-optic and electro-optic tensors. More specifically, the linear electro-optic contribution is defined conventionally as in section 1.2.3 in terms of a third rank tensor as[9]

$$\Delta\varepsilon_{ij} = \frac{\varepsilon_i \varepsilon_j}{\varepsilon_0} r_{ijk} E_k \qquad \text{-(4.3)}$$

where ε_i signifies the main diagonal elements of the permitivitty tensor (i.e. $\varepsilon_i \equiv \varepsilon_{ii}$) and the elasto-optic effect is defined by relating the effects of the strain on the constants of the index ellipsoid through[10]

$$\Delta\left(\frac{1}{n^2}\right)_{ij} = p_{ijkl} S_{kl} \qquad \text{-(4.4)}$$

where p_{ijkl} are the elasto-optic tensor components and S_{kl} are the strain tensor components.

The analysis follows the method that was used by Ohmachi[11] for purely elasto-optic behaviour and later developed by Tsai *et al.*[12,13] to include piezoelectric materials. The perturbed and perturbing fields are assumed to have the following forms

$$\hat{E}_m(x,y,z,t) = \frac{1}{2}E_m(x)U_m(y)\exp(j[\omega_m t - k_{m_x}x - k_{m_z}z]) + c.c. \qquad -(4.5)$$

$$\hat{E}_n(x,y,z,t) = \frac{1}{2}E_n(x)U_n(y)\exp(j[\omega_n t - k_{n_x}x - k_{n_z}z]) + c.c. \qquad -(4.6)$$

$$\hat{S}(y,z,t) = \frac{1}{2}S_I U_{aI}(y)\exp(j[\Omega t - Kz + \phi)] + c.c \qquad -(4.7)$$

$$\hat{E}_p(y,z,t) = \frac{1}{2}E_{pi}U_{pi}(y)\exp(j[\Omega t - Kz + \phi]) + c.c. \qquad -(4.8)$$

where $\hat{E}_m$ and $\hat{E}_n$ are the undiffracted and diffracted electric fields respectively, S is the SAW induced strain and $\hat{E}_p$ is the SAW induced electric field accompanying this strain through the piezoelectric effect. $U_m(y)$ and $U_n(y)$ are the normalised field distributions of the optical waves along the waveguide thickness and have been calculated using the method outlined in chapter 3. $U_{aI}(y)$ and $U_{pi}(y)$ are the normalised field distributions of the components of the SAW induced strains and electric fields respectively and have been calculated using the method of Laguerre polynomials outlined in chapter 2. *c.c* refers to the complex conjugate, and the subscripts I and i correspond to the indices of the strain tensor and electric field vector over which summation occurs.

If Equations (4.5-4.8) are substituted into the wave equation (4.2) together with the expressions for the electro-optic and elasto-optic changes to the dielectric constant (Equations (4.3) and (4.4)) which will contribute to the additional polarisation, then a set of coupled differential equations is obtained which can be reduced to the following form :-

$$\frac{\partial^2 E_m(x)}{\partial x^2} - jK\Delta\theta\frac{\partial E_m(x)}{\partial x} + ABE_m(x) = 0 \qquad -(4.9)$$

$$\frac{\partial^2 E_n(x)}{\partial x^2} + jK\Delta\theta \frac{\partial E_n(x)}{\partial x} + ABE_n(x) = 0 \qquad \text{-(4.10)}$$

where $\Delta\theta$ is the deviation of the incident angle of the light from the Bragg angle and

$$A = \frac{\omega_n^2 n_m^2 n_n^2}{4c^2 k_m \cos\theta_m} \times \frac{\int_0^{\infty} U_m(y)U_n(y)\left\{p{:}S_a U_a(y) + r{:}E_p U_p(y)\right\}dy}{\int_{-\infty}^{+\infty} U_m^2(y)dy} \qquad \text{-(4.11)}$$

$$B = \frac{\omega_m^2 n_m^2 n_n^2}{4c^2 k_n \cos\theta_n} \times \frac{\int_0^{\infty} U_m(y)U_n(y)\left\{p{:}S_a U_a(y) + r{:}E_p U_p(y)\right\}dy}{\int_{-\infty}^{+\infty} U_n^2(y)dy} \qquad \text{-(4.12)}$$

with (:) signifying the appropriate tensor multiplication. General solutions are easily found by matching the boundary conditions $E_m(0) \equiv 1$ and $E_n(0) \equiv 0$ and then the diffraction efficiency $\zeta(f)$ which is defined as the ratio of diffracted light power at $x=L$ to incident power at $x=0$ of the interaction region can be expressed in the following form :-

$$\zeta(f) = g^2(f)\left[\frac{\sin\sqrt{g^2(f) + (K\Delta\theta L/2)^2}}{\sqrt{g^2(f) + (K\Delta\theta L/2)^2}}\right]^2 \qquad \text{-(4.13)}$$

where f is the frequency of the SAW, K is the momentum vector of the SAW, L is the acoustic aperture, $\Delta\theta$ is the variation of the incident light wave from the Bragg angle, and $g^2(f)$ is given by

$$g^2(f) = \frac{\pi^2}{4\lambda_o^2}\left[n_m^3 n_n^3 |\Gamma_{mn}(f)|^2 \frac{L^2}{\cos\theta_m \cos\theta_n}\right] \qquad \text{-(4.14)}$$

where λ_o is the optical wavelength, n_m, n_n are the effective indices of the diffracted and undiffracted modes respectively, θ_m, θ_n are the diffracted and incident angles respectively and $|\Gamma_{mn}|^2$ contains the overlap of the diffracted, undiffracted modes, and the SAW induced electric field and strain profiles, and is given by ;

$$|\Gamma_{mn}(f)|^2 = \frac{\left|\int_0^{\infty} U_m(y)U_n(y)\{p{:}S_aU_a(y) + r{:}E_pU_p(y)\}dy\right|^2}{\left|\int_{-\infty}^{+\infty} U_m^2(y)dy\right|\left|\int_{-\infty}^{+\infty} U_n^2(y)dy\right|} \qquad \text{-(4.15)}$$

Where, in this equation and all preceding ones y represents the depth below the surface of the structure, U_m and U_n are the amplitude profiles of the diffracted and undiffracted modes respectively, p and r are the elasto-optic and electro-optic tensors respectively. As in the SAW analysis of chapter 2, the elasto-optic and electro-optic tensors p and r must be transformed into the co-ordinate system of Figure 4.1, this was done again according to Auld[14]. U_p and U_a represent the normalised SAW induced field distributions along the waveguide thickness, they have been determined using a Laguerre polynomial technique[15] and take the form,

$$u_j = \sum_{m=0}^{\infty} p_m^j \left| m(y) \right\rangle \qquad \text{-(4.16)}$$

where,
$$\left| m(q_2) \right\rangle = \exp[-(q_2 / 2)] L_m(q_2) \Big/ m!$$

and L_m is the m'th Laguerre polynomial. u_j corresponds here to either a strain or an electric field component and p^j_m to the eigenvectors obtained from the eigen-problem outlined in chapter 2.

$|\Gamma_{mn}|^2$ was found numerically by determination of the integrals in Equation (4.15) for each layer and summing over all layers, as each layer in the structure would be represented by different electro-optic and elasto-optic tensor quantities. Numerical Algorithms Group (Nag) sub-routines were used to perform the integrals. Once $|\Gamma_{mn}|^2$ was found the diffraction efficiency (4.13) could be determined from Equations (4.14) and (4.15).

4.3 ACOUSTO-OPTIC INTERACTIONS IN DEVICE STRUCTURES

4.3.1 Procedure

The results presented here are for TE guided optical modes with SAW propagation in the [110] direction on the {100} plane of the III-V structure. The approach taken here is one of assuming that the SAW is propagating freely and in this sense no account is taken of it's generation or of the conversion efficiency of the transducer that generates it. The deviation from the Bragg angle is assumed to be zero for the results shown here resulting in a simplified expression for the diffraction efficiency.

For a given SAW frequency and power and a specific structure, the form of the SAW induced fields were calculated and duly obtained in the form of Equation (4.16). The optical mode profiles were then calculated and together with the SAW induced fields, allowed the calculation of the overlap function in Equation (4.15). Once the overlap function was determined, the diffraction efficiency could be calculated. Repeating this procedure for a range of SAW wavelengths allows the generation of graphs of diffraction efficiency against acoustic frequency since the acoustic surface velocity is also obtained from the Laguerre polynomial technique. By varying the acoustic power, acoustic aperture and material composition, a range of graphs can be obtained that show the effects of the various acousto-optic diffraction parameters.

In general the structures dealt with here are single mode waveguide structures, and the diffracted and undiffracted modes are assumed to be the same, a case known as isotropic diffraction. Some of the structures considered here have layer dimensions of the order of quantum well dimensions, however quantum effects are not considered.

For real quantum well structures it must be noted that at optical wavelengths close to the confined energies of the well, there will be other contributions to the electro-optic effect of the structure[16] probably resulting in extra terms in Equation (4.15), due to quadratic electro-optic effects in the quantum well structure. The analysis is done here for an optical

wavelength of 1.3 μm, quantum effects will occur for wavelengths lower than the wavelength corresponding to the lowest transition energy in the quantum structure. In particular they modify the optical absorption, and hence the refractive index, of the QW structure, through the Kramers-Kronig relationship. Taking quantum effects into account, the refractive index will vary between that of GaAs and that of AlAs with the actual value depending on the composition and thickness of each layer. Consequently, all quantum well structures can be considered here to be equivalent to a particular structure with different layer composition and thickness, for which quantum effects have been ignored.

Although the integrals contained in Equation (4.15) have indefinite limits, there is no loss of accuracy in truncating the integrals and performing them numerically over some finite limit. In the case of the SAW induced field profiles, the majority of the acoustic energy extends to roughly one acoustic wavelength (as shown in the results of chapter 2), and the guided optical mode amplitudes decay rapidly into the substrate after the core/substrate interface is passed. For this reason the integrals were performed to a depth of 2 acoustic wavelengths. The range of SAW frequencies considered here goes from 100 MHz to 2 GHz which includes the typical range of device operating frequencies. The SAW velocity for these structures varies between that of bulk GaAs (2864 ms^{-1}) and that of bulk AlAs (3008 ms^{-1}), which corresponds to a SAW wavelength range of roughly 30μm to 1.5μm.

The results are presented for single layer waveguides, to illustrate the effects of the main compositional parameters of interest in conventional structures, as the results here aid in the understanding of more complicated structures. Results are also presented for hypothetical quantum well structures of 40 quantum wells within the guiding region, with well thicknesses of 80Å and barrier thicknesses of 120Å. Variations of acoustic power, acoustic aperture, Aluminium content in the barrier layers and linear grading of the barrier layer refractive index profile across the waveguide are looked at.

The data for the analysis is taken from Adachi[17], Landolt-Börnstein[18], and INSPEC publications[19],[20] and is shown in Table 4.1 (next page), linear interpolation was used where the appropriate values for binary and ternary alloys were not available.

	GaAs	AlAs	Si	Ge
Refractive index, n	3.41	2.91	3.5	4.3
Density , ρ (kgm^{-3})	5360	3760	2330	5323
Stiffness, ($Nm^{-2}\times10^{10}$)				
c_{11}	11.88	12.02	16.56	12.85
c_{12}	5.38	5.70	6.39	4.92
c_{44}	5.94	5.89	7.95	6.68
Elasto-optic constants				
p_{11}	-0.165	-0.040	-0.094	-0.068
p_{12}	-0.140	-0.035	0.017	-0.054
p_{44}	-0.072	-0.072	-0.051	-0.074
Electro-optic constant ($mV^{-1}10^{-12}$)				
r_{14}	-1.46	-1.25	—	—
Piezoelectric constant (Cm^{-2})				
e_{14}	-0.154	-0.225	—	—

Table 4.1 Material parameters used for the analysis.

4.3.2 Results and discussions

All plots of diffraction efficiency shown here can be described by essentially two features ; the maximum value of diffraction efficiency and where it is situated in the frequency spectrum. Referring to Equations (4.13) and (4.14) it can be seen that the diffraction efficiency is critically dependent on the overlap between the diffracted and undiffracted modes and the SAW induced field quantities.

To illustrate the importance of the acousto-optic overlap in the determination of diffraction efficiency, consider Figure 4.2, this shows the guided modes (diffracted and undiffracted) for a MQW structure of 40 quantum wells in the guiding region with 30% Aluminium fraction in 120Å barriers and GaAs wells of 80Å, together with an electric field profile at three different SAW frequencies. The trends of the graph also apply to the acoustic strain fields as they too

exist within essentially one acoustic wavelength of the surface. At low frequency (100 MHz) the electric field extends deep into the structure, far beyond the range of the guided mode, and this fact together with the low amplitude reduces the overlap and the corresponding diffraction efficiency. At a frequency in the middle of the range considered (1 GHz), the electric field's penetration has decreased and it's amplitude increased, increasing the overlap and the diffraction efficiency. The maximum diffraction efficiency will generally occur when the penetration of the SAW matches the range of the guided mode. At the highest frequency shown in Figure 4.2 (2 GHz), the diffraction efficiency will be very close to it's maximum value. Intuitively then, a broad guided mode will in general put some limit on the high frequency performance of the interaction. It is important to realise though that this type of constraint does not necessarily have to be imposed on the width of the waveguide core, as will be shown later when multi-layer structures are considered.

4.3.2.1 Single layer waveguides

The results given here show the effects of guiding layer thickness, and waveguide composition in simple three layer planar optical waveguides where air forms the upper cladding layer, the core of the waveguide is a GaAs layer and the lower cladding layer is $Al_xGa_{1-x}As$ with the whole structure on a GaAs substrate.

Figure 4.3 shows the variation of diffraction efficiency with SAW frequency for this type of waveguide with a range of guiding layer thicknesses. As the guiding width increases the frequency at which the penetration of the SAW comes to match that of the guided mode decreases (as previously explained) and since this frequency is lower, the amplitude of the induced fields are also lower for this assumed power flow. Thus the two characteristic points of the graph are explained ; i.e. the variation in diffraction efficiency amplitude and the variation in the position of the "roll-off" frequency.

Figure 4.4 shows the variation of diffraction efficiency with SAW frequency for this type of waveguide with a range of Aluminium fractions in the cladding layer. The Aluminium fraction has an effect on all the important parameters of the interaction: the guided mode is generally confined better with increasing Al fraction in cladding layers, thereby increasing the relevant overlap functions at the same acoustic frequencies and increasing the frequency at which roll-off occurs, the result is an increase in the acousto-optic diffraction efficiency. The

electro-optic and elasto-optic constants of an $Al_xGa_{1-x}As$ layer will decrease with increasing Al fraction (see Table 4.1) resulting in a smaller acousto-optic interaction, and depending on the relative sizes of the acoustic wavelength and the $Al_xGa_{1-x}As$ layers, the presence of a high Aluminium fraction will increase the SAW induced electric field in that region (as described in the results of chapter 2). Hence we expect opposing effects with increasing Aluminium fraction, and the dominant effect may change with acoustic frequency and Al fraction. Here, for the waveguide of Figure 4.4, the diffraction efficiency increases over the whole range of SAW frequencies looked at for decreasing Al fraction, suggesting that for this structure, the effect of the photo-elastic and electro-optic components is dictating the overall behaviour. Note there is also a slight decrease in the position of the peak diffraction efficiency with decreasing Al fraction together with a sharper roll off :- the optical mode penetrates further into the substrate with decreasing Al fraction.

4.3.2.2 Multi-layer waveguides

For multi-layer waveguides the compositional parameters of guiding region thickness and cladding layer Al fraction have an analogous effect to that of the single layer waveguide case. However, the addition of further layers to the structure suggests the possibility of using more complicated refractive index profiles and it is clearly then of interest to look at the acousto-optic diffraction efficiencies of such structures. Multi-layered structures with layer dimensions of the order of QW sizes will be used to illustrate this.

4.3.2.3 Quantum well structures

Results are presented here for structures consisting of 40 quantum wells within the MQW guiding region.

The diffraction efficiency can be seen to increase with increasing acoustic power, as shown in Figure 4.5. The maximum value shown is around 75% for an acoustic power of 10mW. Ilyich *et al.*[21] reported diffraction efficiencies of around 50% (experimentally) for a SAW power of 23mW, a guiding region thickness of 0.7 μm, acoustic aperture of 1mm and an Al fraction of 0.1. Abdelrazek *et al.*[22] reported a diffraction efficiency of 38% with an acoustic power of 2.72mW, a guiding layer of 1 μm thickness and an acoustic aperture of 0.76mm. In reality the power applied to the transducer will not be the same as the power carried by

the SAW and for device operation the important transducer parameters must also be considered such as it's frequency response, and issues of impedance matching etc.

The variation of diffraction efficiency with acoustic aperture for the same structure, with an acoustic power of 5mW is shown in Figure 4.6. It can be seen that for this range of acoustic apertures, the diffraction efficiency is increasing with increasing acoustic aperture. Referring to Equation (4.13) it is apparent that the diffraction efficiency will have a sinusoidal dependence on the square of the transducer length, and this becomes clear if the transducer length is taken to values greater than those shown in Figure 4.6.

Figure 4.7 shows the variation of diffraction efficiency with composition of the $Al_xGa_{1-x}As$ barriers. It can be seen from Figure 4.7 that for this structure, increasing the Al fraction initially increases the diffraction efficiency, suggesting that the effect on the guided modes is dominant, and the fact that the increased diffraction efficiency occurs at the high end of the frequency scale, also suggests this conclusion. As the Al fraction is increased beyond 0.2, the diffraction efficiency drops over the full SAW frequency range, suggesting the effect on the elasto-optic constants is dominant.

Figure 4.8 shows the variation of diffraction efficiency with gradient of the linearly graded refractive index profile in the guiding region. A gradient of zero corresponds to an Al fraction of 10% in all the barrier layers of the guiding region. A gradient of 1 corresponds to an Al fraction of 10% in the uppermost barrier and 80% in the lowermost barrier, with linear interpolation in between. As the gradient is increased the guided mode profile is pushed towards the surface of the waveguide[23] (as illustrated in chapter 3), in general increasing the relevant overlap functions and increasing the frequency at which the roll-off occurs. However the opposing effect of decreasing material parameters is again evident since as the gradient increases, the Aluminium content of the structure is also increasing. Of importance here is the fact that if we compare Figure 4.8 with Figure 4.7 it is evident that for the *same* acoustic power, guiding region thickness and acoustic aperture, significant increases in acousto-optic diffraction efficiency can be achieved in the higher end of the SAW frequency range by grading the refractive profile of the structure through variations of composition in individual layers.

4.3.3 *Intermodulation distortion and non-linear effects*

The dynamic range of many acousto-optic signal processing systems is limited by the intermodulation products[24,25] (IMPs) generated by the Bragg cell. The IMPs arise from two distinct sources; multiple optical diffraction due to the presence of multiple tones simultaneously in the cell and optical diffraction from acoustic harmonic waves due to the non-linearity of the acousto-optic material. These two sources will produce unwanted frequencies within the Bragg cell which will interact with the fundamental frequency of the acoustic waves and also between themselves to produce the IMPs.

The standard characterisation of the spurious response of a Bragg cell restricts the input to two pure tone input frequencies (f_1 and f_2). Most combinations of these two tones fall outside the bandwidth of the cell. The strongest modes falling in the bandwidth of the cell are the two-tone third order intermodulation products, $2f_1$-f_2 and $2f_2$-f_1, and it is these that are considered for most analyses.

Throughout the 1980's much work was done on IMPs in *bulk* materials for specific acoustic modes (usually longitudinal). More recently, some authors have tried to estimate the effects of IMPs on the performance of acousto-optic devices[26], using mathematical models based on theories of non-linear acoustic wave motion. This has lead on to more complicated analyses of non-linear *surface* acoustic wave propagation[27,28] on top of generic anisotropic substrates, which in themselves have necessarily been considerable pieces of work. It is clear from these studies that a general non-linear SAW analysis of multi-layered structures that would result in determination of the IMPs is needed, and also that it is beyond the scope of the work presented here. For this reason any consideration of the IMPs has been neglected, however it must be noted that they are important for device design and operation, and it is because of the need to go to higher frequencies and larger bandwidths that this problem is worth looking at.

4.4 SILICON-GERMANIUM : a new acousto-optic material?

4.4.1 Introduction

SiGe is a useful material for optoelectronic applications as it's bandgap may be varied from Si to Ge, thereby enabling optical devices to generate, transmit and absorb light between 1.1 and 1.8 μm. In addition since SiGe is grown on Si substrates, it is an ideal candidate for integration with Si based electronic circuits. Many optical and electronic devices have been demonstrated in SiGe/Si structures[29], and advances in the study of SiGe/Si superlattices and quantum wells[30], and in the growth of SiGe structures[31] provide an impetus for the development of further devices. However, one factor which limits the development of SiGe-based optoelectronic devices and integrated circuits is the lack of active signal processing devices. As mentioned in chapter one, guided wave acousto-optic devices provide many different types of signal processing and analysis operations such as, spectral analysis[32], correlation[33] and deflection[2].

The acousto-optic behaviour of a material is assessed by a number of parameters known as 'acousto-optic figures of merit'[34] (as mentioned in chapter 1), and although Silicon has relatively low acousto-optic figures of merit[35], Germanium has significantly high acousto-optic figures of merit in comparison with many other commonly used materials[35] such as CdS, GaAs and As_2S_3, resulting from a high refractive index at the wavelengths of interest for optoelectronic applications. Consequently, since the acousto-optic effect is potentially useful for the realisation of active signal processing devices in SiGe structures, it is of interest to evaluate the acousto-optic interactions in SiGe/Si structures where the large acousto-optic figures of merit in high Germanium content layers may be exploited. If useful signal processing devices can be demonstrated in SiGe it will aid the development of optoelectronic integration in SiGe.

The theory used for the analysis of the SiGe waveguides is the same as that already mentioned in section 4.2, however it must be remembered that unlike III-V materials, Si and Ge are not piezoelectric as their crystal structures are centro-symmetric. Although this

crystal structure is disrupted in the formation of SiGe, suggesting the possibility of piezoelectric behaviour, here it is assumed that the SiGe layer is non-piezoelectric for all Ge concentrations. In this respect, in practice a piezoelectric surface layer such as ZnO would be needed to provide generation of the SAW. Since conservation of the non-piezoelectric behaviour in the SiGe alloy is effectively an assumption of continuing inversion symmetry, it is sensible to also assume non-electro-optic behaviour for the SiGe alloy.

The theory used here only considers the propagating SAW and does not consider either the generation or coupling of the SAW from the transducer into the SiGe/Si structure. The theory follows exactly that given in section 4.2 except that here there is no electro-optic effect contribution and no piezoelectrically induced electric field, resulting in an expression for the acousto-optic overlap of the form

$$\left|\Gamma_{mn}(f)\right|^2 = \frac{\left|\int_0^{\infty} U_m(y)U_n(y)\{p{:}S_a U_a(y)\}dy\right|^2}{\left|\int_{-\infty}^{+\infty} U_m^2(y)dy\right\|\int_{-\infty}^{+\infty} U_n^2(y)dy\Big|} \qquad \text{-(4.17)}$$

where the symbols represent the same quantities as those given in Equation (4.15) The results presented here are for the TE_0 mode of the SiGe waveguide and the coupling of these modes in the interaction region. i.e. no results are presented involving coupling between different modes or different polarisations.

A planar heterojunction waveguide structure was studied here and the interaction geometry was given by that shown in Figure 4.1. The SAW is assumed to propagate in the [110] direction on the {100} plane, i.e. the SAW propagation direction normally used for III-V materials.

The refractive indices of the SiGe layers were taken from Reference 20, and here, strain effects due to lattice mismatch have been ignored, as the structures studied have layer thicknesses that exceed the critical layer thicknesses below which strain is present[36]. However, for thicknesses greater than the critical layer thicknesses, the strain is

accommodated through relaxation of the structure, which results in the presence of crystal defects which may well affect the waveguide loss characteristics and produce scattering.

4.4.2 Diffraction efficiencies in single layer SiGe/Si waveguides

The SAW propagation analysis results in a solution that has particle displacements in the direction of propagation of the acoustic wave and normal to the surface of the structure. Associated with these are four components of strain whose variation with depth below the surface is used in the analysis of the acousto-optic interaction. In general, the waveguides modelled here are single optical mode structures although those with the highest refractive indices in the guiding region were found to support several modes.

The variation of diffraction efficiency with SAW frequency for several acoustic powers, in $Si_{0.9}Ge_{0.1}$ planar waveguide structures is shown in Figure 4.9. The penetration of the SAW into the substrate decreases with increasing acoustic frequency, and the acoustic energy is concentrated primarily within one acoustic wavelength of the surface. Increasing the SAW frequency initially increases the diffraction efficiency, as the overlap between the SAW induced strain fields and the TE_0 optical mode amplitude increases. However when the SAW frequency becomes sufficiently large, so that the acoustic wavelength becomes comparable in size to the width of the optical mode (approximately the width of the guiding region), then the diffraction efficiency begins to drop off and this effect increases thereafter with the SAW frequency, repeating again the same type of behaviour that was mentioned for the III-V structures.

The diffraction efficiencies shown here for the low acoustic powers are significantly less than those obtained for equivalent $Al_xGa_{1-x}As/GaAs$ structures[37] at the same acoustic powers and acoustic aperture, and in order to produce diffraction efficiencies of the same order of magnitude as those observed in $Al_xGa_{1-x}As/GaAs$, much more acoustic power is needed, making any prospective devices relatively inefficient.

Figure 4.10 shows the variation of diffraction efficiency with SAW frequency, for several Si_xGe_{1-x}/Si single layer planar waveguides with various Germanium fractions. It can be seen, as expected, that a high Ge content is desirable for efficient acousto-optic interaction, and can result in diffraction efficiencies of the same order of magnitude as equivalent $Al_xGa_{1-x}As$/GaAs structures, at the high end of the SAW frequency range.

The design of devices must take into account a number of other effects which are not included in this study. They include

(i) the propagation losses of the waveguide,

(ii) scattering of the optical mode into other modes by the SAW induced grating,

(iii) increasing the efficiency of the SAW generation and coupling efficiency of SAW into the SiGe layer by the use of highly piezoelectric layers such as ZnO, and

(iv) non-linear response of the material to SAW induced effects which can lead to intermodulation distortion as described in section 4.3.3

In terms of practical devices, the crystal structure of the layers will significantly modify the optical propagation characteristics of the waveguide as defects produced in the SiGe grown layer will act as scattering centres, thereby increasing the waveguide propagation loss. In particular, for Ge concentrations below ~10% the SiGe layer will be strained and the propagation loss will be low, typically < 1dBcm^{-1} at a wavelength of 1.523 μm[38], while for Ge concentrations greater than ~10% the layer is completely relaxed and the SiGe layer contains a high density of dislocations[38] which increase the waveguide loss significantly to values between ~5dBcm^{-1} at a wavelength of 1.523μm. For Ge concentrations of 10%, the SiGe/Si heterostructure contains a 0.5μm-thick highly dislocated layer at the SiGe-Si interface which increases the waveguide loss to 1dBcm^{-1} at a wavelength of 1.523μm[39]. The effect of these crystal defects on the strength of the acousto-optic effect is not known, although their reduction of the intensity of the propagating beam will clearly reduce the

intensity of the diffracted beam and such increased waveguide losses are clearly detrimental to the useful operation of the device.

4.5 SUMMARY

The interaction between SAWs and guided optical waves in planar single and multi-layer AlGaAs/GaAs optical waveguides has been studied using a numerical determination of the diffraction efficiency as a function of SAW frequency. Results show that acoustic powers of the order of 5-10mW are needed to produce reasonable diffraction efficiencies. The Aluminium content of the structures is responsible for a combination of qualitatively different parameters which it is suggested produce opposing effects whose significance will vary with the acoustic frequency. Results also suggest that linear grading of the barrier refractive index profiles can significantly increase the diffraction efficiency and raise the diffraction maximum to a higher frequency, through increased confinement of the optical mode and therefore increased overlap with the SAW induced fields.

The interaction between SAWs and guided optical waves in planar $Si_{1-x}Ge_x/Si$ heterojunction waveguides has been analysed and the diffraction efficiency plotted as a function of SAW frequency. For low Germanium concentrations it was found that large acoustic powers are needed to produce useful diffraction efficiencies. It has been shown that the diffraction efficiency and SAW frequency may be optimised by varying the Ge concentration of the guiding layer to produce high efficiency devices in SiGe planar optical waveguide structures.

References

[1] Kissa, K. Wang. X. Ih, C.S. and Hunsperger, R.G. "Novel Integrated-Optic Modulator for Optical Communications," Technical Digest of the OSA Opticon '88 Symposium, Santa Clara, CA, p. MK3, 30 Oct.-4 Nov., (1988)

[2] Gass, P. and Shambles, J.R. "Angle-frequency relationship for a practical acousto-optic deflector," Opt. Lett., **18**, pp.1376-1378, (1993)

[3] Valette, S., Lizet, J., Mottier, P. *et al.* "Integrated optical spectrum analyser using planar technology on oxidised silicon substrate," Electron. Lett., **19**, (21), pp.883-885, (1983)

[4] Jain, F.C. and Bhattacharjee, K.K. "Multiple quantum well optical modulator structures using surface acoustic wave induced Stark effect," IEEE Phot. Technol. Lett. **1**, pp.307-309, (1989)

[5] Gryba, T. and Lvebvre, J. "Optimisation of MQW structures for acousto-optic absorption modulators," IEE Proc. Optoelectron., **141**, pp.62-64, (1994)

[6] Yariv, A. "Coupled mode theory for guided wave optics," IEEE J. Quantum. Electron, **QE-9**, pp.919-933, (1973)

[7] Haus, H.A. and Huang, W. "Coupled-Mode Theory," Proc. IEEE, **79**, pp.1505-1517, (1991)

[8] C S Tsai (Ed.) *Guided wave acousto-optics, Interactions, devices and applications* p.121, Springer series in Electronics and Photonics Vol. 23, Springer, Berlin New York, (1990)

[9] Nye, J.F. Physical *Properties of crystals*, Oxford University Press, (1957)

[10] Dixon, R.W. "The photoelastic properties of selected materials and their relevance to acoustic light modulators and scanners," J. Appl. Phys., **38**, pp.5149-5153, (1967)

[11] Y.Ohmachi, "Acousto-optic light diffraction in thin films," J.Appl.Phys., **44**, pp.3928-3932, (1973)

[12] Tsai, C.S., Alhaider, M.A., Nguyen, L.T. and Kim, B. "Wide-Band Guided-Wave Acoustooptic Bragg Diffraction and Devices Using Multiple Tilted Surface Acoustic Waves," Proc. IEEE, **64**, pp.318-328, (1976)

[13] Bumman, K, and Tsai, C.S. "High-Performance Guided-Wave Acousto-optic Scanning Devices Using Multiple Surface Acoustic Waves," Proc. IEEE, **64**. pp.788-793, (1976)

[14] Auld, B.A. *Acoustic fields and waves in solids*, Vol. 1. Wiley, New York, (1973)

[15] Y.Kim and W.D.Hunt "Acoustic fields and velocities for surface-acoustic-wave propagation in multilayered structures: an extension of the Laguerre polynomial technique," J. Appl. Phys., **68,** (10), pp.4993-4997, (1990)

[16] Hiroshima, T. "Electric field induced refractive index changes in GaAs-$Al_xGa_{1-x}As$ quantum wells," Appl. Phys. Lett., **50**, pp.968-970, (1987)

[17] Adachi, S. "GaAs, AlAs and $Al_xGa_{1-x}As$: material parameters for use in research and device applications," J. Appl. Phys., **58**, pp.R1-R29, (1985)

[18] Landolt-Börnstein, *Numerical Data and Functional Relationships in Science and Technology*, III/2: "Elastic, piezoelectric and related constants of crystals,", Ed. K. H. Hellwege, Springer-Verlag Berlin (1982)

[19] Adachi, S. (Ed.) Properties of Aluminium Gallium Arsenide, INSPEC, Datareview series No.7, IEE (1993)

[20] Kasper, E. (Ed) *Properties of strained and relaxed Silicon Germanium*, INSPEC Datareview series No.12, IEE., (1995)

[21] Ilyich, A., Kikkarin, S.M., Petrov, D.V., Tsarev, A.V. and Yakovkin, I.B., "A comparison of acousto-optic interaction in $LiNbO_3$ and GaAlAs waveguides," Opt. Commun., **56**, pp.161-166, (1985)

[22] Abdelrazek, Y. and Tsai, C.S. "High performance acoustooptic Bragg cells in ZnO-GaAs waveguide at GHz frequencies" Optoelectronics-Devices and technologies, **4**, pp.33-37, (1989)

[23] Thompson, C. and Weiss, B.L. "Modal characteristics of graded multilayer optical waveguides," J. Lightwave Technol., **14**, pp.894-900, (1996)

[24] Elston, G. "Intermodulation products in acousto-optic signal processing systems," Proc. Ultrasonics Symp., pp.391-397, (1985)

[25] Pape, D.R., "Acousto-optic Bragg cell intermodulation products," Proc. Ultrasonics Symp., pp.387-391, (1986)

[26] Elston, G. and Kellman, P. "The effects of acoustic nonlinearities in acousto-optic signal processing systems," Proc. Ultrasonics Symp., pp.449-453, (1983)

[27] Tupholme, G.E. and Harvey, A.P., "Nonlinear surface acoustic waves on a piezoelectric solid," Int. J. Engng. Sci., **26**, pp.1161-1168, (1988).

[28] Harvey, A.P. and Tupholme, G.E., "Propagation of anisotropic elastic and piezoelectric nonlinear surface acoustic waves," Wave Motion, **16**, pp.125-135, (1992)

[29] Wang, K.L. and Karunasiri, R.P.G., "SiGe/Si Electronics and optoelectronics," J. Vac. Sci. Technol. B, **11**, pp.1159-1167, (1993)

[30] Karunasiri, R.P.G. and Wang, K.L. "Quantum devices using SiGe/Si heterostructures" J. Vac. Sci. Technol. B, **9**, pp.2064-2071, (1991)

[31] Kasper, K. "Growth and properties of Si/SiGe superlattices," Surface Sci., **174**, pp.630-639, (1986)

[32] Abdelrazek, Y. and Tsai, C.S. "An integrated optic RF spectrum analyser in a ZnO-GaAs-AlGaAs waveguide," J. Lightwave Technol., **8**, pp.1833-1837, (1990)

[33] Casserent, D. "General time-, space-, and frequency-multiplexed acousto-optic correlator," Appl. Opt., **24**, pp.2884-2888, (1985)

[34] Pinnow, D. "Guide lines for selection of acousto-optic materials," IEEE J. Quantum. Electron., **QE-6**, pp.223-238, (1970)

[35] Abrams, R.L. and Pinnow, D.A. "Acousto-optic properties of crystalline Germanium," J. Appl. Phys., **41,** pp.2765-2768, (1970)

[36] O'Reilly, E.P. "Valence band engineering in strained-layer structures," J. Vac. Sci. Technol., **4**, pp.121-127, (1989)

[37] Armenise, M.N., Matteo, A.M. and Passaro, V.M.N. "Modelling of acoustooptic interaction in multilayer guiding structures," Proc. SPIE, **1583**, pp.289-297, (1991)

[38] Yang, Z., Weiss, B.L., Shao, G. and Namavar, F. "The effects of Ge concentration on the propagation characteristics of SiGe/Si heterojuntion waveguides," J. Appl. Phys., **77**, pp.2254-2257, (1995)

[39] Weiss, B.L., Yang, Z., and Namavar, F. "Wavelength dependent propagation loss characteristics of SiGe/Si planar waveguides," Electron. Lett., **28**, pp.2218-2220, (1992)

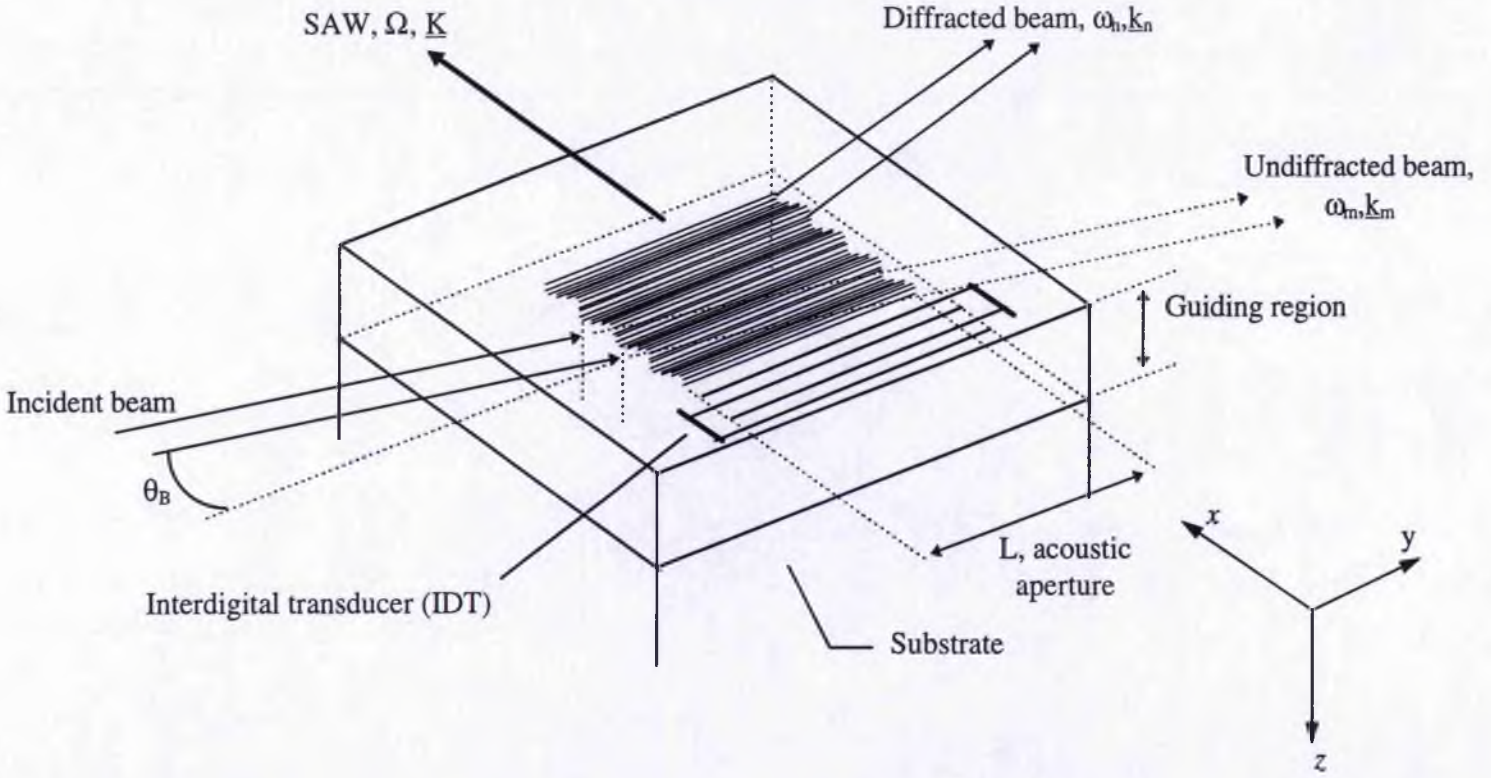

Figure 4.1 *Schematic diagram of the interaction between guided optical modes and surface acoustic waves in planar waveguides. Although not shown here, the guiding region can consist of multiple layers for this analysis. The SAW propagates with angular frequency Ω and momentum vector* $\underline{K}$.

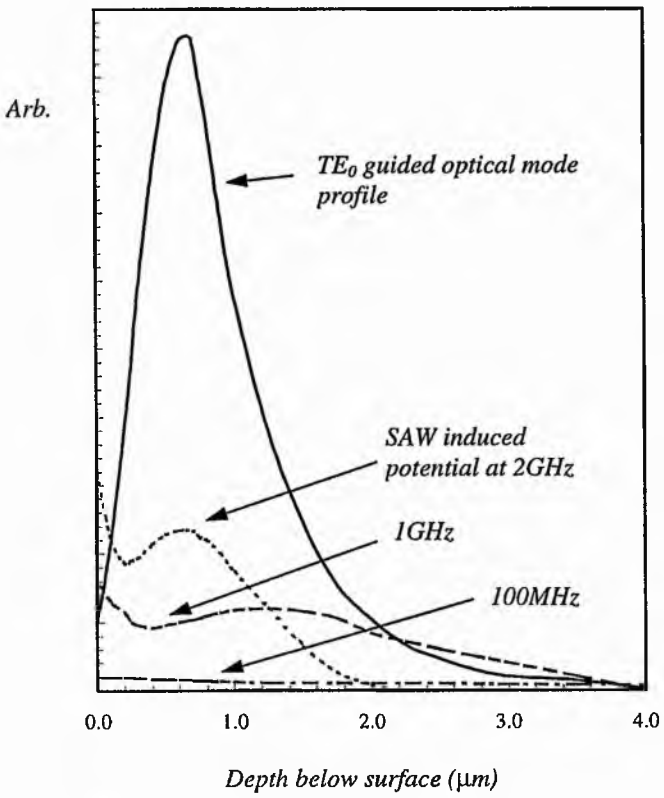

Figure 4.2 *Example of overlap between guided optical mode profile and SAW induced fields for different SAW frequencies.*

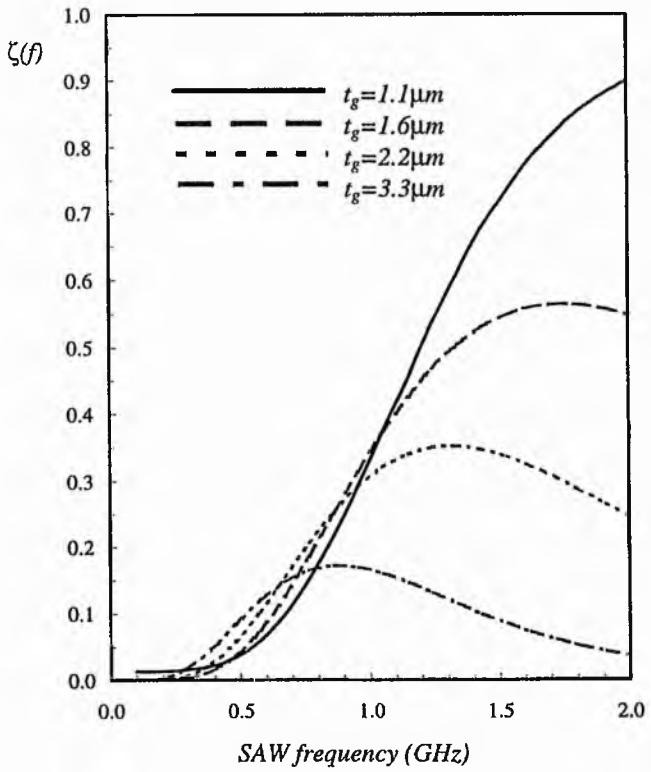

Figure 4.3 *Variation of acousto-optic diffraction efficiency ζ(f) with SAW frequency for different guiding region thicknesses, (t_g) for single guiding layer AlAs/GaAs waveguide structure.*
Acoustic power=5mW
Acoustic aperture (L) = 2mm.

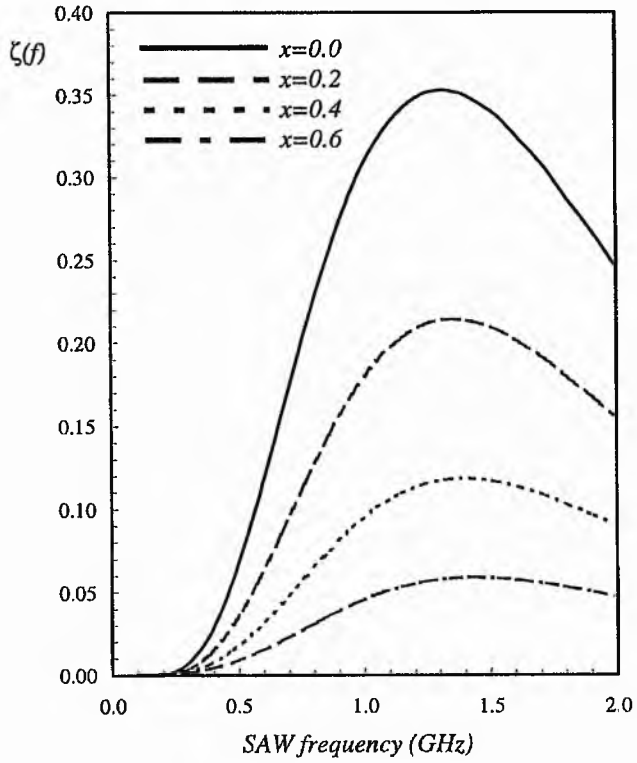

Figure 4.4 *Variation of acousto-optic diffraction efficiency ζ(f) with SAW frequency for different cladding layer Aluminium fractions, (x) for single guiding layer AlGaAs/GaAs waveguide structure.*
Acoustic aperture (L) =2mm
Guiding layer thickness = 2.2μm
Acoustic power = 5mW

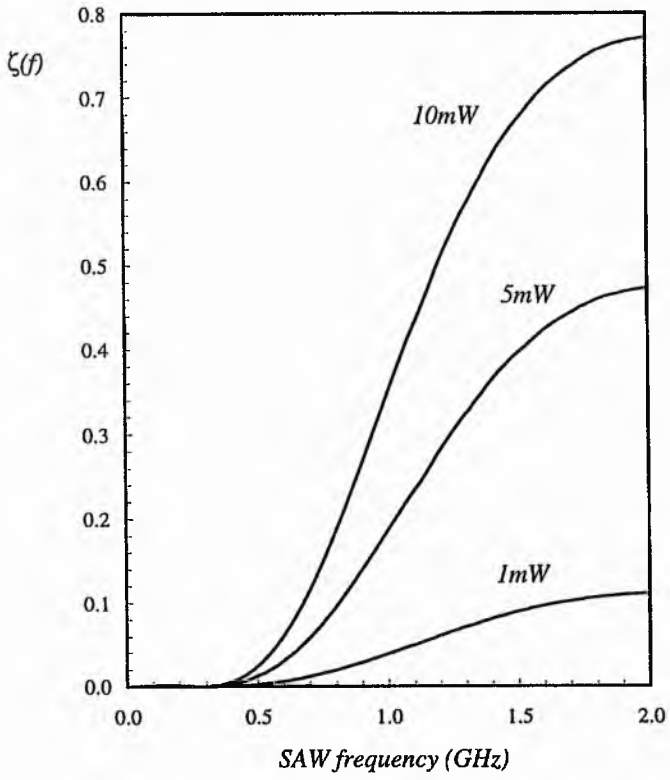

Figure 4.5 *Variation of diffraction efficiency ζ(f), with SAW frequency for acoustic powers of 1mW, 5mW and 10mW. Structure consists of upper layer of 0.4 μm $Al_{0.4}Ga_{0.6}As$ on MQW region of $Al_{0.2}Ga_{0.8}As/GaAs$, L_z=80Å , L_b=120 Å, on bottom layer of $Al_{0.4}Ga_{0.6}As$.*
Acoustic aperture = 2mm

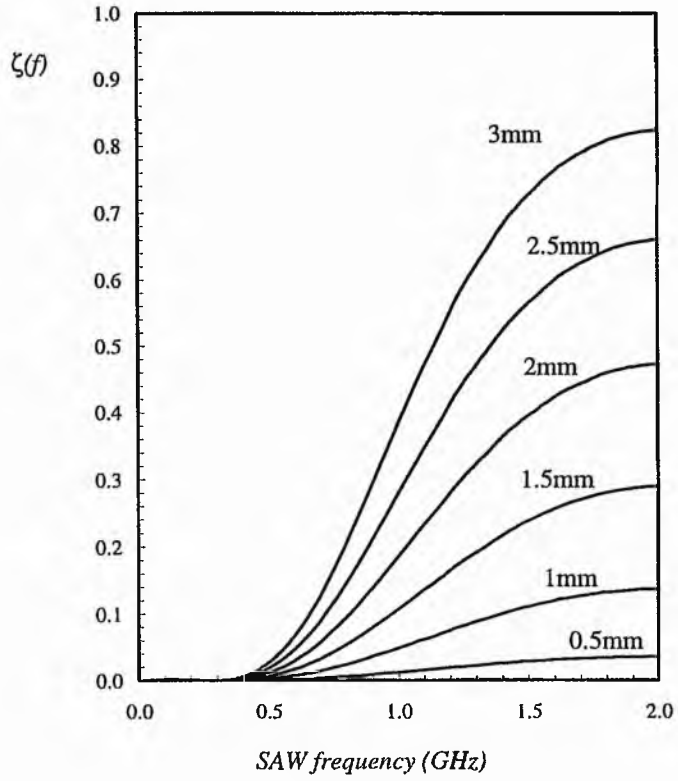

Figure 4.6 *Variation of diffraction efficiency ζ(f), with SAW frequency for acoustic apertures of 0.5 to 3mm. Structure consists of upper layer of 0.4 μm $Al_{0.4}Ga_{0.6}As$ on MQW region of 40 quantum wells of $Al_{0.2}Ga_{0.8}As/GaAs$, L_z=80Å , L_b=120 Å, on bottom layer of $Al_{0.4}Ga_{0.6}As$.*
Acoustic power = 5mW

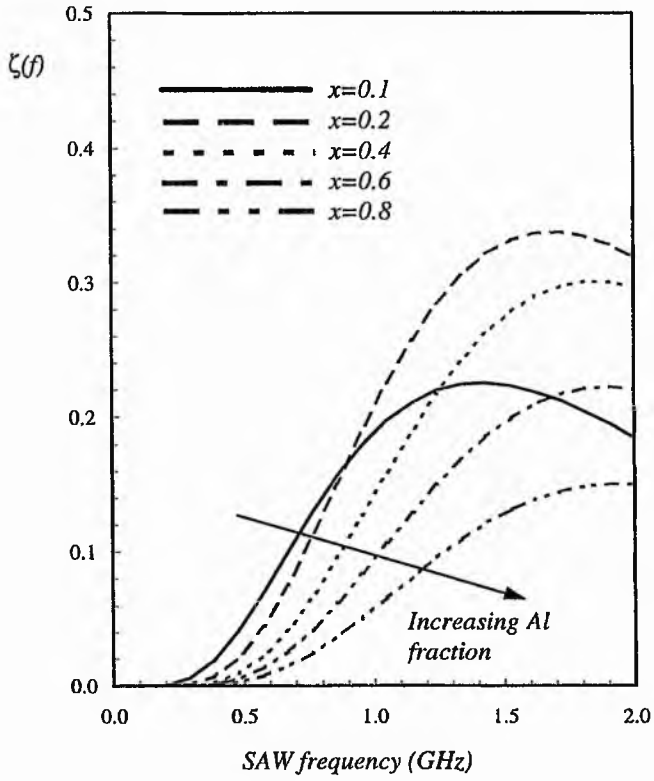

Figure 4.7 *Variation of diffraction efficiency ζ(f), with SAW frequency for a range of Al fractions (x) in the barriers of a MQW structure. Structure consists of upper layer of 0.4 μm $Al_{0.4}Ga_{0.6}As$ on MQW region of $Al_{0.2}Ga_{0.8}As/GaAs$, L_z=80Å , L_b=120 Å, on bottom layer of $Al_{0.4}Ga_{0.6}As$.*
Acoustic aperture L=2mm, acoustic power = 5mW.

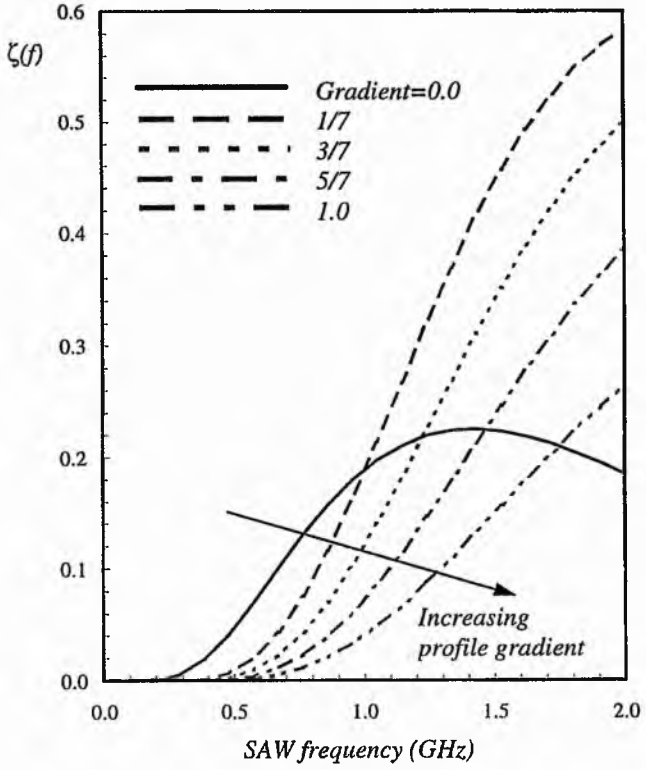

Figure 4.8 *Variation of diffraction efficiency ζ(f), with SAW frequency for a range of refractive index profile gradients in the barriers of a MQW structure. Structure consists of upper layer of 0.4 μm $Al_{0.4}Ga_{0.6}As$ on MQW region of $Al_xGa_{1-x}As/GaAs$, L_z=80Å , L_b=120 Å, on bottom layer of $Al_xGa_{1-x}As$*
Acoustic aperture L=2mm, acoustic power = 5mW.

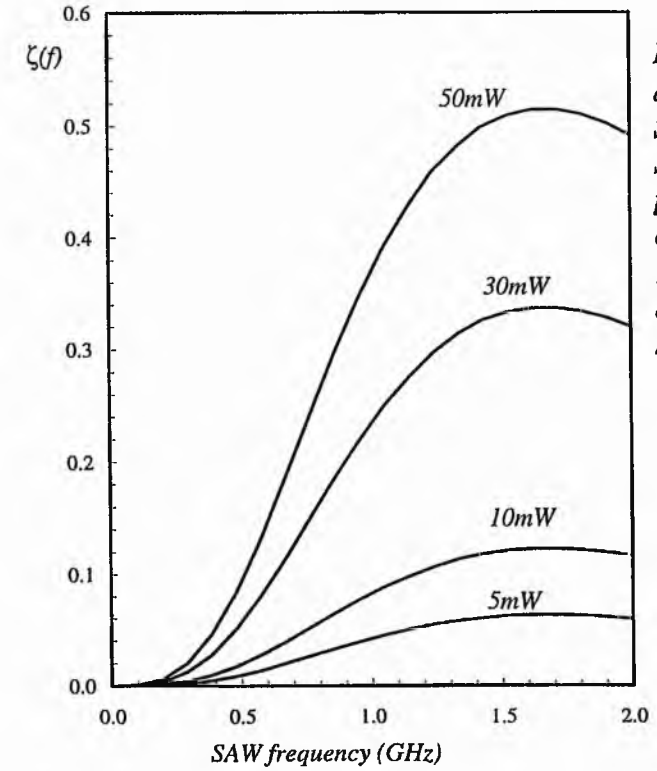

Figure 4.9 *Variation of diffraction efficiency ζ(f), with SAW frequency for a range of SAW powers in a SiGe/Si planar waveguide. Structure consists of upper layer of 1.5μm of $Si_{0.9}Ge_{0.1}$ on substrate of Si.*
Acoustic aperture L=2mm.

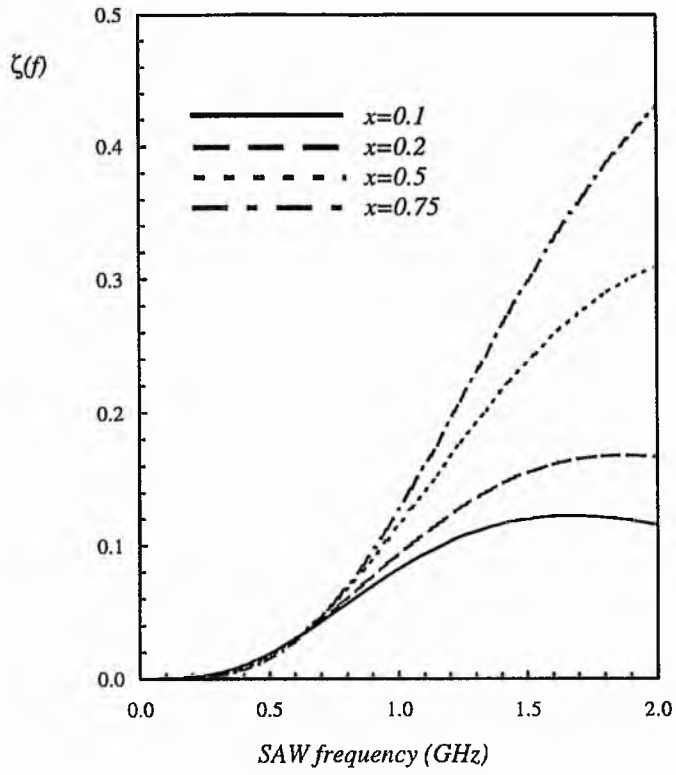

Figure 4.10 *Variation of diffraction efficiency ζ(f), with SAW frequency for a range of Germanium fractions in a SiGe/Si planar waveguide. Structure consists of upper layer of 1.5μm of $Si_{1-x}Ge_x$ on substrate of Si.*
Acoustic aperture L=2mm.
Acoustic power = 5mW

Chapter 5

The Effect of Surface Acoustic Waves on the Properties of Quantum Well Structures

The subject of quantum well structures was introduced in chapter 1, and their enhanced electro-absorptive and electro-optic properties were discussed. Since the field magnitudes employed in the operation of devices that utilise these properties are of the order of the SAW induced fields in such structures (as shown in chapter 2), we expect that refractive index changes induced by SAWs in quantum well structures should provide further possibilities for extending the range and performance of acousto-optic devices.

5.1 INTRODUCTION

A simple study of SAW effects on single and multiple quantum well structures will be presented here. The electron and hole energy eigenvalues and envelope functions of the unperturbed structure are determined. The effect of the acoustically induced strain and electric fields on the confining potential of the quantum well structure is then calculated and the energy eigenvalues and envelope functions for this perturbed case are determined. The complex refractive index of the structure is then calculated for both the perturbed and unperturbed cases, to give the change in refractive index and the absorption coefficient as a

function of SAW wavelength, amplitude, barrier composition, well width and number of wells. The wavelength and power of the SAW were found to be important in setting the induced changes in the refractive index.

Surface acoustic waves have been used for a range of electronic signal processing applications[1], some of which were mentioned in chapter 1. With the continual need for greater device efficiency, larger signal processing power and higher degrees of optoelectronic integration, acousto-optic devices are interesting for the development of efficient, wide bandwidth Bragg diffraction devices in quantum well structures such as AlGaAs/GaAs[2].

In bulk materials the propagation of SAWs produces a periodic ripple on the sample surface which acts as a diffraction grating and may be used for modulation, diffraction and filtering of optical beams. In III-V semiconductor QW structures, which have piezoelectric properties, the propagating SAW induces strain (for specific propagation directions) which induces an electric field (as discussed in chapter 2) which modifies the QW optical properties in addition to the surface ripple.

With current semiconductor growth techniques such as MBE and MOCVD, the growth of multi-layer and multiple quantum well (MQW) structures is well established, and useful devices which rely on the enhanced electro-optic and electro-absorptive properties of QW structures have been demonstrated[3,4]. The effects of strain and linear electric fields on the properties of quantum well structures are well documented[5,6], and for certain crystallographic growth orientations, strain induced piezoelectric fields have been predicted[7] and demonstrated in AlGaAs/GaAs strained QW structures and may be of use for device operation[8].

As has been mentioned in chapter 1, SAWs are very useful for the realisation of adaptive signal processing devices as the signal is concentrated at the surface and hence is readily accessible, have low power requirements and operate most readily in the 10 MHz to over 1 GHz frequency range. It is of interest to characterise/model the effect of SAWs on the

optical properties of QW structures, as a first step to device design. To this end a number of devices have already been proposed[9,10].

In this chapter the results of calculations of the effect of SAWs on the change of the optical properties of single and multiple AlGaAs/GaAs QW structures are presented. More specifically, the refractive index changes due to the deformation of envelope wave functions in QW structures due to a SAW propagating on the sample surface are presented. Excitonic effects, which are greatest (centred) around the bandedge wavelength of the structure, on the changes in refractive index and absorption have not been included here as electro-optic devices are unlikely to be operated around the fundamental bandedge. Electro-optic quantum well modulators operate at wavelengths of low electro-absorption which are somewhat longer than the bandedge wavelength.

The propagation of SAWs on GaAs and other III-V materials has been studied using simple analytical techniques for bulk materials[11] and by matrix methods involving field matching at the interfaces for multi-layer structures[12]. Here the Laguerre polynomial[13] method was used (as described in chapter 2) to determine the strain and induced piezoelectric fields for arbitrary layer thickness and composition of the $Al_xGa_{1-x}As$ barrier layers. The confined state energies and envelope functions of the electrons and holes and the "allowed" transitions in the QW structure are determined, with and without the additional perturbation of the SAW. Then the absorption coefficient and refractive index variation in the QW structure are calculated from the dipole moments formed between the electron and holes.

5.2 THEORY

The refractive index of a material is a macroscopic property of that material. However, in the study of the physics of semiconductor materials, a microscopic approach must be taken to look in more detail at the contributions to both the electronic and optical properties of the material. This entails a quantum mechanical approach to the constituent electrons and atomic nuclei, and also to the interaction of light with the various manifestations of electro-magnetic oscillators within the material.

5.2.1 Wave functions and energy eigenvalues

5.2.1.1 Bulk Materials

Any crystal, regardless of whether it contains a quantum well structure or not, is made up of a large number of interacting particles. As a result of this, any attempt to determine the energy levels and wave functions of a solid cannot realistically be successful without a number of simplifying assumptions.

If the adiabatic approximation[14] is used to separate the dynamics of the electrons and atomic nuclei, together with the one electron approximation[15], and if the potential experienced by the electron is approximated by an effective periodic potential V_0, then the problem can be reduced to solving the time-independent Schrödinger equation

$$\left[\frac{\hat{p}^2}{2m_0}+V_0\right]\left|\phi_{nk}\right\rangle=\varepsilon_{nk}\left|\phi_{nk}\right\rangle \qquad \text{-(5.1)}$$

where m_0 is the mass of the free electron, n is the band index and k is the electron wave vector. The $|\phi_{nk}\rangle$ represent the electronic energy eigenstates. Translational symmetry in the lattice dictates that the energy eigenfunctions obey the Bloch theorem

$$\left\langle \mathbf{r}+\mathbf{R}\middle|\phi_{nk}\right\rangle=e^{i\mathbf{k}.\mathbf{R}}\left\langle \mathbf{r}\middle|\phi_{nk}\right\rangle \qquad \text{-(5.2)}$$

where **R** represents a lattice vector. This leads to the eigenvalue equation for the lattice periodic part of the wave function;

$$\left(\frac{\hat{p}^2}{2m_0}+V_0+\frac{\hbar}{m_0}\mathbf{k}.\mathbf{p}\right)\left|n\mathbf{k}\right\rangle=\left(\varepsilon_{nk}-\frac{\hbar^2k^2}{2m_0}\right)\left|n\mathbf{k}\right\rangle \qquad \text{-(5.3)}$$

The calculation of the full extent of the band structure resulting from these equations is a complicated numerical problem, however **k.p** perturbation theory provides a short cut to

calculating small regions of band structure by treating the **k.p** term in Equation (5.3) as a small perturbation to the electronic behaviour in the vicinity of a given k, particularly $k=0$ which is the most relevant region of interest for optical transitions in III-V materials.

The conduction and valence band states at $k=0$ for III-V compounds such as GaAs are well documented[16]. Once these band energies and eigenstates are determined, **k.p** theory[17] allows one to compute the states in the vicinity of $k=0$ by expansion in terms of the $k=0$ eigenstates. The **k.p** term in Equation (5.3) is then treated perturbatively using the methods of time independent perturbation theory[18]. In the case of the non-degenerate states of the conduction band, it is a straight forward step to obtain the eigenstates and eigenvalues, and (to second order in the perturbation) the effect on the energy of the electron can be absorbed into the concept of effective mass.

The valence band states are treated again using the time independent perturbation theory but applied here to degenerate bands since for III-V materials the $k=0$ states for the two lowest valence bands are degenerate. The appropriate state vectors to be used in the approach are a general linear combination of the basis of state vectors that spans the degenerate sub-space. Perturbation theory is then applied and after including spin-orbit coupling the Hamiltonian for the hole states takes the form of the *Luttinger Hamiltonian*[19] :-

$$\mathcal{H} = \begin{pmatrix} \mathcal{H}_{hh} & -c & -b & 0 \\ -c^{*} & \mathcal{H}_{lh} & 0 & b \\ -b^{*} & 0 & \mathcal{H}_{lh} & -c \\ 0 & b^{*} & -c^{*} & \mathcal{H}_{hh} \end{pmatrix} \qquad \text{-(5.4)}$$

where,

$$\mathcal{H}_{hh} = \frac{\hbar^2 k_z^2}{2m_0}(\lambda_1 - 2\lambda_2) + \frac{\hbar^2 (k_x^2 + k_y^2)}{2m_0}(\lambda_1 + \lambda_2)$$

$$\mathcal{H}_{lh} = \frac{\hbar^2 k_z^2}{2m_0}(\lambda_1 + 2\lambda_2) + \frac{\hbar^2 (k_x^2 + k_y^2)}{2m_0}(\lambda_1 - \lambda_2)$$

$$c = \frac{\sqrt{3}\hbar^2}{2m_0}\left[\lambda_2 (k_x^2 - k_y^2) - 2i\lambda_3 k_x k_y\right]$$

$$b = \frac{\sqrt{3}\hbar^2}{m_0}\left[\lambda_3 k_z (k_x - ik_y)\right]$$

and the three Luttinger parameters, λ_1, λ_2 and λ_3 are determined experimentally and listed in many books including Landolt-Börnstein[20]. For III-V semiconductors, in the vicinity of $k=0$ the axial approximation[21] is commonly introduced which results in the assumption of isotropic band structure within the k_x, k_y plane and allows the Luttinger Hamiltonian to be easily diagonalised[22].

5.2.1.2 Quantum confinement

In the case of quantum well structures, the time independent Schrödinger equation (Equation (5.1)) becomes

$$\left[\frac{\hat{p}^2}{2m_0} + V_0 + V_{con}\right]\left|\phi_\lambda{}^{QW}\right\rangle = \varepsilon_{nk}\left|\phi_\lambda{}^{QW}\right\rangle \qquad -(5.5)$$

where V_{con} is the potential due to the epitaxially grown quantum well structure and λ represents the set of quantum numbers used to identify a particular state.

The *envelope function approximation*[23] is adopted here, where the confining potential V_{con} is assumed to vary sufficiently little within a unit cell. This assumption leads to a separation of the wave functions into a part that varies at the scale of the ionic potential and a part that varies in a much slower manner that is known as the envelope function. Perturbation theory can again be used for both degenerate and non-degenerate bands. For the case of the conduction band, separation of variables leads to equations for both the motion in the direction perpendicular to the well and also in the plane of the well. The envelope functions obey a one-dimensional Schrödinger like equation describing the motion perpendicular to the well. The effects of quantum confinement are much more interesting for bands that are degenerate at $k=0$, for the top two valence bands in III-V materials second-order degenerate perturbation theory yields coupled differential equations whose solutions can again be expressed as products of one-dimensional quantum well functions with two dimensional (in the plane of the QW) free-particle functions. It is found that the states with the heavier effective mass in the z direction also have the lighter effective mass in the transverse

direction. This is termed *mass reversal*, and the convention is to use the masses in the z direction as a criteria for labelling *light* and *heavy* holes.

5.2.1.3 Acoustic perturbation

The passage of an acoustic wave over the top of the quantum well structure will modify the potential experienced by the electron, through the strain, and for specific propagation directions of interest, also through the induced electric field.

The propagation of a SAW on the surface of a semiconductor structure contributes a *time dependent* perturbation to the one-electron energy levels and wave functions of the QW structure. Typical SAW propagation velocities on AlGaAs/GaAs multi-layer structures are ~3000 m/s [24], as mentioned in chapter 2. Since the focus of the work here is on the influence of the SAW on the optical properties of the QW structure, it was deemed appropriate as a first approximation to treat the SAW as a stationary wave. In addition, since the SAW wavelength is typically >1μm, the oscillatory nature of the SAW has a slower spatial variation than that of the quantum well confining potential. Consequently it is appropriate to express the problem within the envelope function approximation. The quantum well subband edge states at the Γ-Valley can be calculated within the envelope function approximation, using a Ben-Daniel and Duke model[25], resulting in a 1-dimensional Schrödinger like equation:

$$\frac{-\hbar^2}{2}\frac{d}{dz}\left[\frac{1}{m^*(z)}\frac{d}{dz}+V(z)\right]\psi_n(z)=\varepsilon_n\psi_n(z) \qquad \text{-(5.6)}$$

which is solved for the electron and hole energy levels and envelope wave functions. Here z represents the growth direction, i.e. normal to the plane of the quantum wells, $V(z)$ is the confining potential, $m^*(z)$ is the effective mass of either electrons or holes, $U_n(z)$ represents the *envelope* wave function of either an electron or hole, corresponding to the n'th confined subband energy level, ε_n. A SAW propagating on the surface of an AlGaAs/GaAs QW structure in the [110] direction on the {100} plane induces both a depth dependent strain and a piezoelectric field[26]. Both of these effects contribute additional terms to the shape of the confining potential $V(z)$, experienced by the electrons and holes. In the case of the electric

field, the additional term in $V(z)$ is taken from the electric potential ϕ_{SAW} corresponding to the SAW induced piezoelectric field and which by using the Laguerre polynomial method is given by the following expansion:

$$\phi_{SAW} = \sum_{l=0}^{l=\infty} r_l |l(z)\rangle \exp(ix) \qquad \text{-(5.7)}$$

where l labels the l'th Laguerre polynomial and in reality the summation can be truncated to a finite number of terms without any significant loss of accuracy, e.g. if the series is truncated to $l = 5$, further terms are found to contribute less than ~0.01% to the final summation, and $|l(z)\rangle$ is given by:

$$|l(z)\rangle = \frac{\exp[-(z/2)]L_l(z)}{l!} \qquad \text{-(5.8)}$$

where $L_l(z)$ is the l'th Laguerre polynomial, the definition of which is taken from Aizenstadt *et al*[27].

The strain induced by the SAW also affects the shape of the QW potential. Adachi[28] gives the strain Hamiltonian at $k=0$ in the zinc blende type crystal, which is derived from the theory of Pikus and Bir[29]. Strains of the order of a few % can have large and important effects on the electronic band structure of semiconducting materials[30] and are commonly used in device operation. In SAW generated piezoelectric fields, the strains are significantly less than 0.01%, and therefore are not thought large enough to produce bandgap changes that will significantly affect the confining potential in QW structures. In addition it was found that if the strain Hamiltonian terms were calculated and added to the potential of Equation (5.6) then no significant alteration to the potential experienced by the electron was found. For this reason the SAW induced strain has not been included in the calculations, resulting in a treatment involving only the SAW induced electric field.

5.2.2 *Absorption coefficients and refractive indices*

Once the electron and hole envelope wave functions and the energy levels of the quantum well structure have been determined, the absorption coefficient and refractive index of the structure can be calculated. A semiclassical approach is taken in which the semiconductor structure is described quantum mechanically and the electromagnetic field is described classically. Time dependent perturbation theory applied to such a composite system gives, to first order, Fermi's golden rule[18] ;

$$\Gamma_{i\to f} = \frac{2\pi}{\hbar}\left|\left\langle E_f^{(0)}\left|\hat{H}_I\right|E_i^{(0)}\right\rangle\right|^2 \delta(E_f^{(0)} - E_i^{(0)} - \hbar\omega) \qquad \text{-(5.9)}$$

which represents the probability per unit time, Γ, for a transition to occur from the initial state E_i to final state E_f, where the transition is induced by the perturbing applied field, here represented by the interaction Hamiltonian H_I. Here δ represents the Dirac delta function, the superscript 0 corresponds to eigenvalues in the absence of a perturbation and ω is the frequency of the external perturbing potential (in this case the electromagnetic field). The electric dipole approximation is used for this type of theory, where the optical wavelength is assumed large enough to allow the spatial variation of the electromagnetic polarisation vector over the system of interest to be neglected. The interaction Hamiltonian H_I then takes on the form,

$$\hat{H}_I = \varepsilon.\hat{r} \qquad \text{-(5.10)}$$

where is ε the polarisation vector of the electromagnetic wave and $\boldsymbol{r}$ is the linear operator representing position.

The complex refractive index of a quantum well structure is derived from density matrix theory[31] and the real and imaginary parts can be expressed as[32]:

$$n_{re} = \frac{\mu_{cv}}{2n_b\varepsilon_0\pi\hbar^2 l_z} \times \sum_{lm} \int_{\bar{E}}^{\infty} \left\langle R_{ch}^2(E_0) \right\rangle \frac{(f_c - f_v)(\hbar\omega - E_{ch})}{(\hbar\omega - E_{ch}) + (\hbar/\tau)^2} dE_{ch} \qquad \text{-(5.11)}$$

and

$$n_{im} = \frac{-\mu_{cv}}{2n_b\varepsilon_0\pi\hbar^2 l_z} \times \sum_{lm} \int_{\bar{E}}^{\infty} \left\langle R_{ch}^2(E_0) \right\rangle \frac{(f_c - f_v)(\hbar/\tau)}{(\hbar\omega - E_{ch}) + (\hbar/\tau)^2} dE_{ch} \qquad \text{-(5.12)}$$

where l_z is the well thickness, μ_{cv} is the reduced electron-hole effective mass, E_{cl} is the electron confined energy level of the l'th electron measured from the bottom of the conduction band and E_{vm} is the equivalent for holes measured from the top of the valence band. E_g is the bulk bandgap energy and f_c and f_v are the Fermi functions for the electrons in the conduction band and in the valence band respectively. The lower limit of the integral is equal to $E_{cl}+E_{vm}+E_g$, which is the transition energy for an electron in the l^{th} state and a hole in the m^{th} state. n_b is the refractive index of the quantum well structure without electron-hole pairs and τ is the intraband relaxation time. $\langle R^2_{ch}(E_o)\rangle_{lm}$ is the mean square of the dipole moment formed by an electron in subband l and a hole in subband m. The light hole band has been neglected in the solution of Equations (5.11) and (5.12) since the density of states of this band is much smaller than that of the heavy hole band[32].

The matrix element of the dipole moment formed between an electron in the conduction band and a heavy hole in the valence band is given by:

$$R_{ch} = \left\langle \Psi_c k_{c\perp} \middle| er \middle| \Psi_c k_{c\perp} \right\rangle \qquad \text{-(5.13)}$$

where the subscripts c and h denote the conduction band and the heavy-hole bands respectively, $k_{c\perp}$ and $k_{h\perp}$ are the wave vectors of electron and hole in the plane of the QW structure. The wave functions here are expressed in the envelope function approximation and as such

$$\left|\Psi_{cn} k_{c\perp}\right\rangle = \left|\psi_{cn}\right\rangle \left|u_{ck}(n)\right\rangle e^{jk_{c\perp} r_\perp} \qquad \text{-(5.14)}$$

where $|\psi_{cn}\rangle$ corresponds to the slowly varying envelope function, $\psi_n(z)$ of Equation (5.6) and $|u_{ck}(n)\rangle$ corresponds to the periodic part of the Bloch function and as such possesses the periodicity of the lattice potential. The calculation of the mean square of the dipole moment follows the approach given in detail in References 31 and 32. Here we have included the overlap between electron and hole envelope functions unlike previous analyses where a perturbative approach was taken and an approximate orthonormal relation between the envelope functions of the unperturbed structure could be assumed, here no such restriction is placed on the envelope functions since the perturbed wave functions are obtained explicitly through a finite difference method and are not in the form of a linear combination of the unperturbed wave functions.

5.3 SURFACE ACOUSTIC WAVE PROPAGATION ON DEVICE STRUCTURES

5.3.1 Procedure

The structures looked at in the work presented here consist of single and multiple AlGaAs/GaAs quantum well structures. Where for the case of an MQW structure it is assumed here that the barriers between wells are always large enough to treat each well as separate. In that respect the determination of the energy levels and envelope functions is done sequentially for each well of the structure. In the case of superlattice structures, where the separation between wells is small enough to allow coupling between wells, then the whole structure must be treated as one. The method described here can cope with the analysis of superlattice structures in principle, however it must be remembered that the superlattice has an effective band structure produced through the coupling and subsequent mutual perturbation between the quantum wells of the structure. The effective band structure is brought about through the virtually insignificant difference in energy between the different eigenvalue solutions corresponding to a particular quantum number in the structure. The efficiency of the bisection method used to find these eigenvalues is then severely

compromised by this close spacing of solutions, and another technique or more powerful computing would be needed to determine the complete set of solutions for any given superlattice. For this reason only single and multiple QW structures are looked at in the work presented here.

The co-ordinate system used here is shown in Figure 5.1 When the SAW propagates across the surface in the *y* direction, a piezoelectric field is set up that has an oscillatory dependence in the propagation direction of the SAW and an exponentially decaying depth dependence, $\underline{E}(z)$. Assuming the static approximation we, consider the effect of the electric field on the confining potential at a specific *y* value in the structure. Figure 5.2 illustrates the effect of the piezoelectric field on the confining potential of an MQW structure. For large acoustic wavelengths, i.e. >10μm, the deviation of the SAW induced electric potential from that of a linear profile is negligible giving rise to a constant electric field across the MQW structure. As the acoustic wavelength is decreased the non-linearities in the SAW induced potential become more significant, this effect can be seen in Figure 5.2 with an acoustic wavelength of 2μm. In this sense, we expect any differences between the case of a constant electric field applied across an MQW structure and a SAW induced field, to increase with decreasing acoustic wavelength.

The one dimensional Schrödinger like equations for the electron and hole envelope functions (Equation (5.6)) were solved using a finite difference grid. The problem was re-expressed as a dimensionless "Sturm-Liouville"[33] problem to produce a tridiagonal matrix. The eigenvalues of the tridiagonal matrix were found by solving the determinantal equation using a recursive relation[34] and a bisection method. Inverse iteration[35] was then used to improve the eigenvalue accuracy and find the eigenvectors, which represent the envelope functions.

Equations (5.11) and (5.12) were solved numerically using a Romberg integration method[36] employing an extended midpoint rule to perform the integrals.

It must be noted that the effects of tunnelling are ignored in this analysis, and that the model only uses the "confined" states for the refractive index calculations. The criteria taken here for defining what constitutes being "confined" is that there is a greater than 50% probability

of finding the electron/hole inside the quantum well. In reality it is likely that the SAW induced potential could produce regions outside of the QW that are particularly favourable to electron/hole occupation. Hence, proper consideration of tunnelling effects together with possible practical ways of minimising it would have to be undertaken when looking at specific device operation in more detail.

The effects of SAW wavelength, SAW amplitude, barrier composition, well width, and number of wells on the SAW induced modification to the complex refractive index of relevant structures were investigated. Well widths in the range 30Å to 130Å were considered together with barrier compositions in the range x=35% to 75% (x is the Aluminium fraction), acoustic wavelengths in the range 1.5μm to 20μm, and acoustic powers in the range 1 to 100mW. MQW structures consisting of 2, 5 and 10 quantum wells were also studied, and it must be noted that this is well below the number of quantum wells used in typical MQW device structures, however the nature of the results obtained suggests an applicability to all types of MQW structures.

The procedure undertaken for any particular structure is to

(i) Determine the electron and heavy hole confined energy levels and envelope functions in the absence of a perturbing SAW.

(ii) Using the same method, produce equivalent data for the same structure with the addition of a perturbing SAW.

(iii) Using the data from (i) and (ii), calculate the change in the complex refractive index of the structure.

The parameters used for the analysis are shown in Table 5.1 (next page) and are taken from References 20 and 28. T is the temperature (here assumed to be 300K) and x is the Aluminium fraction.

Parameter	Value
Conduction/valence band offset ratio (Qc:Qv)	0.66
Energy gap, Eg (eV)	$1.519+1.247x-0.005405T^2/(T+204)$ for $x< 0.45$ $1.519+1.247+(1.147(x-0.45)^2-0.0005405T^2/(T+210)$ for $x\geq 0.45$
Electron effective mass	0.0665+0.0835x
Heavy Hole effective mass	0.33+0.18x
Light Hole effective mass	0.09+0.09x

Table 5.1 Important parameters used for the analysis.

5.3.2 Results and discussions

5.3.2.1 Unperturbed quantum well structures

A typical example of the unperturbed energy eigenvalues and envelope functions for electrons and heavy and light holes in a single quantum well is shown in Figure 5.3. The structure here is a 90Å $Al_{0.35}Ga_{0.65}As/GaAs/Al_{0.35}Ga_{0.65}As$ quantum well. Note that as the relevant energy level moves up the well, the confinement of the electron/hole decreases and it's envelope function penetrates deeper into the barriers. The variation of the energy levels and envelope functions with well/barrier composition is well known and need not be discussed in detail here, suffice to say that as the well thickness decreases, the energy levels are shifted up the respective wells. As the barrier Aluminium fraction increases, the energy levels are shifted down the respective wells.

The energy levels and envelope functions for the electrons and holes in an MQW structure are shown in Figure 5.4, the structure consists of five quantum wells each with a well width of 60Å and barriers of 35% Aluminium content and 200Å thickness. It can be seen that in this case the envelope functions are well separated spatially and the structure can be approximated as an array of single quantum wells.

For the case of a superlattice the coupling between quantum wells leads to a qualitatively different type of behaviour for both the energy levels and envelope functions. The best way of discussing this is to consider what happens when a single quantum well is put in the vicinity of another. For a large separation between the two wells (e.g. ~100 Å) the structure would behave like an MQW structure with well separated envelope functions, and energy levels that are virtually identical for each well. As the separation between the wells decreases, the coupling between wells would cause a splitting of the quantum well energy levels analogous to the splitting of atomic energy levels when two identical atoms are put in close proximity. This behaviour can be treated perturbatively[37] in a manner similar to tight binding calculations in electronic states of crystals. The result is splitting of the energy levels by an amount that depends on the size of the perturbing potential and leads to symmetric and anti-symmetric combinations of the unperturbed envelope functions.

If further quantum wells are added to the structure, the resulting splitting of the energy levels leads to an effective energy band structure, again analogous to the energy bands of a crystal structure, and the appropriateness of the term s*uperlattice* becomes apparent.

5.3.2.2 Surface acoustic wave induced electric field effect

The electron-heavy hole interband transitions in the as-grown rectangular QW structures are shown in Table 5.2 for barrier Aluminium fractions of 35%, which show that only the e_1-h_1 and e_2-h_2 "allowed" transitions exist with any significant strength. The presence of a SAW induces both strain and electric fields, both of which have the potential to modify the optical properties of the QW structure. However, as has been mentioned, due to the very low level of the induced strains they have no significant effects while the strain induced piezoelectric field is much more significant.

The SAW induced piezoelectric field has two major effects on the potential profile of the QW; firstly the shape of the confining potential changes so that the well width over the height of the potential is not constant and secondly the minimum energy difference between the conduction and valence bands is reduced as a consequence of the tilting of the potential profile. The latter of the two effects is the dominant mechanism commonly used for band-edge electroabsorption mechanisms in quantum well structures and devices utilising constant

electric fields across the QW structure such as the Quantum-Confined Stark effect[38]. The perturbed profile has confined solutions that reside at a higher energy with respect to the minimum of their corresponding wells, in other words it is as if the well had been made thinner. The reduction in the e_1-hh_1 transition energy is due to the minimum energy difference reduction.

		No SAW		+SAW (λ=2μm)		+SAW (λ=4μm)		+SAW (λ=8μm)	
l_z (Å)	Transition	Energy (eV)	Overlap	Energy (eV)	Overlap	Energy (eV)	Overlap	Energy (eV)	Overlap
30	e_1hh_1	1.6250	0.9845	1.6247	0.9835	1.6249	0.9842	1.6250	0.9845
	e_1hh_2	1.7565	<1e-5	-					
60	e_1hh_1	1.5117	0.9919	1.5106	0.9809	1.51136	0.9886	1.5116	0.9910
	e_1hh_2	1.5686	0.0009	1.5684	0.1416	1.56855	0.0784	1.5686	0.0412
	e_1hh_3	1.6572	0.1118	-	-			1.6571	0.1123
	e_2hh_1	1.7165	0.0004	1.7157	0.1533	1.7163	0.0843	1.7164	0.0442
	e_2hh_2	1.7734	0.9610	1.7735	0.9425	1.7735	0.9555	1.7734	0.0159
	e_2hh_3	1.8620	0.0026	-	-		0.0896	1.8619	0.0196
90	e_1hh_1	1.4717	0.9950	1.4682	0.9301	1.47065	0.9739	1.4714	0.9890
	e_1hh_2	1.5016	0.0016	1.5012	0.3420	1.50146	0.1984	1.5015	0.1064
	e_1hh_3	1.5505	0.0792	1.5489	0.1145	1.5503	0.0901	1.5505	0.0823
	e_2hh_1	1.5894	0.0015	1.5871	0.3603	1.5887	0.2091	1.5892	0.1120
	e_2hh_2	1.6193	0.9830	1.6201	0.8852	1.6195	0.9519	1.6193	0.9742
	e_2hh_3	1.6682	0.0001	1.6697	0.2163	1.6684	0.1212	1.6683	0.0637
	e_3hh_1	1.7752	0.0937	-	-	1.8001	0.0745	1.7749	0.0884
	e_3hh_2	1.8050	0.0010	-	-	1.8309	0.1559	1.8051	0.0821
	e_3hh_3	1.8540	0.9272	-	-	1.8797	0.9074	1.8540	0.9220
110	e_1hh_1	1.4584	0.9962	1.4520	0.8492	1.4564	0.9434	1.4578	0.9808
	e_1hh_2	1.4795	0.0017	1.4789	0.4984	1.4795	0.3114	1.4795	0.1704
	e_1hh_3	1.5146	0.0677	1.5137	0.1575	1.5144	0.0962	1.5145	0.0756
	e_2hh_1	1.5448	0.0017	1.5405	0.5209	1.5434	0.3254	1.5444	0.1783
	e_2hh_2	1.5660	0.9876	1.5674	0.7587	1.5665	0.9090	1.5661	0.9651
	e_2hh_3	1.6010	0.0008	1.6023	0.3391	1.6014	0.1984	1.6011	0.1056
	e_3hh_1	1.6866	0.0791	1.6819	0.0532	1.6851	0.0325	1.6862	0.0656
	e_3hh_2	1.7078	0.0004	1.7088	0.4083	1.7082	0.2427	1.7079	0.1305
	e_3hh_3	1.7428	0.9652	1.7437	0.8329	1.7431	0.9241	1.7429	0.9538

Table 5.2 The electron-heavy hole transition energies and overlap integrals for a single quantum well with and without a perturbing SAW.

The effect on the transition energies due to the induced piezoelectric field show that the transition energies change by up to ~4meV due to the presence of the SAW. Here a SAW of wavelength 2μm and 10mW power is assumed. A quantitative measure of the strength of the transitions is provided by the overlap functions of electron and heavy hole envelope functions. The overlaps for the transitions in the as-grown rectangular QW structures show that only the e_1-hh_1, e_2-hh_2 and e_3-hh_3 "allowed" transitions exist with any significant strength. The changes in transition energy in going from the unperturbed to perturbed state

can clearly be seen and previously insignificant transitions become significant, e.g. the e_1-hh_2 transition. The lowest order transition (e_1-hh_1) is always shifted *down* in energy . However the results suggest that some of the higher order transitions are shifted to ***higher*** energies, e.g. the e_2-hh_2 transition in the 90Å quantum well. This suggests that for these higher order transitions, the effective narrowing of the well is dominating over the effect of narrowing of the minimum energy gap. The effect on the optical properties of these structures of these higher order transition shifts is not clear at the moment and further investigations need to be done. These SAW induced changes in the QW transitions result in changes in the absorption coefficient and refractive index which are discussed in the next section.

The overall behaviour of the transition energies with applied SAW has been re-produced with other acoustic wavelengths and powers. As an example the results for acoustic wavelengths of 4 and 8 microns are also included in Table 5.2. It was found that the shifts in transition energies diminish with increasing SAW wavelength (as the induced potential drops) and with decreasing SAW power.

5.3.2.3 Effect of surface acoustic waves on the refractive index of quantum well structures

The width of the quantum well has a significant effect on the energy of the confined states in the quantum well and as the well width increases the energy of the confined states in the well decreases while the number of confined states within the well also increases with well width. The same effects can also be obtained by keeping the well width constant and varying the depth of the quantum well by varying the composition of the barrier layer. As the energy levels move closer to the bottom of the well, the transition energies of the electrons and holes confined in the wells will correspond to longer optical wavelengths. The SAW acoustic wavelengths of interest are much larger than the well width, so that for a given acoustic wave **perturbation**, the induced strain modifies the transition in the QW thereby modifying both the absorption and refractive index of the structure.

The peak change in the refractive index due to the presence of the SAW is shown to shift to longer optical wavelengths with increasing well width. This effect is shown in Figure 5.5, where the spectral change in refractive index due to the presence of the SAW is plotted for

quantum well widths of 30Å, 60Å, 90Å, 110Å and 130Å with a SAW wavelength of 2μm and power of 10mW. These results show that the SAW causes a reduction of the real part of the refractive index of between 0.1 and 0.3% for optical wavelengths of greater than ~1 μm. The associated change in the absorption coefficient is shown in Figure 5.6. The steps in the absorption curve arise as this curve is comprised of the absorption coefficient of each allowed transition in the structure each of which have different transition energies and thus bandedge wavelengths. As the well width increases, the absorption curve moves to longer optical wavelengths, since the ground state transition energy is reduced.. Of significance is the fact that the absorption above an optical wavelength of around 1μm is negligible, suggesting that devices that rely solely on changes in real part of refractive index could operate effectively in this region as significant changes occur in this region as shown in Figure 5.5.

The effect of Al composition of the QW barrier layers on the variation of the refractive index, see Figure 5.7, are not as significant as those due to well width variations. Figure 5.7 is for Al compositions of 35%, 55% and 75%, a well width of 90 Å, a SAW wavelength of 2μm and an acoustic power of 10mW. Increasing the Al fraction increases the depth of the confining potential barriers in the QW structure, and the energies of the electron and hole confined states move away from the bottom of their respective potential wells. This process increases the transition energies and is reflected in the e_1-hh_1 transition peak shifts shown in Figure 5.7. The Al fraction also affects the size of the SAW induced potential due to the variation of the piezoelectric constant with Al fraction[28] and the SAW induced electric field increases with increasing Al content accordingly. It would be expected that this process would increase the refractive index shifts with Al content, which would be in opposition to the effect of the increased confinement. It is thought that this could explain at least qualitatively why the SAW induced refractive index variations shown in Figure 5.7 do not seem to be particularly sensitive to Al content.

The acoustic wavelength determines the rate of decay of the SAW induced electric field into the structure. Consequently, assuming a constant power flow that is independent of the acoustic wavelength, the amplitude of the SAW induced potential at the surface of the structure will be constant and the gradient of the induced potential (i.e.the electric field) will

increase with decreasing acoustic wavelength, as shown in Figure 5.8. The increased SAW induced electric field in the quantum well produces larger shifts in transition energies and hence increases in the refractive index of the structure, see Figure 5.9. The maximum change in refractive index occurs for the smallest acoustic wavelength, with values of around -0.15% for a SAW wavelength of 2μm and optical wavelengths of greater than ~1μm for which the corresponding optical absorption is very low and has not changed. For a SAW velocity of ~3000 ms^{-1} this corresponds to an acoustic frequency of 1.5GHz which is near the upper frequency limit for practical SAW devices.

Increasing the acoustic power increases the magnitude of the SAW induced potential at the surface of the structure. For a constant acoustic wavelength the gradient of the SAW induced potential is expected to increase, resulting in a larger electric field within the quantum well region, as shown in Figure 5.10. In a similar manner to the effect of the acoustic wavelength, this increases the changes in refractive index due to the SAW, increasing to ~-0.4% at the wavelength region above the band edge wavelength for 50mW acoustic power, see Figure 5.11.

The addition of more quantum wells to the structure to make an MQW structure has one major difference to the results shown above for single quantum well structures. Since it is directly due to the non-linearity of the SAW induced potential, it is unlikely to be seen in structures employing a constant electric field across the structure. The depth dependence of the SAW induced potential is inherently non-linear and the corresponding electric field is essentially the gradient of the potential variation, each quantum well in the MQW layer will experience a different perturbing electric field, depending on its depth and the penetration of the SAW. For a structure with 5 quantum wells, it can be seen that the gradient of the confining potential varies between quantum wells when the SAW is turned on, see Figure 5.2. This suggests that *variations in the change* of refractive index across the structure are expected for multiple quantum wells, which is confirmed in the results. These variations in the shift of refractive index increase slightly with increasing well width but the major variation is due to the acoustic wavelength, see Figures 5.12 and 5.13, which give results for two and five quantum wells respectively. Each quantum well that is added to the structure experiences a different SAW induced electric field, which leads to a broadening of the optical

effect as the number of quantum wells is increased. The quantum well that is nearest to the surface experiences the highest perturbing electric field, hence for example in Figure 5.12 the upper curve of each pair corresponds to the quantum well that is closest to the surface. Keeping the acoustic wavelength as high as possible will minimise this effect, however it must be noted that this would also decrease the observable refractive index change.

5.4 SUMMARY

A simple analysis of the effect of the propagation of SAWs on QW and MQW structures has been performed. Expressed within the envelope function approximation, the method allows the determination of the electron/hole energy eigenvalues and envelope functions in the presence of a perturbing SAW.

The results presented above show that the dominant effect of the SAW on the optical properties of the QW structure is the SAW induced piezoelectric field which shifts the transition energies by up to 4meV for an acoustic wavelength of 2μm and acoustic power of 10mW. These field induced changes allow some of the previously "forbidden" transitions to become "allowed". These changes in the subband structure of the QW structure result in significant changes in the absorption coefficient and refractive index of the structure.

The SAW induced changes in the absorption coefficient and refractive index of the structure are determined by the SAW frequency and the thickness and composition of the individual layers in the MQW structure. The SAW induced refractive index changes are both negative and are much more sensitive to the well width than the Al fraction in the barriers. The absorption coefficient of the structure shows the same trend. The SAW induced electric field increases with reducing SAW wavelength which results in large positive changes in the refractive index, with the changes being larger just above the band edge wavelength of the material. Similarly, increasing the SAW acoustic power results in negative increases in the change of refractive index which again are greater near the band edge wavelength. Increasing the number of quantum wells from two to five increases the maximum negative

change in refractive index. All of these effects do not take into account the effects of excitons which will modify the characteristics around the bandedge.

References

[1] Ananasso, F. "Review of SAW devices and their signal processing applications in space communications", International Journal of Satellite Communications, **7**, pp.235-261, (1989).

[2] Abdelrazek, Y. and Tsai, C.S. "High performance acousto-optic Bragg cells in ZnO-GaAs waveguide at GHz frequencies", Optoelectronics Devices and Technologies, **4**, pp.33-37, (1989).

[3] Miller, D.A.B. Chemla, D.S. Damen, T.C. Gossard, A.C. Weigmann, W. Wood, T.H. and Burrus, C.A. "Novel hybrid optically bistable switch: the quantum well self-electro-optic-effect device," Appl. Phys. Lett., **45**, pp.13-15, (1984)

[4] Wood, T.H. "Multiple quantum well (MQW) waveguide modulators", J. Lightwave Technol., **6**, pp.743-757, (1988)

[5] O'Reilly, E.P. "Valence band engineering in strained-layer structures", Semiconductor Science and Technology, **4**, pp.121-137, (1989)

[6] Kan, Y. Nagai, H. and Yamanashi, M. "Field effects on the refractive index and absorption coefficient in AlGaAs quantum well structures and their feasibility for Electrooptic device applications", IEEE J. Quantum Electron., **QE-23**, pp.2167-2179, (1987).

[7] Smith, D.L. and Mailhiot, C. "Piezoelectric effects in strained-layer superlattices," J. Appl. Phys., **63**, pp.2717-2719, (1988)

[8] Pabla, A.S. Sanchez-Rojas, J.L. Woodhead, J. Grey, R. David, J.P.R. Rees, G.J. Pate, M..A. Robson, P.N. Hogg, R.A. Fisher, T.A. Wilcox, A.R.K. Whittaker, D.M. Skolnick, M.S. and Mowbray, D.J. "Tailoring of internal fields in InGaAs/GaAs multi-well structures grown on (111)B GaAs", Appl. Phys. Lett., **63**, pp.752-754, (1993)

[9] Jain, F.C. and Bhattacharjee, K.K. "Recent developments in multiple quantum well acousto-optic and electro-optic modulator structures", Proceedings of the IEEE Utrasonic Symposium, pp.429-536, (1991)

[10] Gryba, T. and Lefebvre, J.E. "Optimisation of MQW structures for acousto-optic absorption modulators", Proceedings of the IEEE Optoelectronics, **141**, pp.62-64, (1994)

[11] Bright, V.M. Kim, Y. and Hunt, W.D. "Study of surface acoustic waves on the {110} plane of gallium arsenide" J. Appl. Phys., **71**, pp.597-605 (1992)

[12] Armenise, M.N. Passaro, V.M.N and Impagnatiello, F. "Acoustic mode analysis of a homogenous multilayer guiding structure", J. Opt. Soc. Am B, **8**, pp.443-446 (1991)

[13] S. Datta, B.J. Hunsinger, "Analysis of surface waves using orthogonal functions" J. Appl. Phys., **49**, pp.475-479, (1978)

[14] See for example, Ridley B.K. *Quantum processes in semiconductors* 3rd edition, Oxford Science Publications (1993)

[15] Bassani, F. and Parravicini, G.P. *Electronic states and optical transitions in solids*, page 69, Pergamon press (1975)

[16] Chow, W.W. Koch, S.W. and Sargent, M. III, *Semiconductor laser physics*, page 180, Springer-Verlag (1994)

[17] See for example, page 75 in Kane, E.O. *Semiconductors and Semimetals*, Edited by R.K. Wilardson and A.C. Beer, Academic, New York, (1966)

[18] Schiff, L.I. *Quantum mechanics*, Chapter 8, 3rd edition, McGraw-Hill, (1968)

[19] Luttinger, J.M. and Kohn, W. "Motion of electrons and holes in perturbed periodic fields," Phys. Rev. **97**, pp.869-883, (1955)

[20] *Landölt-Börnstein Numerical Data and Functional Relationships in Science and Technology*, Ed. O. Madelung, Group III, Vol. 17, Springer, Berlin, (1982)

[21] See for example, Altarelli, M. *Heterojunctions and Semiconductor Superlattices*, Eds. G. Allan, G. Bastard, N. Boccara, M. Lannoo and M. Voos, Springer Verlag, Berlin, (1985)

[22] Broido, D.A. and Sham, L.J. "Effective mass of holes at GaAs-AlGaAs heterojunctions," Phys. Rev. **B31**, pp.888-892, (1985)

[23] Bastard, G. and Brum, J.A. "Electronic states in semiconductor heterostructures," IEEE J. Quantum Electron. **QE-22**, pp.1625-1644, (1986)

[24] Kikkarin, M.M. Petrov, D.V. and Yakovkin, I.B. "Surface acoustic waves in GaAsAs/GaAs structures" Russian Ultrason., **17**, pp.113-118, (1987)

[25] BenDaniel, D.J. and Duke, C.B., "Space-charge effects on electron tunnelling", Phys. Rev., **152**, pp.683-692 (1966)

[26] Thompson, C. and Weiss, B.L. "Characteristics of surface acoustic wave propagation in III-V semiconductor quantum well structures", J. Appl. Phys., **78**, pp.5002-5007, (1995)

[27] Aizenshtadt, V.S. and Krylov, V.I. "Tables of Laguerre polynomials and functions", Pergamon, New York (1973).

[28] Adachi, S. "GaAs, AlAs and AlGaAs: Material parameters for use in research and device applications," J. Appl. Phys. **58**, pp.R1-R29, (1985)

[29] Pikus, G.E. and Bir, G.L. "Effect of deformation on the energy spectrum and the electrical properties of imperfect germanium and silicon", Sov. Phys: Solid State, **1**, pp.136-138, (1959)

[30] Adams, A.R. and Dunstan, D.J. "Analysis and design of low-dimensional structures and devices using strain: I. Hydrostatic pressure effects" Semicond. Sci. Technol., **5**, pp.1194-1201 (1990)

[31] Asada, M. Kameyama, A. and Suematsu, Y. "Gain and intervalence band absorption in quantum well lasers", IEEE J.Quantum Electron., **QE-20**, pp.745-753, (1984)

[32] Yamamoto, H. Asada, M. and Suematsu, Y. "Theory of refractive index variation in quantum well structure and related intersectional optical switch", J. Lightwave Technol., **6**, pp.1831-1840 (1988)

[33] Ascher, V.M. Matheig, R.M.M. and Russell, R.D. *Numerical solutions of boundary value problems for ordinary differential equations*, page 478 Prentice Hall (1988).

[34] Acton, F.S. *Numerical methods that work*, Harper & Row, New York, London (1970).

[35] Press, W.H. Teukolsky, S.A. Vetterling, W.T. and Flannery, B.P. *NUMERICAL RECIPES IN C, The Art of Scientific Computing*, 2nd Edition, Page 493, Cambridge University Press (1994).

[36] See, for example page 140 in Reference 35

[37] Weisbuch, C. Vinter, B. *QUANTUM SEMICONDUCTOR STRUCTURES Fundamentals and Applications*, Page 27, Academic Press, (1991)

[38] Miller, D.A.B. Chemla, D.S. Damen, T.C. Gossard, A.C. Wiegmann, W. Wood, T.H. and Burrus, C.A. "Band-Edge Electroabsorption in Quantum well structures: The Quantum-Confined Stark Effect," Phys. Rev. Lett. **53**, pp.2173-2176, (1984)

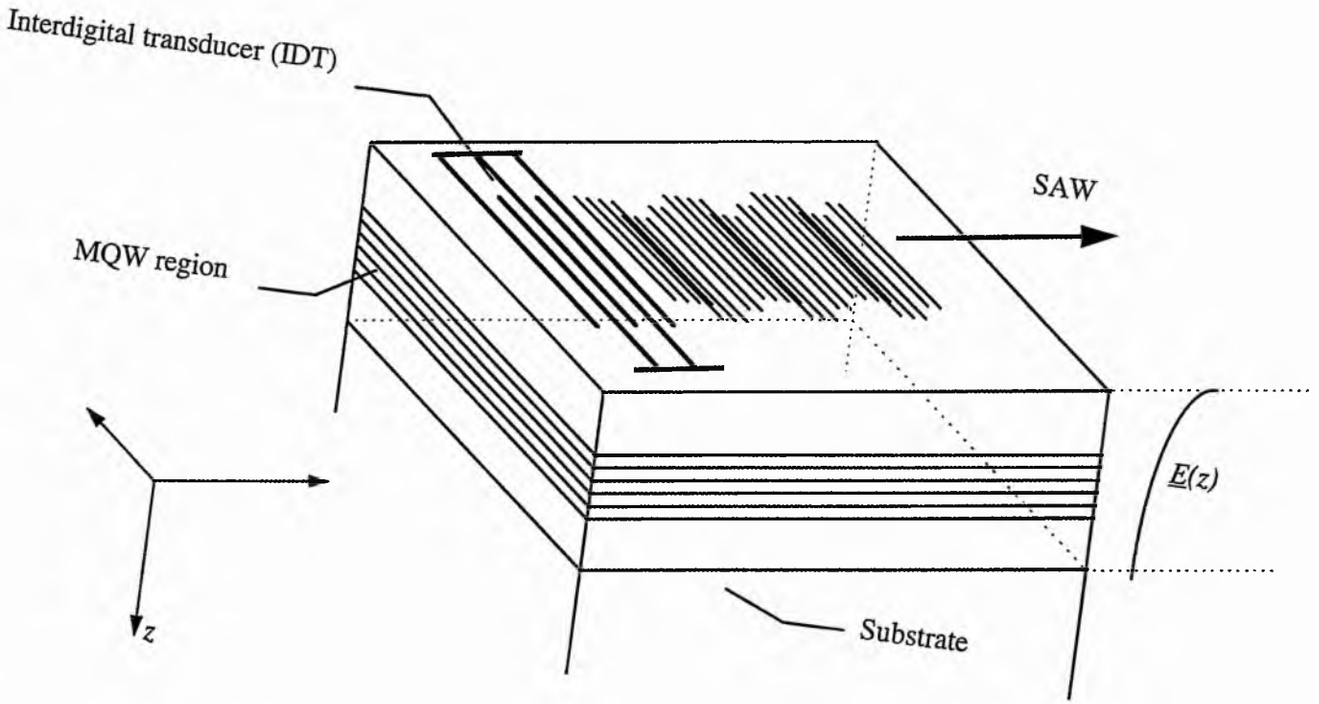

Figure 5.1 *Schematic diagram of the propagation of a SAW on top of a multiple quantum well (MQW) structure together with the co-ordinate system adopted for the modelling.* $\underline{E}(z)$ *is the SAW induced piezoelectric field amplitude, where z is the direction normal to the plane of the quantum wells.*

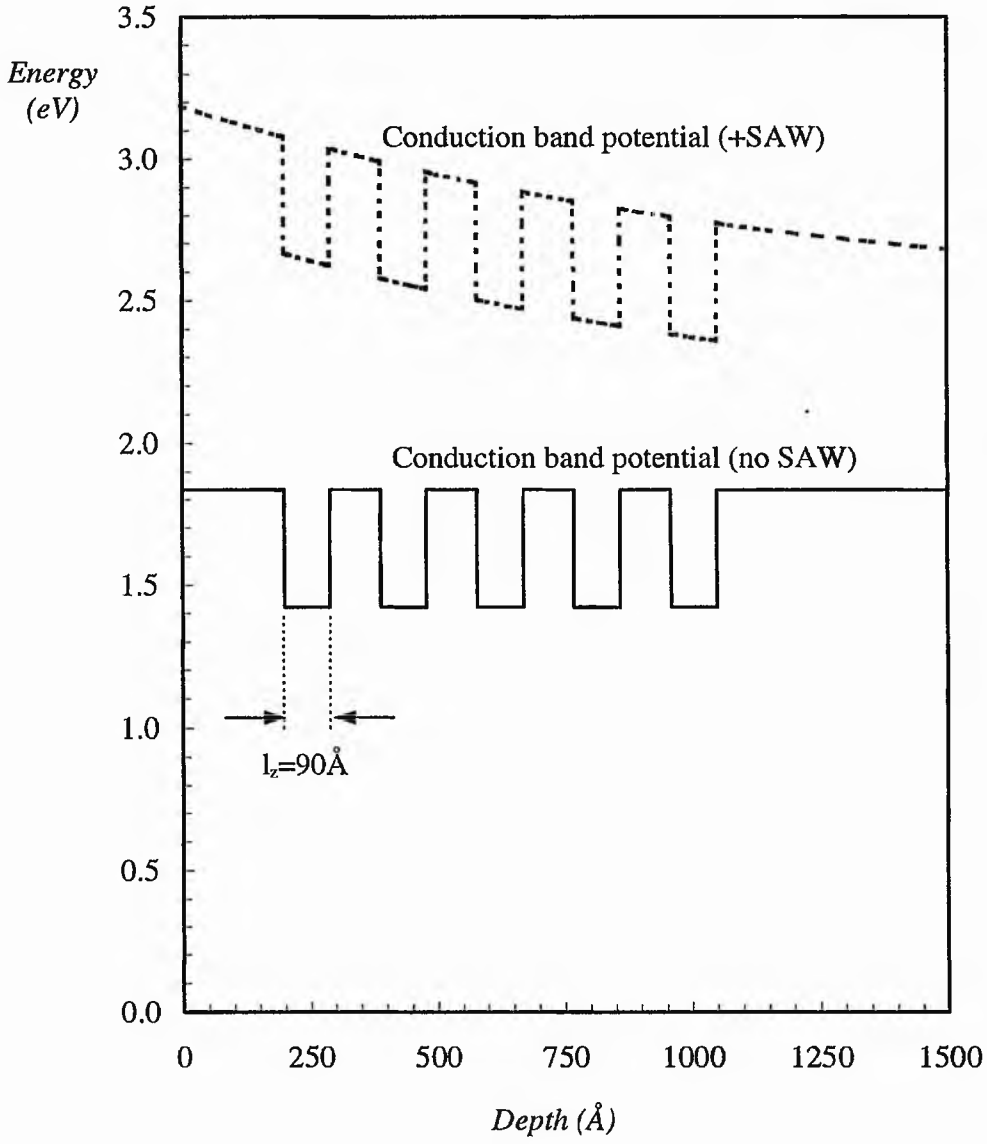

Figure 5.2 *The conduction band potential profiles of a multiple quantum well structure with and without the presence of a SAW in a structure contining five quantum wells of well widths of 90Å*

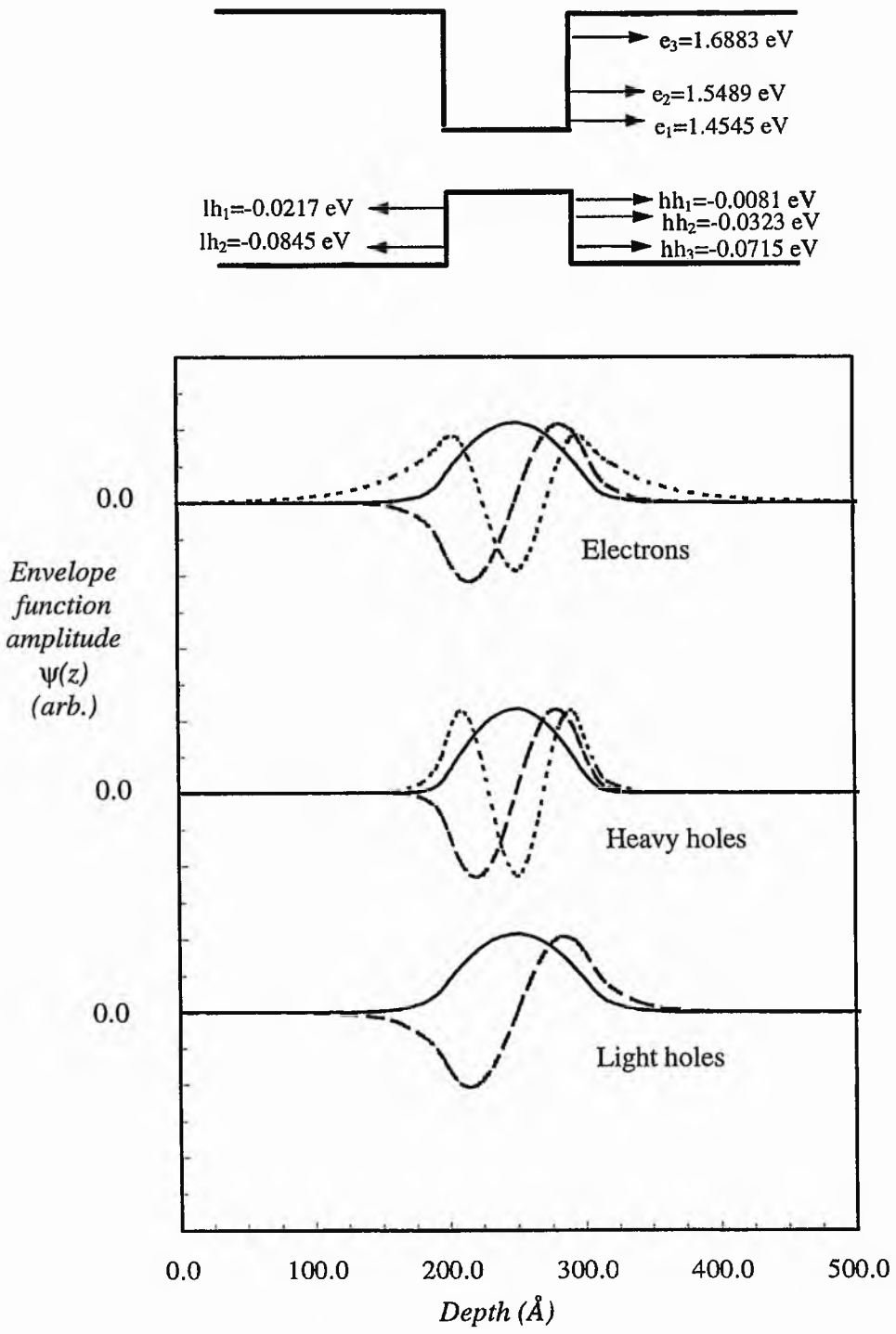

Figure 5.3 *The electron, heavy hole and light hole envelope functions and energy levels in a single AlGaAs/GaAs quantum well of well width l_z=90Å and 35% Aluminium fraction in the barriers.*

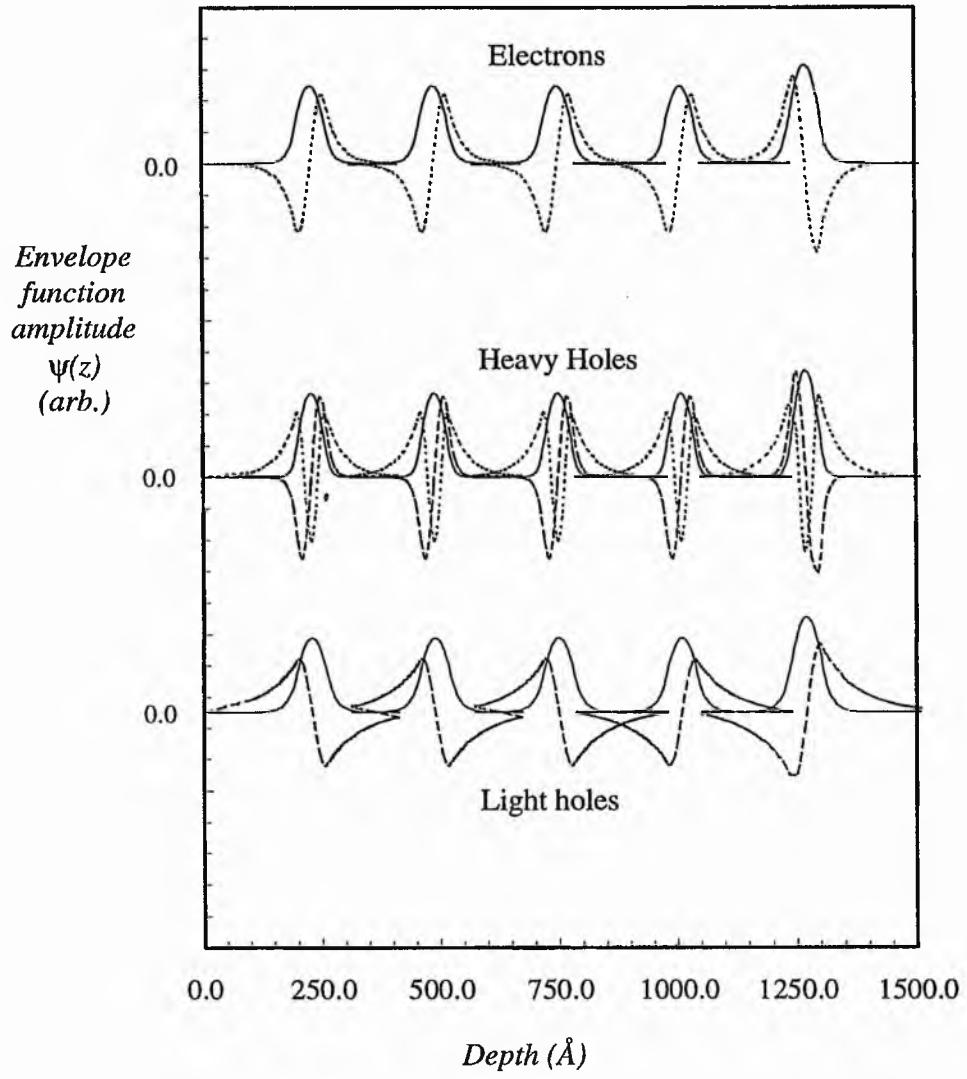

Figure 5.4 *The electron, heavy hole and light hole envelope functions in a multiple quantum well structure consisting of five quantum wells of well widths l_z=60Å, barrier widths in the MQW region of 200Å and Aluminium fractions of 35%.*

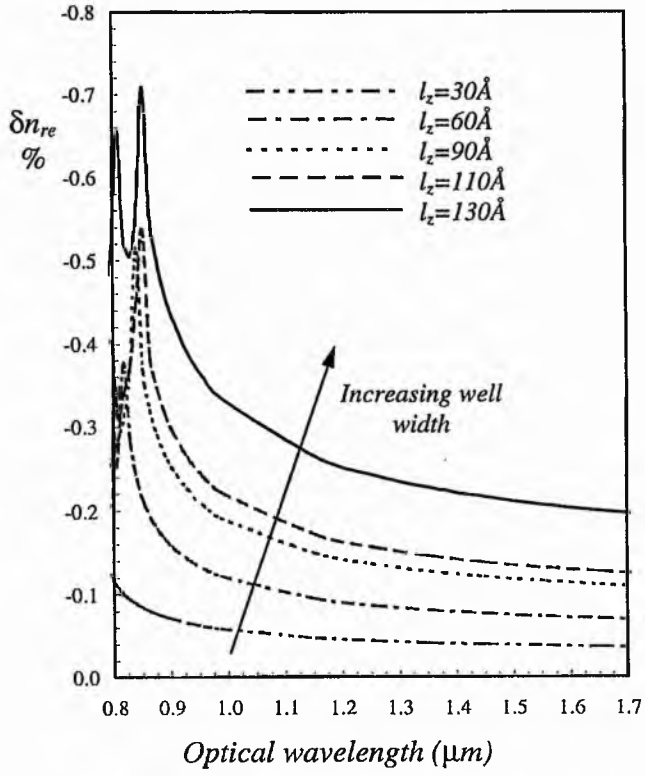

Figure 5.5 *Variation of the change in real part of refractive index (δn_{re}) with optical wavelength for different well widths (l_z) in a single quantum well structure of 50% Aluminium in the barriers with a perturbing SAW of wavelength 2μm and 10mW acoustic power.*

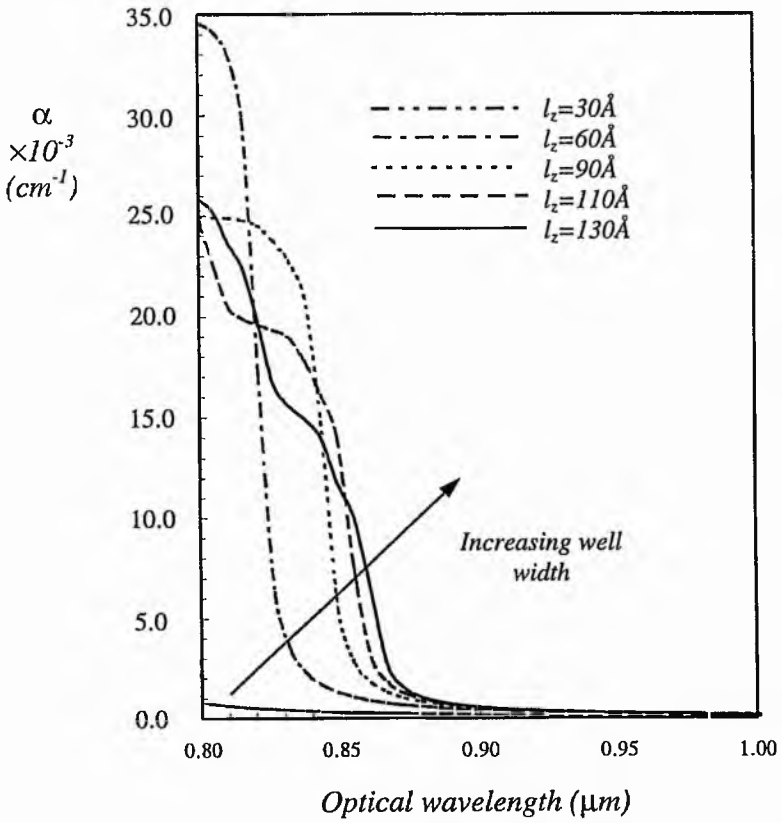

Figure 5.6 *Variation of the absorption coefficent (α) with optical wavelength for different well widths (l_z) in a single quantum well structure of 50% Aluminium in the barriers with a perturbing SAW of wavelength 2μm and 10mW acoustic power.*

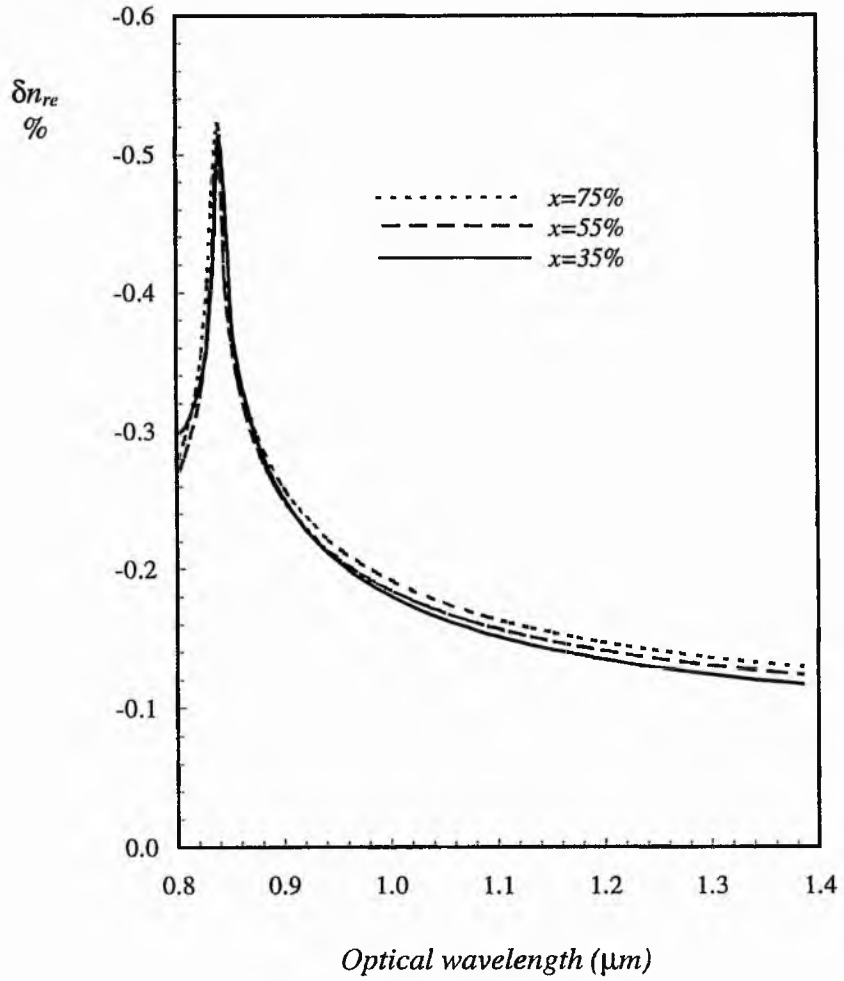

Figure 5.7 *Variation of the change in real part of refractive index (δn_{re}) with optical wavelength for different barrier Aluminium fractions (x) in a single quantum well structure of well width l_z=90Å with a perturbing SAW of wavelength 2μm and 10mW acoustic power.*

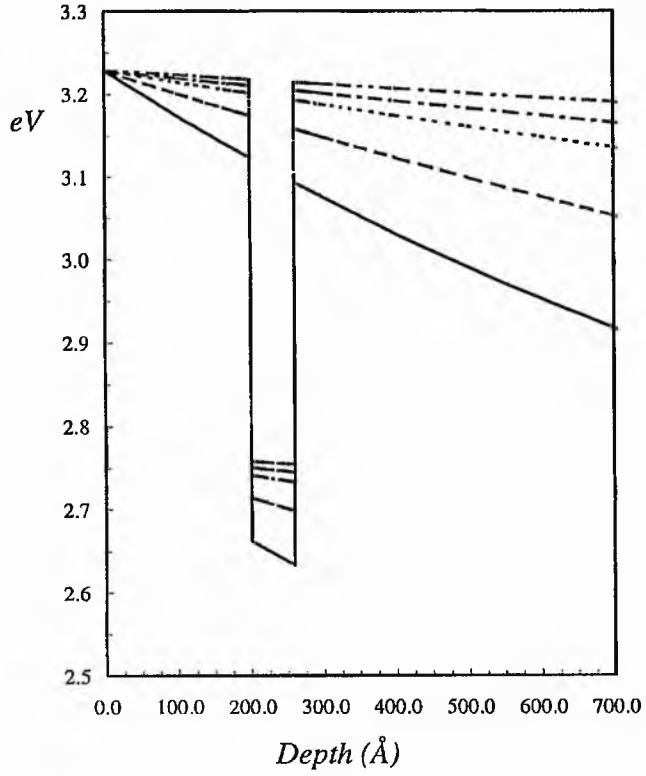

Figure 5.8 *The SAW induced potential depth profiles in single quantum wells structures for a range of acoustic wavelengths, λ_{ac}. Aluminium fraction in the barriers = 55%, well width l_z = 60Å, SAW power= 10mW.*

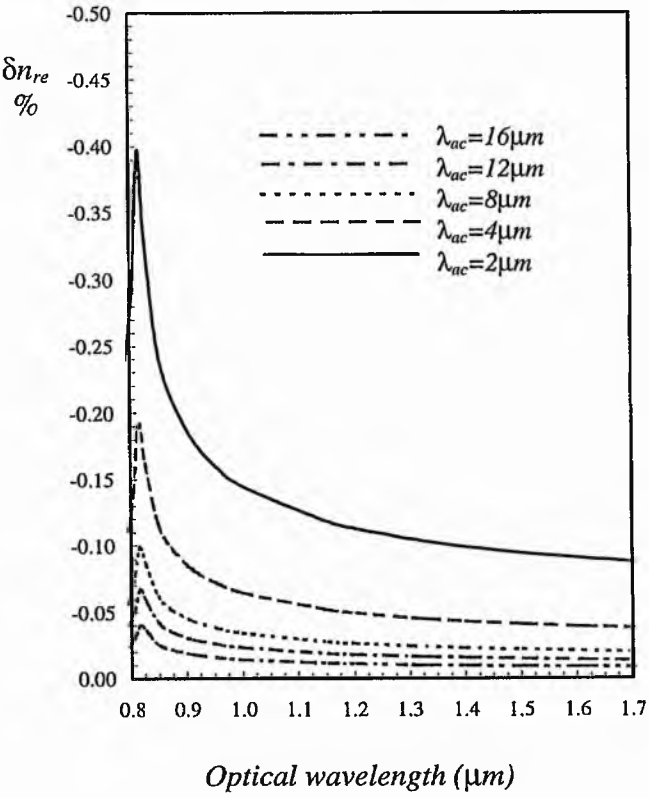

Figure 5.9 *Variation of the change in real part of refractive index (δn_{re}) with optical wavelength for different SAW wavelengths (λ_{ac}) in a single quantum well structure of 55% Aluminium in the barriers and a well width l_z=60Å with a perturbing SAW of 10mW acoustic power.*

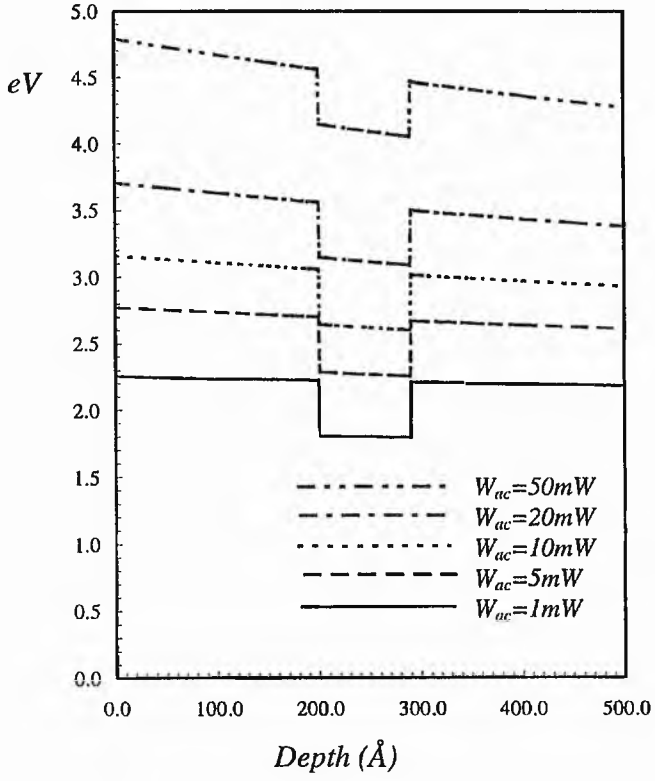

Figure 5.10 *The SAW induced potential depth profiles in single quantum wells structures for a range of acoustic power flows, W_{ac}. Aluminium fraction in the barriers = 55%, well width l_z = 90Å, SAW wavelength = 2μm.*

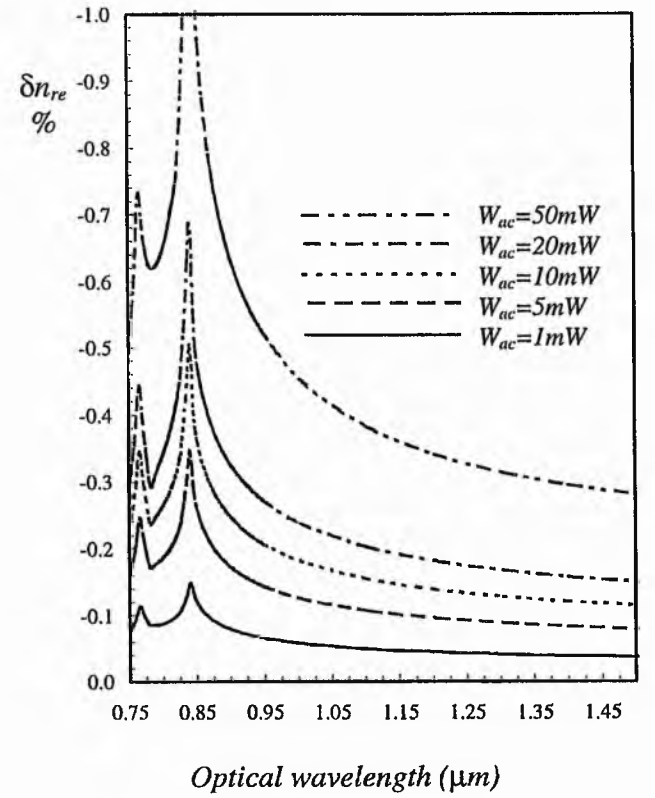

Figure 5.11 *Variation of the change in real part of refractive index (δn_{re}) with optical wavelength for different SAW power flows (W_{ac}) in a single quantum well structure of 55% Aluminium in the barriers and a well width l_z=90Å with a perturbing SAW of wavelength = 2μm.*

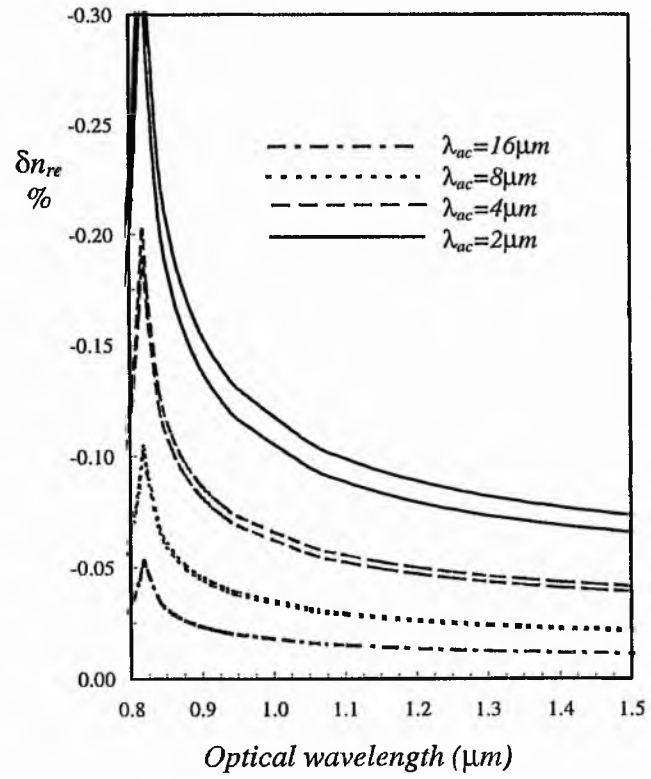

Figure 5.12 *Variation of the change in real part of refractive index (δn_{re}) with optical wavelength for different SAW wavelengths (λ_{ac}) in a double quantum well structure of 55% Aluminium in the barriers and a well width l_z=90Å in each well. The QWs are separated by 100Å of AlGaAs barrier. The perturbing SAW has a power flow of 10mW.*

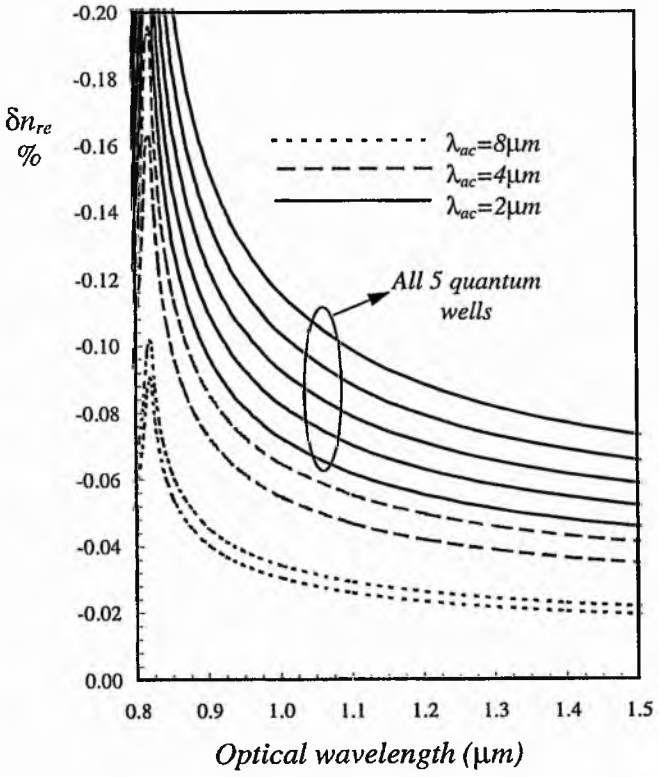

Figure 5.13 *Variation of the change in real part of refractive index (δn_{re}) with optical wavelength for different SAW wavelengths (λ_{ac}) in a MQW structure of five quantum wells of 55% Aluminium in the barriers and a well width l_z=60Å in each well. The QWs are separated by 100Å of AlGaAs barrier. The perturbing SAW has a power flow of 10mW.*

Chapter 6

Conclusions and Future Work

6.1 CONCLUSIONS

In this thesis, a model for calculating the SAW induced fields and guided optical modes in multi-layer and MQW structures has been developed. Isotropic acousto-optic diffraction in the multi-layer structure has been modelled and the various dependencies of the diffraction efficiency considered. The effects of a propagating SAW on the properties of single and multiple quantum wells have also been calculated. The work shows several features which are not included elsewhere and some interesting aspects which are not directly related to the main objectives of the thesis.

In considering the implementation of multi-layer and MQW structures into Bragg cell type devices together with the cell's operation, a number of points emerge :- The aluminium fraction in multi-layer AlGaAs/GaAs structures clearly provides another degree of freedom in setting the nature of the SAW induced potential. In particular high aluminium content at the surface of such structures will optimise the induced potential at the surface and hence increase the electric field in the lower part of the structure. In addition, the characteristics of any individual layer are not sufficient to determine the nature of the SAW induced fields for the whole structure, and the presence of an individual layer of quantum well dimensions has no significant effect on the induced fields. More specifically it is the MQW structure as a

whole that determines the SAW characteristics, and in some cases the MQW structure will be equivalent, in terms of SAW propagation, to a particular bulk composition. On looking in more detail at the magnitude of such SAW induced fields, it was found that for typical SAW wavelengths and power flows, the induced field was comparable in size to electric fields presently employed in electro-absorptive and electro-optic MQW devices.

The greater flexibility in setting the SAW characteristics obtained from employing a multi-layer structure is also carried over to the guided optical modes in such structures. Control over the position of the fundamental mode within the waveguide has been theoretically demonstrated and applications suggested.

Most importantly, the combined use of increased aluminium content and a graded refractive index profile to both increase the SAW induced field amplitude and push the optical mode towards the surface of the structure has been shown (through it's effect on the acousto-optic overlap function) to theoretically increase the acousto-optic diffraction efficiency by a factor of between 2 and 3 for the higher end of the SAW frequency range (>1GHz), see for example Figure 4.8. This is direct evidence of the advantage of using a multi-layer structure as opposed to single layer structures.

It is clear from the results of chapter 5 that the quantum effects of QW structures are exploitable. Increased changes in refractive index are observed over their bulk counterparts. For SAWs of this type, typical refractive index changes in bulk GaAs are ~ 0.01%, calculated from the strains and electric field magnitudes obtained in chapter 1. The refractive index changes obtained for the quantum well structures of chapter 5 are at least an order of magnitude greater than this and in some cases closer to two orders of magnitude, for the same acoustic powers. This could for example lead to shorter interaction lengths as compared to typical bulk devices. In addition, when comparing the case of SAWs on MQW structures to that of applying constant electric fields to such structures, it is clear that firstly, equivalent shifts in refractive index are possible with the additional advantages that a SAW incorporates i.e. the signal is accessible at the surface, and can be utilised for a great diversity of signal processing applications. When considering the issue of power requirements it must first be noted that the characteristics of the SAW generating transducer will play a large roll

in setting any minimum power threshold and must be considered in detail for device design. However, the non-linear shape of the SAW induced potential implies that an equivalent potential difference to that corresponding to a constant electric field, could produce higher electric fields within a specified depth range of the structure. This effect would of course depend on the SAW wavelength and hence indirectly also on the conversion efficiency of the SAW transducer.

Also it has been shown that the non-linearity associated with a SAW induced potential is significant when considering the optical properties of that structure, and can lead to variations in δn_{re} of ~0.05% across the structure for a MQW containing 5 quantum wells of moderate size (see figure 5.13). This result is of considerable importance since previously in proposing MQW acousto-optic devices it has been assumed that the MQW structure is not large enough to be affected by the non-linearity. This is clearly not true for high frequency operation ($>$1GHz), and could be detrimental to device operation.

In summary, the work has shown the considerable potential for the use of SAW effects in MQW and multi-layer structures for adaptive signal processing devices and also pointed out the points that would need to be addressed for specific device design.

6.2 FUTURE WORK

The models developed in the thesis can easily be applied to other III-V material systems such as InGaAs/InP and InGaAs/AlGaAs with the proviso that the as-grown strain in the structures is included in the analyses. Additionally, the propagation of SAWs on interdiffused quantum well structures would provide a new area of study where the possibilities for tailoring the optical and electrical properties of the QW structure are much greater.

From a theoretical point of view the model used to look at the propagation of the SAW on a QW structure is crude. Although the envelope function approximation is appropriate, the

validity of the static approximation adopted is unknown, and in this sense experimental verification of the effect of a SAW on the confined energy levels of a QW would help to clarify the problem of validity. From a fundamental standpoint what is needed is a model of the band structure of the material under investigation with a perturbing SAW. Only then can the overall effects of the SAW on the electric and optical properties be fully understood.

The contribution of excitons to the optical properties of quantum wells has not been considered in chapter 5 and will obviously be important for device operation around the band-edge of material structures, for example in devices employing electro-absorption mechanisms. Excitons, in the form of electron-hole bound pairs, provide another realisation of an electromagnetic oscillator that will contribute to the spectrum of oscillators within the material and hence to the dielectric function. Clearly an inclusion of excitons to the QW model will give a better indication of the changes in absorption and refractive index possible with the addition of a SAW.

Some acousto-optic devices are based on anisotropic acousto-optic (AO) interactions in which the incident light may be diffracted form one polarisation state to another. This means that the photon-phonon momentum matching conditions can be approximately satisfied for a range of incident light angles, leading to large aperture characteristics which are useful in the operation of AO filters. The extension of the model to include anisotropic diffraction and coupling between all modes of the optical waveguide would clearly be advantageous.

Although the changes in complex refractive index due to a SAW on a QW structure have been calculated, they have not been applied to the acousto-optic diffraction analysis begun in chapter 4. In this sense the extension of the model of chapter 4 should also include electro-optic effects in QW structure.

When considering specific device design a number of issues need to be addressed. The presence of intermodulation products (IMPs) within the acousto-optic cell will limit the dynamic range of devices, suggesting that some sort of estimation of these effects would be required. The transducer that generates the SAWs (usually an IDT) will have a frequency dependent conversion efficiency which will limit the optimum performance of any acousto-

optic device. Clearly then, any inherent advantage gained in device operation from employing AO interaction in multi-layer/MQW structures must be tolerated by the transducer and this will have to be considered during transducer design.

The acousto-optic tunable filter (AOTF), as mentioned in chapter 1, is an optical filter that is tunable electronically through the driving acoustic frequency and has received much attention over recent years. An in depth study of this type of device, employing either a multi-layer or MQW structure would help to clarify the advantages in using such structures for AO devices and also address in more detail the practical problems of such an endeavour.